# Thin Films of π-Conjugated Chalcogenadiazole: Growth, Structure, and Optical Properties

**Dissertation**
der Mathematisch-Naturwissenschaftlichen Fakultät
der Eberhard Karls Universität Tübingen
zur Erlangung des Grades eines
Doktors der Naturwissenschaften
(Dr. rer. nat.)

vorgelegt von
Anton Pylypenko
aus Kiew/Ukraine

Tübingen
2025

Gedruckt mit Genehmigung der Mathematisch-Naturwissenschaftlichen Fakultät der Eberhard Karls Universität Tübingen.

| | |
|---|---|
| Tag der mündlichen Qualifikation: | 23.02.2026 |
| Dekan: | Prof. Dr. Thilo Stehle |
| 1. Berichterstatter/-in: | Prof. Dr. Dr. h.c. Frank Schreiber |
| 2. Berichterstatter/-in: | Prof. Dr. Martin Oettel |

# Contents

**Abstract** **7**

**Zusammenfassung in deutscher Sprache** **9**

## I Introduction and Theory 11

**1 Introduction** **13**

**2 Theory** **17**
- 2.1 Organic semiconductors . . . . . 17
  - 2.1.1 Molecular structure and properties of OSCs . . . . . 17
  - 2.1.2 Solid state interactions in organic solids . . . . . 20
- 2.2 Thin film growth . . . . . 21
  - 2.2.1 Growth modes . . . . . 24
  - 2.2.2 Issues specific to organic thin film growth . . . . . 25
  - 2.2.3 Co-deposition of two organic materials . . . . . 26
  - 2.2.4 Growth of bilayer thin films . . . . . 28
- 2.3 X-ray scattering . . . . . 29
  - 2.3.1 X-ray scattering on one electron . . . . . 30
  - 2.3.2 X-ray scattering on one atom . . . . . 33
  - 2.3.3 X-ray scattering on one molecule . . . . . 35
  - 2.3.4 X-ray scattering on crystal . . . . . 36
  - 2.3.5 X-ray refraction and reflection . . . . . 38

## II Materials & Methods 41

**3 Materials** **43**
- 3.1 Dibenzoselenadiazoloquinoxaline (dbSeQ) . . . . . 43
- 3.2 Diindenoperylene (DIP) . . . . . 44
- 3.3 Pentacene (PEN) . . . . . 45

**4 Experimental Methods** **47**
- 4.1 Organic molecular beam deposition (OMBD) . . . . . 47
- 4.2 Atomic Force Microscopy (AFM) . . . . . 49
- 4.3 Scanning Electron Microscopy (SEM) . . . . . 51

4.4 X-ray Reflectivity (XRR) . . . . . 52
4.5 Grazing Incidence Small Angle X-ray Scattering (GISAXS) . . . . 54
4.6 Grazing Incidence Wide Angle X-ray Scattering (GIWAXS) . . . 56
4.7 UV-Vis absorption spectroscopy (UV-Vis) . . . . . 57
4.8 Photoluminescence spectroscopy (PL) . . . . . 58

**III Results 61**

**5 Results of pristine dibenzoselenadiazoloquinoxaline thin film growth and annealing kinetics 63**
5.1 Growth conditions and sample preparation . . . . . 64
5.2 Morphology evolution during growth . . . . . 66
5.3 Morphology evolution during annealing . . . . . 71
5.4 Ex situ morphology studies . . . . . 75
5.5 Crystalline structure of the films . . . . . 85
5.6 Optical Properties . . . . . 87
5.7 Summary and conclusion . . . . . 89

**6 Results of thin film growth and annealing kinetics of bilayer and mixed complexes incorporating dibenzoselenadiazoloquinoxaline, diindenoperylene and pentacene 93**
6.1 Morphology evolution during growth . . . . . 94
6.1.1 Morphology evolution during growth of the heterostructures incorporating dbSeQ and DIP . . . . . 94
6.1.2 Morphology evolution during growth of the heterostructures incorporating dbSeQ and PEN . . . . . 98
6.2 Morphology evolution during annealing of heterostructures incorporating dbSeQ and DIP . . . . . 100
6.3 Ex situ morphology studies . . . . . 106
6.3.1 Ex situ morphology studies of the heterostructures incorporating dbSeQ and DIP . . . . . 107
6.3.2 Ex situ morphology studies of the heterostructures incorporating dbSeQ and PEN . . . . . 108
6.4 Crystalline structure of the films . . . . . 111
6.4.1 Crystalline structure of the heterostructures incorporating dbSeQ and DIP . . . . . 111
6.4.2 Crystalline structures of the heterostructures incorporating dbSeQ and PEN . . . . . 112
6.5 Optical Properties . . . . . 113
6.5.1 Optical characterization of the heterostructures incorporating dbSeQ and DIP . . . . . 114
6.5.2 Optical characterization of the heterostructures incorporating dbSeQ and PEN . . . . . 115

6.6 Summary and conclusion . . . . . . . . . . 116
6.6.1 Summary and conclusion on films with DIP . . . . . . . . 116
6.6.2 Summary and conclusion on films with PEN . . . . . . . . 118

**IV Conclusions and outlook 121**

**7 Conclusions 123**

**8 Outlook 127**

**V Appendices 129**

**9 Appendix 131**
9.1 Additional morphology investigations . . . . . . . . . . 131
9.2 Additional XRR data . . . . . . . . . . 133
9.3 Additional GISAXS data . . . . . . . . . . 134

**List of Abbreviations 137**

**Bibliography 139**

**List of own publications 163**

**Acknowledgments 165**

# Abstract

Organic semiconductors (OSCs) represent a rapidly advancing class of materials of great importance to the field of optoelectronics because of their unique properties and functionalities. The utilization of thin films of organic semiconductors has become pervasive within the domain of organic optoelectronics, with devices such as organic field-effect transistors (OFETs), organic light-emitting diodes (OLEDs), and organic solar cells serving as notable exemplars. A crucial aspect of the fabrication of optoelectronic devices based on organic small molecules is the understanding of the growth and the post-growth effects in thin films of these molecules, since the performance of thin-film-based devices depends on the characteristics of the thin film. The combination of organic molecular beam deposition (OMBD) and high vacuum conditions is of high priority during the fabrication of organic thin films, as it allows for the precise control of growth and the production of high-quality films for device applications. One of the factors that can negatively impact the performance of a given material despite its suitability in terms of electrical and optical properties is the dewetting of the produced film. Consequently, the study of thin film growth and the post-growth effects, along with its structural and optical properties, is of significant interest not only to the scientific community but also to industrial implementation.

Thin films composed of $\pi$-conjugated organic molecules have attracted considerable attention in the field of organic optoelectronics. Thiadiazolo-heteroacenes, which are distinguished by their robust and adjustable absorption spectra and effective charge transport properties, are emerging as promising candidates for these technologies. It is anticipated that chemical modifications, particularly those that incorporate a heavy Se atom and thus expand the $\pi$-conjugation, will allow fine-tuning of the optical characteristics and influence the structural configurations via the heavy-atom effect and additional interactions. Hence, a comprehensive understanding of the growth mechanisms of thin films and optical properties of such compounds is pivotal for the advancement of future applications.

The present work reveals the growth behavior and the post-growth effects in thin films of dibenzoselenadiazoloquinoxaline (dbSeQ), a new organic semiconductor, thin films of which tend to dewet on $Si/SiO_x$ substrates. To overcome this limiting feature, we deposited thin films of dbSeQ in combination with well-studied organic semiconductors, namely, diindenoperylene (DIP) and pentacene (PEN) at room and low substrate temperatures (RT and LT, respectively). Using X-ray scattering techniques, i.e. grazing-incidence small-angle X-ray scattering (GISAXS) and X-ray reflectivity (XRR), we characterized the growth and the annealing of thin films *in situ* in real time. The combination of atomic force microscopy

(AFM), grazing-incidence wide-angle X-ray scattering (GIWAXS), PL spectroscopy (PL) and UV-Vis absorption spectroscopy (UV-Vis) provides additional important information about the morphology, structure and optical properties of the deposited films *ex situ*. These results are of great importance for understanding the growth of organic semiconductors incorporating fused 1,2,5-selenadiazoles and the factors that influence it, which can be used for the future development of thin film-based devices.

# Zusammenfassung in deutscher Sprache

Organische Halbleiter (OSCs) stellen eine sich rasch entwickelnde Materialklasse dar, die aufgrund ihrer einzigartigen Eigenschaften und Funktionen von großer Bedeutung für den Bereich der Optoelektronik ist. Im Bereich der organischen Optoelektronik hat sich die Verwendung dünner Schichten durchgesetzt. Als bemerkenswerte Beispiele können hier Geräte wie organische Feldeffekttransistoren (OFETs), organische Leuchtdioden (OLEDs) und organische Solarzellen angeführt werden. Ein entscheidender Aspekt bei der Herstellung optoelektronischer Bauelemente auf Basis organischer Kleinmoleküle ist das Verständnis der Wachstums- und Nachwachseffekte in Dünnschichten dieser Moleküle, da die Leistung dünnschichtbasierter Bauelemente von den Eigenschaften der Dünnschicht abhängt. Die Kombination aus organischer Molekularstrahldeposition (OMBD) und Hochvakuumbedingungen hat bei der Herstellung organischer Dünnschichten hohe Priorität, da sie eine präzise Steuerung des Wachstums und die Herstellung hochwertiger Schichten für Bauelementanwendungen ermöglicht. Ein Faktor, der die Leistung eines Materials trotz seiner Eignung bezüglich ihrer elektrischen und optischen Eigenschaften negativ beeinflussen kann, ist die Entnetzung der hergestellten Schicht. Aus diesem Grund ist die Untersuchung des Dünnschichtwachstums und der Nachwachseffekte sowie der strukturellen und optischen Eigenschaften von großem Interesse, sowohl für die Wissenschaft als auch für die industrielle Umsetzung.

Dünnschichten aus $\pi$-konjugierten organischen Molekülen haben im Bereich der organischen Optoelektronik erhebliche Aufmerksamkeit erhalten. Thiadiazolo-Heteroarene, die sich durch ihre robusten und einstellbaren Absorptionsspektren und effektiven Ladungstransporteigenschaften auszeichnen, entwickeln sich zu vielversprechenden Kandidaten für diese Technologien. Es wird angenommen, dass chemische Modifikationen, insbesondere solche, die ein schweres Se-Atom enthalten und folglich die $\pi$-Konjugation erweitern, eine Feinabstimmung der optischen Eigenschaften ermöglichen. Diese Modifikationen beeinflussen die strukturellen Konfigurationen über den Effekt des schweren Atoms sowie zusätzliche Wechselwirkungen. Daher ist ein umfassendes Verständnis der Wachstumsmechanismen von Dünnschichten und der optischen Eigenschaften solcher Verbindungen für die Weiterentwicklung zukünftiger Anwendungen von entscheidender Bedeutung.

Die vorliegende Arbeit demonstriert das Wachstumsverhalten und die Nachwachseffekte in Dünnschichten aus Dibenzoselenadiazoloquinoxalin (dbSeQ), einem neuartigen organischen Halbleiter, dessen Schichten eine Tendenz zur Entnet-

zung auf Si/SiO$_x$-Substraten aufweisen. Um diese Einschränkung zu überwinden, wurde die Abscheidung von Schichten aus dbSeQ in Kombination mit gut untersuchten organischen Halbleitern, nämlich Diindenoperylen (DIP) und Pentacen (PEN), bei Raumtemperatur und niedrigen Substrattemperaturen (RT bzw. LT) durchgeführt. Mittels Röntgenstreuungstechniken, konkret streifender Kleinwinkel-Röntgenstreuung (GISAXS) und Röntgenreflektivität (XRR), wurde eine Echtzeit-Charakterisierung des Wachstums und des Temperns von Dünnschichten *in situ* durchgeführt. Die Kombination der Verfahren Rasterkraftmikroskopie (AFM), streifende Weitwinkel-Röntgenstreuung (GIWAXS), PL-Spektroskopie (PL) und UV-Vis-Absorptionsspektroskopie (UV-Vis) liefert maßgebliche Informationen zu Morphologie, Struktur und optischen Eigenschaften der abgeschiedenen Schichten *ex situ*. Diese Ergebnisse sind von signifikanter Relevanz für das Verständnis des Wachstums von organischen Halbleitern mit fusionierten 1,2,5-Selenadiazolen sowie der Faktoren, die dieses Wachstum beeinflussen und für die zukünftige Entwicklung dünnschichtbasierter Geräte genutzt werden können.

# Part I

# Introduction and Theory

## Chapter 1

# Introduction

The future of modern microelectronics is connected to an increasing degree of integration of its elements, the speed, and reliability of information processing. The steady increase in complexity and performance of traditional silicon-based planar integrated circuits cannot continue indefinitely because of limitations such as high power consumption and the memory wall [1–3]. In recent years, there has been a search for fundamentally new solutions that would lead to significant progress in microelectronics. One of these directions, based on attempts to use individual molecules (mainly organic) as the basis of microelectronic devices, has been called molecular electronics [4]. Since their discovery in 1905 [5, 6], organic semiconductors (OSCs) have gained significant interest from the scientific community due to their compelling properties, including their mechanical flexibility, ease of production, and low cost. Organic substances in the condensed state (molecular crystals, ordered films, polymers, etc.) are characterized by weak intermolecular interactions, allowing optimal combinations of the individual properties of molecules and the collective properties of aggregates [7, 8]. This enables, given the vast variety of organic compounds and the comparative simplicity of their synthesis, the creation of devices based on solid organic substances with fundamentally different and more extensive capabilities when compared to those of their traditional counterparts. OSCs are already in use in various areas and devices, such as organic field-effect transistors (OFETs), organic thin-film transistors (OTFTs), organic light-emitting diodes (OLEDs), flexible light sources, displays, and solar cells [9–21].

The design and fabrication of such devices frequently require the production of thin films. Similarly to traditional inorganic semiconductors, the performance of their organic counterparts is related to their molecular packing, crystallinity, and purity [21]. For example, it was found that during the operation of OTFT, the majority of mobile charges are located within the first several monolayers of the OSC film at the semiconductor/dielectric interface [22–24]. Consequently, a profound understanding of the growth processes of thin films of organic materials is pivotal in order to achieve optimal device performance.

An effective way to improve the electronic performance of these devices is to control how the donor and acceptor molecules are arranged, which can be tuned through different preparation methods. Two commonly employed strategies are bulk heterojunctions (BHJs), where both components are co-deposited to create the active layer, and planar heterojunctions (PHJs), in which separate donor and acceptor layers are deposited one after the other [25–32].

Fabrication methods for a thin film can be categorized into two main approaches: solution and vapor deposition techniques. Solution deposition implies the coating of the substrate with an organic solvent that contains a dissolved organic semiconductor. As the solvent vaporizes, a thin film is formed on the substrate [33]. Moreover, a strategy for the transfer of monolayers from the air/water interface to a solid substrate has been developed for hydrophobic materials. This transfer can be achieved through vertical deposition, also known as the Langmuir-Blodgett technique, or horizontal deposition, also known as the Langmuir-Schaefer technique [34–36]. Vapor deposition involves condensation of the material on the substrate from the gaseous phase. In the realm of vapor deposition techniques, physical vapor deposition (PVD) has garnered significant attention in recent years due to its notable versatility and the wide array of techniques it comprises, including thermal evaporation, physical sputtering, laser ablation, and arc-based emission [37]. In this thesis, we used the vapor deposition technique called organic molecular beam deposition (OMBD, see Sec. 4.1 for more details), which involves sublimation of organic material in a vacuum to a gaseous state, followed by subsequent condensation of the material into a film that covers the substrate surface [38].

Growth of organic thin films from the vapor phase is a sophisticated non-equilibrium process involving numerous kinetic processes. The resulting film characteristics depend on several factors such as substrate temperature, deposition rate, choice of substrate, molecule-substrate compatibility, vibrational degrees of freedom, etc. (see Sec. 2.2 for more details). By controlling the deposition parameters, one can tailor properties of organic thin films which is crucial for obtaining high-quality thin-film devices [39]. However, thin films often experience post-growth effects, such as dewetting, which can lead to the roughening of the resulting film. Consequently, in order to obtain comprehensive information about the evolution of the structure, kinetics, and transient structures, it is essential to perform real-time measurements [40]. In this context, X-ray scattering techniques are ideal for non-invasive investigation of the film structure and morphology during the growth [41–43].

In this research, we investigate the growth and annealing kinetics of thin films of the novel semiconductor material dibenzoselenadiazoloquinoxaline (dbSeQ) and its blends with well-investigated OSCs diindenoperylene (DIP) and pentacene (PEN). During the growth and subsequent annealing, we examined the morphology of thin films *in situ* by using grazing-incidence small-angle X-ray scattering (GISAXS) and X-ray reflectivity (XRR). In this work, GISAXS is the main characterization method, as it is versatile and allows to track surface morphology evolution during the deposition in real time [43–45]. Real-space imaging techniques such as atomic force microscopy (AFM) and scanning electron microscopy (SEM) allowed for a detailed analysis of morphological properties *ex situ*. Structural properties were investigated using grazing-incidence wide-angle X-ray scattering (GIWAXS). Optical properties were explored by photoluminescence spectroscopy and absorption spectroscopy in the UV-Vis range.

By combining the *in situ* and *ex situ* characterization, we can form a comprehen-

sive description of film growth and post-growth effects. We studied the influence of the deposition rate, low and high substrate temperatures on the morphology of the resulting film. We found how the growth of dbSeQ differs depending on the substrate temperature and how it changes in heterostructures with other organic materials. We anticipate that the insights gained from our research will significantly contribute to the advancement of understanding and development of future organic semiconductor technologies.

This thesis contains four parts and is organized as follows: The first part is devoted to the theoretical aspects important in the scope of this work. The second part of the thesis is aimed at the materials and methods that were used and, in the third part, the results of our investigations are presented. The fourth part contains conclusions and an outlook for the whole thesis.

The theoretical part is presented in Chap. 2 and covers the basics of OSCs, thin film growth, and X-ray scattering. OSCs are discussed in Sec. 2.1 which covers the structural properties and mechanisms of interaction between molecules in organic solids. It is followed by a brief overview of the growth of organic thin films which is given in Sec. 2.2. It includes descriptions of growth scenarios and factors that are influencing the growth of single-component films, as well as more complex cases of the growth of two organic materials in different configurations. The last section of the theoretical part is devoted to X-rays and the interaction of X-rays with matter. Sec. 2.3 gives insights into the interaction of X-rays with matter, from the simple case of scattering on the single electron to scattering on the crystal.

The brief description and unit cell parameters of the organic compounds that were used in this work are presented in Chap. 3. The insights and principle of operation of a particular characterization technique are disclosed in Chap. 4.

The results part is divided into two chapters: Chap. 5 is focused on the growth and annealing behavior of neat dbSeQ films. For neat films, we explored how their growth depends on rate and substrate temperature, which includes *in situ* real-time GISAXS was taken during growth and subsequent annealing. In addition, the optical characterization by PL spectroscopy at LT is included. Chap. 6 is dedicated to the growth of dbSeQ together with DIP and PEN in a layered configuration or during simultaneous deposition. For the bilayer films with DIP, the growth at different substrate temperatures was explored.

The fourth part of the thesis summarizes the results and conclusions (Chap. 7) to provide a wider picture of the work that has been done. Furthermore, several suggestions regarding possible implementations and other characterization possibilities are given in the outlook in Chap. 8.

Chapter 2

# Theory

## 2.1 Organic semiconductors

This section is based on Refs. [46, 47], and all other references are explicitly cited.

Organic semiconductors (OSCs) are a unique class of materials that combine the electrical properties of semiconductors with the mechanical and chemical versatility of organic molecules. Unlike traditional inorganic semiconductors, which rely on rigid crystalline lattices, OSCs utilize $\pi$-conjugated molecular systems for electronic functionality. These materials, comprising carbon-based small molecules or polymers, have garnered significant attention for their use in emerging electronics such as organic light-emitting diodes (OLEDs), organic photovoltaics (OPVs) and organic field-effect transistors (OFETs) [32, 48, 49]. Their lightweight nature, flexibility, and compatibility with low-cost processing methods make them attractive for flexible and sustainable electronics.

### 2.1.1 Molecular structure and properties of OSCs

Organic materials contain mostly carbon and hydrogen atoms and could include heteroatoms like oxygen, nitrogen, selenium, sulfur, and others. In general, we can highlight three varieties of OSCs: amorphous molecular films, polymer films, and molecular crystals. The nature of the semiconductor properties in these types are similar, but their electronic structure and photophysical properties may differ on the order and coupling in the solid. In this thesis we were using the molecular crystals PEN, DIP and dbSeQ. The distinctive electronic properties of OSCs such electrical conductivity arise from their molecular structure. By alternating the single and double bonds along their backbone, $\pi$-conjugated systems can be created, which results in delocalized molecular orbitals.

To understand the concept of $\pi$-conjugation in OSCs, we first look at the electronic structure of carbon and discuss the formation of hybrid orbitals on the example of a carbon atom. In the ground state it has six electrons: two in a $1s$ orbital, two in a $2s$ orbital and two from three $2p_x$,$2p_y$,$2p_z$-orbitals (Fig. 2.1), that can be written as $1s^2 2s^2 2p^2$. If the carbon atom is influenced by other atoms, i.e. it is a part of the molecule, the energy difference between the $2s$- and the $2p$-orbitals is compensated and forces them to degenerate.

This means that the new, energetically-favorable hybrid orbitals are formed from a linear combination of the $2s$- and the $2p$-orbitals. Fig. 2.2 presents the possible

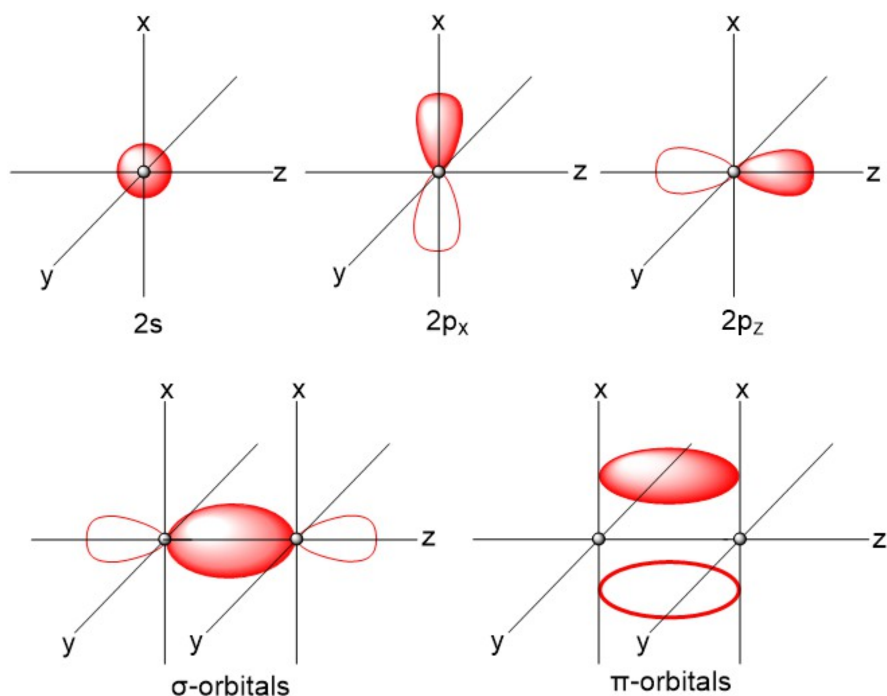


***Figure 2.1:*** *Top row: Atomic s and p orbitals. Bottom row: Molecular $\sigma$ and $\pi$ orbitals formed by the constructive overlap of two $p_z$ and two $p_x$ orbitals, respectively. Image adapted from [46].*

variants of the hybridization. The combination of two orbitals, namely, one $2s$ and one $2p$ results in two $sp$-hybrid orbitals at an angle of 180° between them. When a $2s$ orbital mixes with two $2p$ orbitals it produces three $sp^2$-hybridized orbitals with an angle of 120° between them. Finally, when all four orbitals are mixing it results in four $sp^3$-hybridized orbitals with an angle 109.5° between them.

In a carbon atom, the quantity of hybrid and $p$-orbitals determines the number of bonds it is able to create. Chemical bonds can be explained by a pair of electrons that equally belong to a pair of adjacent atoms simultaneously. Because the electron cannot be assigned to one atom, it is assigned to the molecular orbitals instead atomic orbitals.

A classic example of the organic molecule is benzene $C_6H_6$ presented in Fig. 2.3. In this molecule, each of six carbon atoms has three $2sp^2$-hybridized orbitals and one $2p_z$-orbital. Hybridized orbitals yield three orbitals located in the $xy$-plane that are called $\sigma$-orbitals and the associated bonds are called $\sigma$-bonds. The one $2p_z$-orbital that remains not hybridized and directed perpendicular to xy-plane is called $\pi$-orbital and the associated bonds are called $\pi$-bonds. The electron in the $2p_z$ orbital will be paired with the electron in the $2p_z$ orbital of the nearest carbon atom. It means the creation of the spatial probability density located symmetrically below and above the molecule axis, and called delocalized $\pi$-system. Such delocalization enhances the electronic properties of organic semiconductors,

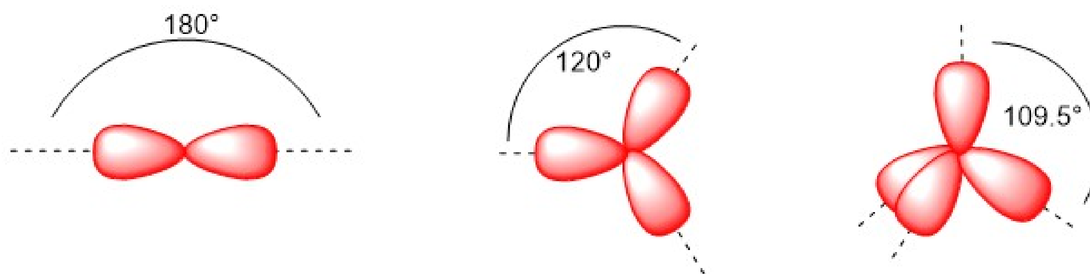


***Figure 2.2:*** *Schematic representation of hybridization types, illustrating sp, $sp^2$, and $sp^3$ hybrid orbitals from left to right. Image adapted from [46].*

providing pathways for charge transport.

The molecular orbitals of a molecule, derived via the linear combination of atomic orbitals (LCAO), define the electron distribution across the entire molecular system. Among these orbitals, two hold particular significance for their influence on optical and electronic properties: the highest occupied molecular orbital (HOMO) and the lowest unoccupied molecular orbital (LUMO), analogous to the valence and conduction bands in inorganic semiconductors [50]. Their energy difference determines the molecular energy gap.

HOMO and LUMO can be related to ionization energy (IE) and electron affinity (EA), respectively. IE represents the energy required to remove an electron from the HOMO to the vacuum level (VL), while EA describes the energy gained when an electron is added to the LUMO from the VL. The VL serves as a universal energy reference point, corresponding to the energy of an electron infinitely removed from the system. To measure the IE and EA, approaches including photoemission spectroscopy or cyclovoltammetry are commonly used.

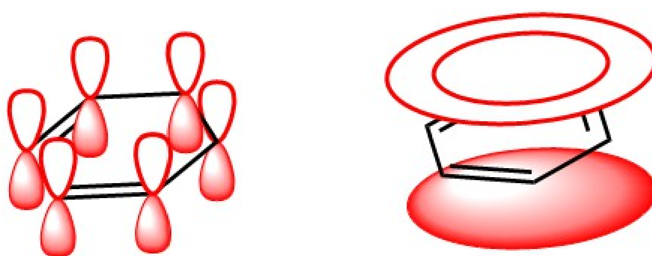

***Figure 2.3:*** *Left: Orientation of uncoupled $p_x$ orbitals in benzene molecule. Each carbon atom has a $p_x$ orbital oriented perpendicular to the plane of the molecule. These uncoupled orbitals, however, are not present in the actual benzene molecule due to coupling effects. Right: The coupling of these $p_x$ orbitals results in the formation of $\pi$ orbitals. Image adapted from [47].*

Similarly to inorganic semiconductors, OSCs electrons can move from the HOMO to the LUMO if provided with energy equivalent or higher than the energy gap, for instance, through optical activation, such as absorption of a photon. This excitation

plays a critical role in the charge transport and photophysical properties of organic semiconductors. The stronger $\sigma$-bonds in these molecules ensure structural integrity when the anti-bonding $\pi$-orbitals become populated. Additionally, $\pi$-electron systems significantly contribute to intermolecular interactions, which are dominated by relatively weak van der Waals forces. These interactions influence the stability of molecular solids, making them susceptible to structural defects due to the low energy needed for molecular displacements and dislocations.

Optical excitation of a conjugated $\pi$-system generates a bound electron–hole pair, known as an exciton. Because excitons in OSCs possess limited charge mobility, transport occurs primarily through hopping between neighboring molecules rather than through the band-like mechanisms typical of inorganic semiconductors. The efficiency of hopping is heavily dependent on the degree of $\pi$-$\pi$ orbital overlap between neighboring molecules, with optimal transport occurring when molecules are closely aligned.

Structural properties thus play a pivotal role in determining the electronic behavior of molecular solids composed of small OSCs. In such systems, the interplay between molecular orientation, $\pi$-system interactions, and intermolecular forces directly impacts their optoelectronic performance.

### 2.1.2 Solid state interactions in organic solids

The structure of molecular packing in molecular organic solids is determined by intermolecular interactions. These interactions are influenced by forces, which vary in strength and direction.

Fluctuations in the charge distribution within a molecule can give a rise for cohesion forces. These fluctuations induce corresponding dipoles in adjacent molecules, leading to attractive forces known as dispersive or van der Waals forces. This attractive force is described by the induced dipole-dipole potential energy as a function of distance $r$:

$$V_{\text{disp}} = -\frac{A}{r^6}, \tag{2.1}$$

where $A$ is a material-specific parameter. The repulsive forces, which arise from Coulomb repulsion between inner electrons and atomic nuclei, preventing the collapse of the solid structure. These forces are particularly strong at short distances and decrease rapidly as the distance increases.

Repulsive forces are commonly treated using approximations, such as the Lennard-Jones potential, which combines van der Waals interactions with repulsion:

$$V(r) = 4\epsilon \left[ \left( \frac{\sigma}{r} \right)^{12} - \left( \frac{\sigma}{r} \right)^{6} \right], \tag{2.2}$$

where $r$ is the distance between the two particles, $\epsilon$ represents the depth of the potential well, $\sigma$ is the distance at which the potential is zero. The Lennard-Jones

potential is illustrated in Fig. 2.4. For organic solids with molecules containing

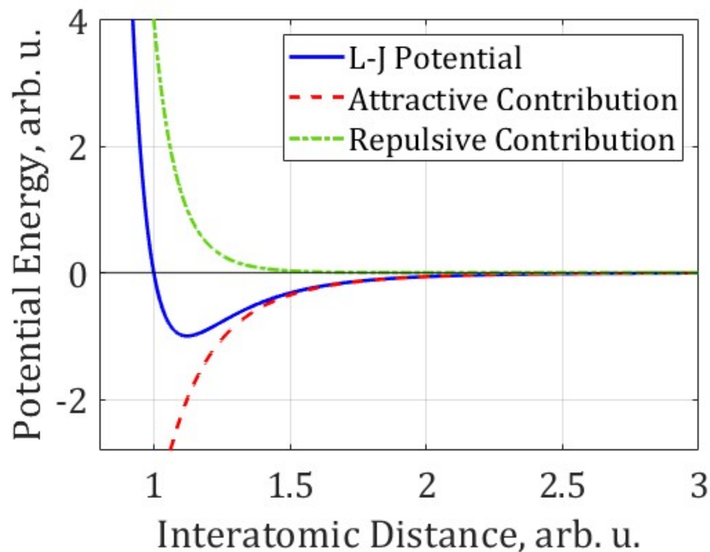


***Figure 2.4:*** *Lennard-Jones potential curve (blue) with attractive (van der Waals, red) and repulsive (green) contributions.*

polar substituents or permanent dipoles, Coulomb forces must also be considered. These interactions can arise from monopoles, dipoles, or quadrupoles, which exhibit long-range effects [51]. The quadrupole moment plays a crucial role in determining the molecular arrangement within a solid because there should be a balance between quadrupole-quadrupole interactions and van der Waals forces. For planar molecules, this interplay gives rise to two primary molecular configurations in a solid composed of identical species, face-to-edge and face-to-face arrangements [52, 53]. The face-to-edge configuration optimizes the attraction between regions of positive and negative partial charges, enhancing electrostatic stabilization. For the slip-stacking arrangement, the molecular stacking is adjusted to balance attractive van der Waals forces with repulsive electrostatic interactions, achieving overall stability [52–54]. A configuration which arises from the both above-mentioned configurations is called a herringbone structure.

Another important intermolecular force in organic solids is the C–H/$\pi$ interaction. This interaction involves both electrostatic and repulsive forces and is significant in the packing of $\pi$-conjugated systems. Further information regarding these interaction types can be found in [52, 55].

## 2.2 Thin film growth

Thin films of organic materials are of high interest for different applications. They are used in semiconductor devices, optical coatings, and many others. The growth of thin films involves various kinetic processes such as adsorption, nucleation,

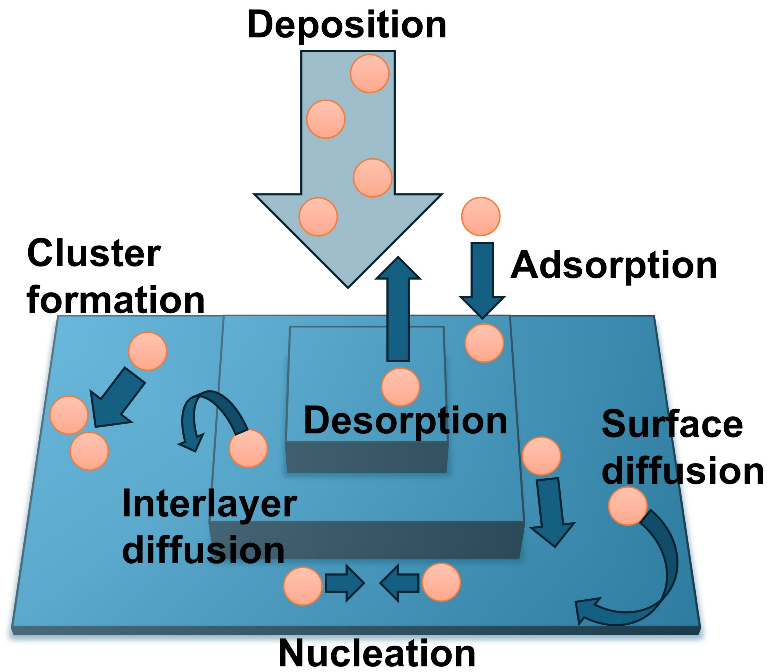


***Figure 2.5:*** *Schematic representation of the atomistic processes occurring during film growth by OMBD. Based on [41].*

surface diffusion, chemical binding, etc. This section provides a brief overview of the key points in thin film growth and is mainly based on Refs. [40, 41, 56, 57]. All other references are explicitly cited.

Organic thin films can be prepared with various methods including laser-induced evaporation [58], physical vapor deposition (PVD) [59], chemical vapor deposition (CVD) [60], ink jet [61], blade-coating [62], spin-coating [63]. In the present study, a particular type of PVD, namely organic molecular beam deposition (OMBD) [38, 41, 56], was employed as the main deposition method due to its versatility and its ability to fully control the growth process. The method itself will be discussed in more detail in Sec. 4.1, while the discussion of the main processes appearing during the growth is given below.

Growth should be viewed as a non-equilibrium process, meaning that models based solely on equilibrium energetics cannot capture all possible growth modes. A dynamic approach is required, incorporating the incoming adsorbate flux and corresponding supersaturation, the probabilities of adsorption and desorption, as well as the relevant diffusion processes, both within and between layers, and the associated energy barriers. In Fig. 2.5 we summarized and present the most important processes that can happen during film growth.

Adsorption is a process where an arriving molecule adheres to the substrate or the pre-existing film at the location where it arrives at the surface. During adsorption, the motion of the molecule is effectively arrested, allowing it to bind to the surface through van der Waals forces or other weak interactions. The high

surface energy has an impact on adsorption, because high-energy surfaces provide more binding sites, enhancing molecular adherence [64].

Nucleation is a fundamental process during thin film growth, describing the initial formation of stable clusters or aggregates of molecules on a substrate. When the interaction potential between individual molecules is attractive - such as van der Waals interactions - the formation of molecular pairs or larger aggregates is energetically favorable [65]. During nucleation, if two molecules encounter each other on the substrate surface after diffusion, they may bind together to form an aggregate. This aggregation significantly reduces their probability of undergoing further diffusion or desorption [66, 67]. The strength of the interaction potential between molecules defines the probability of nucleation. For example, van der Waals forces can promote the aggregation process by providing sufficient attractive energy to stabilize the forming cluster [68].

Desorption (or re-evaporation) occurs when molecules, upon arrival at the substrate or pre-existing thin film, do not attach permanently and instead desorb back into the surrounding environment. Desorption can occur when the substrate temperature is too high or the binding energy is too low [68]. This phenomenon is often observed when the kinetic energy of incident molecules is too high, preventing stable adherence to the substrate or film surface [65, 66]. Desorption is typically undesirable, as it reduces the effective deposition rate and leads to inefficient material usage and non-uniform resulting film. Sometimes desorption does not allow for deposition at all.

Surface diffusion occurs if a molecule that arrived to the sample surface possesses sufficient kinetic energy to diffuse across the surface to find an energetically favorable position. This surface diffusion process is crucial for determining the morphology of the film and can significantly influence the growth dynamics of the thin film [65, 66].

In the case of multilayer growth, molecules often encounter step-edges between different layers during diffusion. If a molecule is situated on a higher layer, it may hop down to the subjacent layer upon overcoming the so-called Ehrlich-Schwoebel barrier (ES) [69, 70]. Alternatively, the molecule can be captured at the step-edge. If the molecule is located on a lower layer, it may either step up to a higher layer, attach to the step-edge, or diffuse along the edge. The probabilities of these processes are defined by the interplay of various interaction energies, including molecule-molecule and molecule-substrate interactions [68]. The diffusion behavior is a key factor in defining the uniformity, grain structure, and overall quality of thin films [71].

There are two types of diffusion that are commonly distinguished. Intralayer diffusion refers to the movement of particles within a single film layer. The diffusion coefficient $D$ quantifies the rate at which particles diffuse across the surface of the film and is given by the equation:

$$D = D_0 \exp\left(-\frac{E_D}{k_B T}\right), \tag{2.3}$$

where $D_0$ is the prefactor, $E_D$ represents the activation energy for diffusion, $k_B$ is the Boltzmann constant, and $T$ is the temperature. The activation energy $E_D$ corresponds to the energy barrier that particles must overcome to change its position. Interlayer diffusion, which involves particle movement between adjacent layers, is influenced by the value of ES barrier $\Delta E_{ES}$. The interlayer diffusion coefficient $D'$ is expressed as:

$$D' = D \exp\left(-\frac{\Delta E_{ES}}{k_B T}\right). \tag{2.4}$$

If $D'$ is smaller than $D$, particles are more likely to remain in their initial layer rather than diffuse to an adjacent one. If $\Delta E_{ES}$ is significantly larger than $E_D$, interlayer diffusion is hindered, resulting in the three-dimensional (3D) growth mode of the thin film.

Notably, the probability of one or another surface process mentioned above is determined by the summation of the factors present in the given system. For instance, the perfectly flat, defects-free, and non-reactive substrate excludes the possibility of dissolution of the incoming molecule into the substrate. Substrate defects such as steps, edges, cracks, impurities, or dislocations act as "traps" and dislocation centers for the molecules and play a significant role in film growth.

### 2.2.1 Growth modes

Thin film growth is a non-equilibrium process and cannot be fully explained only by the equilibrium thermodynamics. Among several approaches to describe growth theories [72–74], we focus on the one that uses the concept of surface and interface energies. The following is a simplified representation of three distinct growth modes in classical equilibrium wetting theory. These growth modes are determined by the interplay between the surface free energies of the substrate ($\gamma_{\text{substrate}}$), the film ($\gamma_{\text{film}}$), and the interfacial free energy ($\gamma_{\text{interface}}$), as well as other influencing factors such as the deposition rate and substrate temperature. These models cannot describe growth completely, because

The three primary growth modes summarized in Fig. 2.6 are as follows:

#### Layer-by-Layer Growth (Frank–van der Merwe)

When

$$\gamma_{\text{film}} + \gamma_{\text{interface}} < \gamma_{\text{substrate}}$$

is satisfied, it becomes energetically favorable for the system to cover (wet) the substrate. If this condition remains valid for subsequent film layers, then the layer-by-layer growth mode is sustained.

In inorganic systems, this type of growth occurs when the atoms of the film are more strongly bound to the substrate than to each other. However, in the case of organic molecules deposited on certain inert substrates, this condition may be

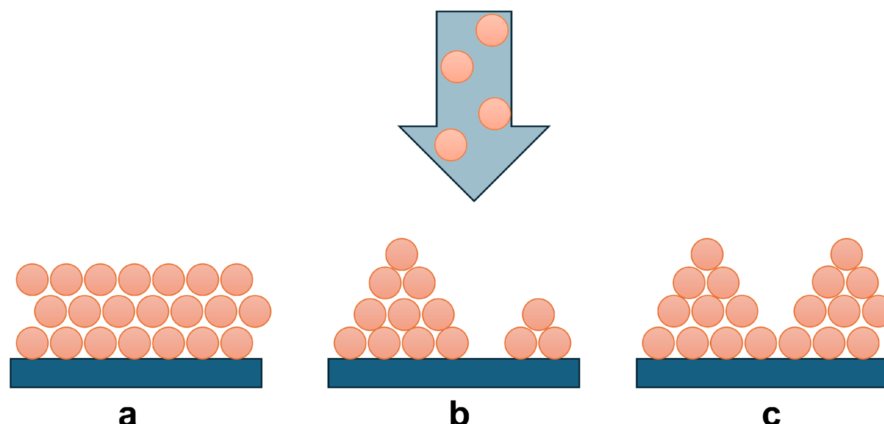


***Figure 2.6:*** *Schematic representation of the different growth modes: Frank-van der Merwe growth (a), Volmer-Weber growth (b), Stranski-Krastanov growth (c). Image adapted from [41].*

reversed due to weaker interactions between organic molecules and the substrate compared to the intermolecular forces [56, 75].

#### Island Growth (Volmer–Weber)

When

$$\gamma_{\text{film}} + \gamma_{\text{interface}} > \gamma_{\text{substrate}},$$

the system energetically favors dewetting, leading to the formation of islands. In this mode, the substrate remains partially uncovered as the film forms discrete clusters. This process typically results in a 3D growth.

#### Layer-plus-Island Growth (Stranski–Krastanov)

This growth mode represents a hybrid of the two modes described above. Initially, one or several wetting layers are formed, followed by a transition to island growth. This transition is driven by differences in substrate–molecule and molecule–molecule interaction energies, which lead to a change from wetting behavior to dewetting behavior.

In addition to surface free energies, variations in the bulk energy of the growing film can also explain this transition. For instance, a bulk energy that changes with increasing film thickness (e.g., due to substrate-induced strain) may drive the system from two-dimensional (2D) layer-by-layer growth to 3D island growth [40, 48, 76].

### 2.2.2 Issues specific to organic thin film growth

Organic molecules, unlike atomic systems, are extended objects with internal degrees of freedom that significantly influence their growth behavior. These

degrees of freedom allow molecules to adopt different orientations during growth, such as lying-down or standing-up orientations, or even aligning at an angle to the surface normal. The molecular orientation has an impact on the macroscopic physical properties of the film [32, 48, 77, 78]. Additionally, organic molecules exhibit vibrational degrees of freedom, which influence the diffusion, adsorption, and interactions with the substrate or neighboring molecules.

The interactions in organic systems are predominantly van der Waals type, which distinguishes them from the stronger interactions typical of inorganic thin films [48]. This distinction allows organic molecules to accommodate more strain, often resulting in higher critical thicknesses for strain-induced changes in growth mode compared to rigid atomic systems [76, 79]. Relatively weak interaction potentials also contribute to polymorphism, which means multiple stable crystal structures coexist within the same film [80]. Furthermore, since van der Waals forces dominate these systems, the temperatures relevant for evaporation and diffusion on the substrate are generally lower. It should be noted, that the total interaction energy of a molecule (when considered over its entire contact area with the surface) can still be quite large. However, on a per-atom basis, the interactions of the organic molecules discussed here are typically weaker.

For van der Waals–bonded crystals made of closed-shell molecules, the absence of dangling bonds at the organic surface results in surface energies that are usually lower than those of inorganic substrates. However, when organic molecules interact with strongly reactive substrates, molecular diffusion can be hindered, leading to films of lower structural order [81]. In extreme cases, highly reactive surfaces may even cause molecular dissociation upon adsorption.

The large size of organic molecules and their associated unit cells introduces additional complexities in growth dynamics. The size mismatch between molecular unit cells and substrate lattices often leads to an increased number of translational domains. Additionally, the low-symmetry crystal structures typical of organic molecules contribute to both translational and orientational domains. These domain boundaries act as sources of disorder, significantly affecting the charge transport properties of the film [32, 82, 83].

The factors outlined above influence not only the static structure of organic thin films but also their growth dynamics. The interactions between molecules and between molecules and the substrate play a crucial role in determining diffusion behavior and the processes that influence film formation.

### 2.2.3 Co-deposition of two organic materials

The growth of thin films produced by co-evaporation of two organic compounds involves interesting effects that are important and applicable particularly for OPV. Understanding the mixing behavior in binary organic systems is crucial, as it directly influences the morphology and crystalline order of the thin films. The mixing behavior of the mixtures depends on several factors, including steric compatibility, molecule-molecule, and molecule-substrate interactions, and experimental

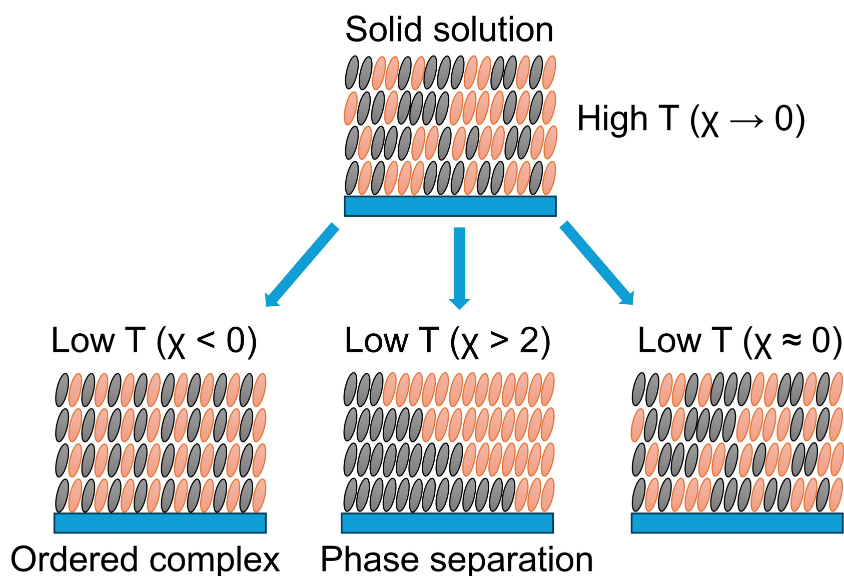


***Figure 2.7:*** *Schematic representation of the different mixing scenarios in binary mixtures. Image adapted from [57].*

conditions, such as substrate temperature and deposition rate. Let us assume that there are two organic compounds A and B evaporated simultaneously. In accordance with the principles of equilibrium thermodynamics and minimization of free energy, the initial consideration is the entropy contribution, which invariably promotes the process of mixing. Secondly, the various interaction energies between the two species, A and B, entering the free energy can either facilitate or hinder the mixing. The free energy of mixing for this system can be expressed using a mean-field approach:

$$\frac{F_{\text{mix}}}{k_B T} = x_A \ln x_A + x_B \ln x_B + \chi x_A x_B, \tag{2.5}$$

where $x_A$ and $x_B$ represent the concentrations of the two materials, while $\chi$ is a dimensionless interaction parameter that depends on the interaction energies between molecules of the same species ($W_{AA}$, $W_{BB}$) and the interaction energy between molecules of different species ($W_{AB}$). This parameter is defined as:

$$\chi = \frac{1}{k_B T} \left[ W_{AA} + W_{BB} - 2W_{AB} \right]. \tag{2.6}$$

This equation does not take into account the steric compatibility of the molecules, which generally plays a significant role in the mixing behavior. Steric compatibility promotes better mixing, while steric incompatibility often results in phase separation. Depending on the value of the interaction parameter $\chi$, three distinct mixing scenarios are possible, as depicted in Fig. 2.7:

- Solid Solution: When $\chi \approx 0$, the interaction energies between different species

are similar to those within the same species, which favors the formation of a solid solution. In such a case, molecules of one species can substitute molecules of the other without disrupting the structural arrangement. This behavior requires a system of two compounds with similar shapes and sizes.

- Phase Separation: When $\chi > 2$, the interaction energies within each material are significantly stronger than those between the two different materials. In such cases, steric incompatibility amplifies the tendency to phase separation, leading to distinct domains of the two materials.

- Ordered Complex: When $\chi < 0$, the interaction energies between different species are stronger than those within the same species, and the materials exhibit good steric compatibility, an ordered complex is likely to form.

Each of these scenarios has important implications for the structural and functional properties of the resulting thin films. Solid solutions can lead to homogeneous mixing at the molecular level, which might be desirable for uniform electronic properties. Phase separation can be advantageous in certain OPV architectures, where distinct donor and acceptor domains enhance charge separation. Examples and further discussions of these behaviors can be found in [30, 84–89].

### 2.2.4 Growth of bilayer thin films

Another approach to depositing two organic materials is the growth of one material on top of another, resulting in a bilayer film. This configuration is common in OPV and organic solar cells [90, 91]. These systems are often fabricated using OMBD (Sec. 4.1), which allows for precise control over film structures. The growth dynamics of the overlayer in such heterostructures is significantly influenced by the properties of the underlying film, with variations arising from differences in interfacial interactions, steric compatibility, and molecular orientation. The simplified schemes of different heterostructures are presented in Fig. 2.8

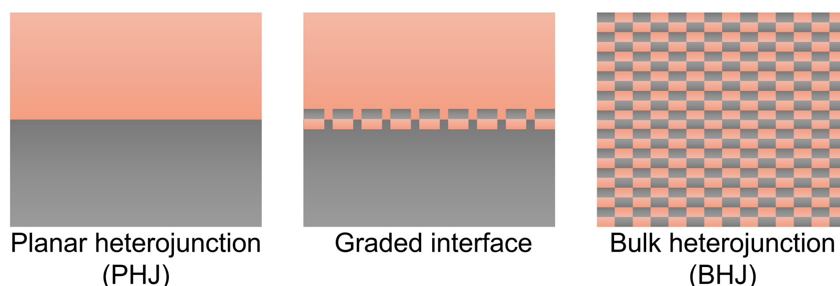


***Figure 2.8:*** *Schematic representation of the different heterostructures occurring in binary systems. Image adapted from [57].*

Interfacial interactions that include van der Waals forces play a central role in determining growth behavior. The steric incompatibility between the two materials

can induce strain during the overlayer growth, while the orientation of molecules in the bottom layer, such as lying-down or standing-up configurations, can strongly influence the arrangement of the overlayer molecules. The resulting overlayer structure can exhibit various growth scenarios. In some cases, an epitaxial-like growth is observed, where the in-plane orientation of the bottom layer is adopted by the overlayer [92]. Examples include - sexithiophene (6T) and para-sexiphenyl (6P), where azimuthal alignment occurs [38, 93–95].

The orientation of molecules in the overlayer often reflects the orientation of the bottom layer. For rod-like molecules, the overlayer may exhibit standing-up or lying-down orientations depending on the alignment of the underlying material [96, 97]. Additionally, the roughness of the surface during the deposition of the second material can evolve in different ways. For instance, surface smoothing can occur if the second material fills voids in the first layer, while in other cases, the roughness may remain unaffected or increase due to factors such as nucleation at step edges or dewetting of the second material [31, 98, 99].

Beyond the growth dynamics of the overlayer, the deposition of a second organic compound can alter the structure of the underlying film. Such reconstructions have been observed in systems such as diindenoperylene (DIP) deposited on fluorinated cobalt-phthalocyanine, where the layers near the interface undergo significant structural changes [100, 101].

## 2.3 X-ray scattering

The whole X-ray scattering section provides basics of the interaction of X-rays with matter and is based on [102, 103]. All other references are explicitly cited.

X-rays are a form of electromagnetic radiation with wavelengths that typically range between $10^{-8}$ and $10^{-12}$ m. Their discovery was done by W.C. Röntgen [104] and is dated back to 1895. It gave rise to many areas of physics and have become an indispensable part of modern science. The short wavelength and relatively weak interaction with matter make the X-rays a powerful tool to explore the atomic structure of matter.

Consider a monochromatic X-ray plane wave, as illustrated in Fig. 2.9. The wave propagates along the $z$-axis, orthogonal to both its electric field $\mathbf{E}$ and magnetic field $\mathbf{H}$. The spatial behavior of the electromagnetic wave at a fixed time is governed by its wavelength $\lambda$ or, equivalently, the wave number $k = 2\pi/\lambda$. In three-dimensional space, the electric field is described by:

$$\mathbf{E}(\mathbf{r}, t) = \hat{\epsilon} E_0 e^{i(\mathbf{k}\cdot\mathbf{r}-\omega t)}, \tag{2.7}$$

where $\hat{\epsilon}$ is the unit vector of polarization, and $\mathbf{k}$ is the wave vector aligned with the propagation direction. The transverse property of electromagnetic waves ensures that $\hat{\epsilon} \cdot \mathbf{k} = 0$, and similarly $\mathbf{k} \cdot \mathbf{E} = \mathbf{k} \cdot \mathbf{H} = 0$. The mutual arrangement of $\mathbf{E}$, $\mathbf{H}$ and $\mathbf{k}$ is presented in Fig. 2.9.

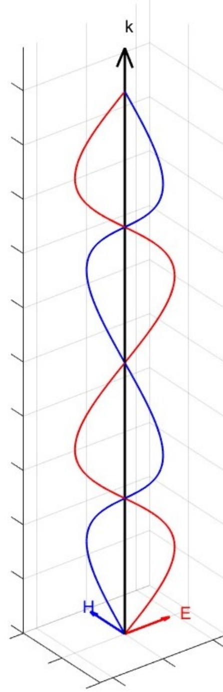


***Figure 2.9:*** *Representation of an electromagnetic wave: the electric field* $\boldsymbol{E}$*, magnetic field* $\boldsymbol{H}$*, and wave vector* $\boldsymbol{k}$ *are mutually perpendicular.*

The relationship between the wavelength $\lambda$ (in Å) and the photon energy $E$ (in keV) of X-rays can be expressed as:

$$\lambda[\text{Å}] = \frac{hc}{\varepsilon} = \frac{12.398}{\varepsilon[\text{keV}]}. \tag{2.8}$$

When an X-ray photon interacts with an atom, it can undergo either scattering or absorption. For cases where X-rays encounter a dense medium consisting of many atoms or molecules, it is often more practical to model the material as a continuous medium with a boundary at the interface with vacuum (or air). At this boundary, the X-ray beam undergoes both refraction and reflection.

## 2.3.1 X-ray scattering on one electron

The simplest example of X-ray scattering is scattering on a single free electron. In order to describe this process, we consider the wavelength of the incident wave to be equal to the wavelength of the scattered one (elastic scattering). The ability of an electron to scatter X-rays is quantified by its scattering length.

A typical scattering experiment is depicted in Fig. 2.10. It is important to emphasize the quantity that is called the *differential scattering cross section*, denoted $\mathrm{d}\sigma/\mathrm{d}\Omega$, which is defined as:

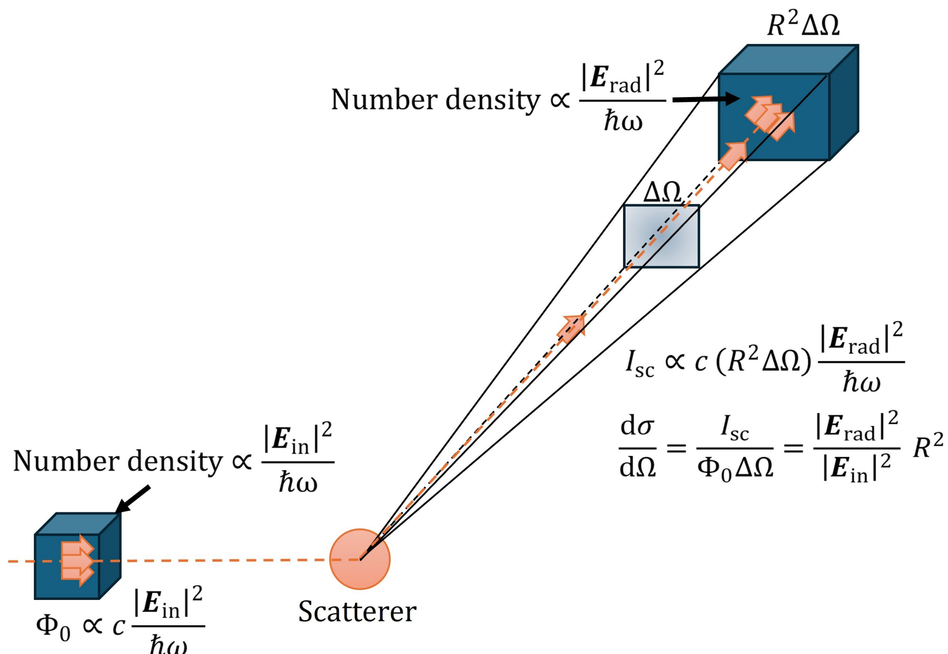


***Figure 2.10:*** *Schematic image depicting a typical scattering experiment used to measure the differential cross-section, as described by Eq. 2.9. The incident beam flux $\Phi_0$ represents the number of particles passing through a unit area per second. For electromagnetic waves, this is proportional to $|E_{in}|^2$ multiplied by the speed of light, c. Upon interaction with the target, the incident beam generates a scattered beam, the intensity of which, $I_{sc}$, is the number of counts detected per second. This intensity is proportional to $|E_{rad}|^2$, the area of the detector, and the speed of light. The detector is positioned at a distance $R$ from the target and covers a solid angle $\Delta\Omega$. Illustration adapted from [102].*

$$\frac{d\sigma}{d\Omega} = \frac{I_{\mathrm{sc}}}{\Phi_0 \Delta\Omega}, \tag{2.9}$$

where the incident beam has a flux $\Phi_0$, representing the number of photons per unit area per second. Photons scattered by the sample are recorded at a detector located at a distance $R$ from the scattering object and subtending a solid angle $\Omega$. The scattered intensity $I_{sc}$ corresponds to the number of scattered photons recorded per second. Thus, the differential cross-section serves as a measure of the scattering efficiency, normalized to the incoming beam to exclude experimental factors such as flux and detector size.

For electromagnetic waves, the incident flux $\Phi_0$ can be expressed in terms of the electric field $\mathbf{E}_{in}$ of the incoming beam. Since the energy density is proportional to $|\mathbf{E}_{in}|^2$, the photon number density scales as $|\mathbf{E}_{in}|^2/\hbar\omega$, and multiplying this by the speed of light $c$ gives the flux. Similarly, the scattered intensity $I_{sc}$ depends on the modulus squared of the radiated electric field $|\mathbf{E}_{rad}|^2$, scaled by the detector area

$R^2\Delta\Omega$ and $c$. These relations lead to the following expression for the differential cross section:

$$\frac{\mathrm{d}\sigma}{\mathrm{d}\Omega} = \frac{|\mathbf{E}_{rad}|^2}{|\mathbf{E}_{in}|^2} R^2. \tag{2.10}$$

When an X-ray beam interacts with an electron, the electron oscillates within the electric field of the incoming wave. This oscillation causes the electron to radiate, producing a spherical wave described by $\mathbf{E}_{rad} \propto \hat{\boldsymbol{\epsilon}}' e^{ikR}/R$, where $\hat{\epsilon}'$ is the polarization of the radiated field. The task is to determine $\mathbf{E}_{rad}$ at an observation point.

The radiated field depends on the electron charge $-e$ and its acceleration $a_X(t')$, where $t' = t - R/c$ accounts for the finite propagation speed of the wave. For an observation point in the plane of the polarization vector and propagation direction of the incoming wave, the radiated field can be expressed as:

$$E_{rad}(R,t) \propto \frac{-e}{R} a_X(t') \sin\theta, \tag{2.11}$$

where $\theta$ is the angle between the observation point and the propagation direction of the incident wave. The factor $\sin\theta$ accounts for variations in acceleration observed at different angles.

Acceleration $\mathbf{a}_X(t')$ can be calculated using the force acting on the electron divided by its mass $m$, yielding:

$$a_X(t') = -\frac{e}{m} E_0 e^{-i\omega t'} = -\frac{e}{m} E_{\mathrm{in}} e^{i\omega \frac{R}{c}} = -\frac{e}{m} E_{\mathrm{in}} e^{ikR}. \tag{2.12}$$

Substituting this into the expression for $E_{rad}$ gives:

$$\frac{E_{\mathrm{rad}}(R,t)}{E_{in}} \propto \frac{e^2}{m} \frac{e^{ikR}}{R} \sin\theta. \tag{2.13}$$

The proportionality constant must have units of length for dimensional consistency. From electrostatics, the Coulomb energy at a distance $r$ is $e^2/(4\pi\epsilon_0 r)$, which can be equated to the relativistic energy $mc^2$ to yield the fundamental length scale:

$$r_0 = \frac{e^2}{4\pi\epsilon_0 mc^2} = 2.82 \times 10^{-5}\,\text{Å}. \tag{2.14}$$

This value is known as the Thomson scattering length or classical electron radius.

The magnitude of the scattering length can be determined by these considerations, but its phase remains undefined. The scattering amplitude for a single electron is expressed as $-r_0\,|\hat{\boldsymbol{\varepsilon}} \cdot \hat{\boldsymbol{\varepsilon}}'|$. The factor of $-1$ arises due to a phase difference of $180°$ between the incoming and scattered waves. This phase difference significantly affects the refractive index $n$, which is less than 1 in the X-ray region.

The relationship between the radiated and incident electric fields is given by

$$\frac{E_{\text{rad}}(R,t)}{E_{\text{in}}} = -r_0 \frac{e^{ikR}}{R} |\hat{\boldsymbol{\varepsilon}} \cdot \hat{\boldsymbol{\varepsilon}}'| \tag{2.15}$$

and using Eq. (2.10), the differential scattering cross-section is written as

$$\left(\frac{\mathrm{d}\sigma}{\mathrm{d}\Omega}\right) = r_0^2 |\hat{\boldsymbol{\varepsilon}} \cdot \hat{\boldsymbol{\varepsilon}}|^2. \tag{2.16}$$

This equation characterizes the Thomson scattering cross section for an electromagnetic wave interacting with a free electron. The term $|\hat{\boldsymbol{\varepsilon}} \cdot \hat{\boldsymbol{\varepsilon}}'|^2$ plays a crucial role in selecting the ideal geometry for various X-ray experiments. For instance, synchrotron radiation produces X-rays polarized in the horizontal plane of the synchrotron. As a result, vertical scattering planes are preferred for experiments, ensuring $|\hat{\boldsymbol{\varepsilon}} \cdot \hat{\boldsymbol{\varepsilon}}'|^2 = 1$ regardless of the scattering angle $\psi$. However, fluorescence studies can minimize scattering by using a horizontal plane at $\psi = 90°$, where $|\hat{\boldsymbol{\varepsilon}} \cdot \hat{\boldsymbol{\varepsilon}}'|^2 = 0$.

To formalize this, the polarization factor $P$ is defined based on the source of the X-rays:

$$P = |\hat{\boldsymbol{\varepsilon}} \cdot \hat{\boldsymbol{\varepsilon}}'|^2 = \begin{cases} 1, & \text{Synchrotron: vertical scattering plane} \\ \cos^2\psi, & \text{Synchrotron: horizontal scattering plane} \\ \frac{1}{2}(1+\cos^2\psi), & \text{Unpolarized source} \end{cases} \tag{2.17}$$

The total cross section for Thomson scattering can be obtained by integrating the differential cross section over all angles. Using the rotational symmetry of the radiation field with respect to $\hat{\varepsilon}$, it is shown that the average value of $< (\hat{\boldsymbol{\varepsilon}} \cdot \hat{\boldsymbol{\varepsilon}}') >^2$ on a sphere is 2/3. Consequently, the total cross section $\sigma_T$ becomes

$$\sigma_T = 4\pi r_0^2 \times \frac{2}{3} = \frac{8\pi r_0^2}{3} = 0.665 \times 10^{-24}\,\mathrm{cm}^2$$

This result reveals that the classical cross section for scattering, both differential and total, remains constant and independent of the wave energy. This property is especially significant in the X-ray region of the electromagnetic spectrum, where photons possess sufficient energy for electrons to behave approximately as if they are free. However, this model fails in the optical regime or when the photon energy exceeds the threshold for resonant excitation of deeply bound atomic states.

### 2.3.2 X-ray scattering on one atom

Initially, we adopt a classical perspective, where the electron density is represented by $\rho(\mathbf{r})$. The scattered radiation field arises as a superposition of contributions from different volume elements within this charge distribution. To calculate this superposition, one must account for the phase of the incident wave as it interacts

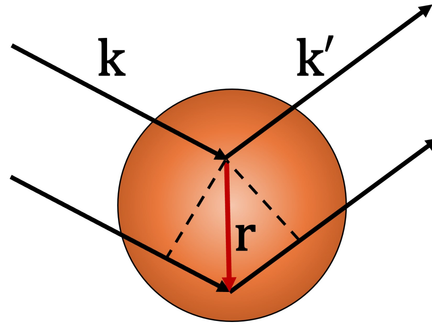


***Figure 2.11:*** *Schematic representation of scattering from an atom. An X-ray with wavevector* $\mathbf{k}$ *is elastically scattered* ($|\mathbf{k}| = |\mathbf{k}'| = 2\pi/\lambda$) *by the electron distribution within an atom, emerging in the direction defined by* $\mathbf{k}'$*. The phase shift of of* $\mathbf{k}' \cdot \mathbf{r} - \mathbf{k} \cdot \mathbf{r} = \boldsymbol{q} \cdot \mathbf{r}$*, defining the wavevector transfer* $\boldsymbol{q}$*. Illustration adapted from [102].*

with the volume element at the origin and another at position $\mathbf{r}$, as illustrated in Fig. 2.11. The phase difference between two successive wave crests is $2\pi$. The phase difference between the contributions of these two elements is $2\pi$ multiplied by the ratio of the projection of $\mathbf{r}$ along the incident direction to the wavelength, which simplifies to the scalar product $\mathbf{k} \cdot \mathbf{r}$. The phase difference between the scattered wave from a volume element around the origin and around $\mathbf{k}$ is $-\mathbf{k}' \cdot \mathbf{r}$. The total phase difference is therefore:

$$\Delta\phi = (\mathbf{k}' - \mathbf{k}) \cdot \mathbf{r} = \mathbf{q} \cdot \mathbf{r}, \tag{2.18}$$

where

$$\mathbf{q} = \mathbf{k}' - \mathbf{k} \tag{2.19}$$

is the scattering vector. For elastic scattering, $|\mathbf{k}| = |\mathbf{k}'|$, and the magnitude of $\mathbf{q}$ is given by $\mathbf{q} = 2|\mathbf{k}|\sin\theta = (4\pi/\lambda)\sin\theta$, where $\theta$ is the angle between the observation point and the propagation direction of the incident wave. The scattering vector $\mathbf{q}$, typically expressed in units of $\text{Å}^{-1}$, is fundamental for describing scattering.

A volume element $\mathrm{d}\mathbf{r}$ at position $\mathbf{r}$ contributes an amount $-r_0\rho(\mathbf{r})\mathrm{d}\mathbf{r}$ to the scattered field, with a phase factor of $e^{-i\mathbf{q}\cdot\mathbf{r}}$. The total scattering length of the atom becomes:

$$-r_0 f^0(\mathbf{q}) = -r_0 \int \rho(\mathbf{r}) e^{-i\mathbf{q}\cdot\mathbf{r}} \mathrm{d}\mathbf{r}, \tag{2.20}$$

where $f^0(\mathbf{q})$ is the so-called atomic form factor. In the limit $\mathbf{q} \to 0$, all volume elements scatter in phase, yielding $f^0(\mathbf{q} = 0) = Z$, the number of electrons in the atom. As $\mathbf{q}$ increases, the volume elements scatter out of phase, and $f^0(\mathbf{q} \to \infty) = 0$.

Atomic electrons are subject to quantum mechanics and exhibit discrete energy

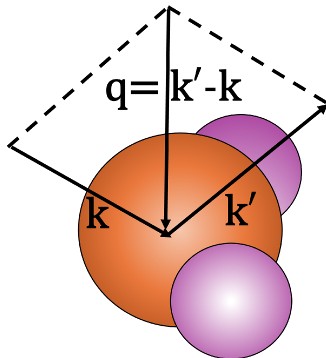


***Figure 2.12:*** *Scattering from a molecule, with the scattering triangle relating* **k**, **k**′, *and* **q**. *Illustration adapted from [102].*

levels. The most tightly bound electrons reside in the $K$-shell, with energies comparable to typical X-ray photons. For X-ray energies much lower than the $K$-shell binding energy, the response of these electrons to an external field diminishes due to their bound state. Electrons in the $L$- and $M$-shells are less tightly bound and respond to the driving field more effectively, but the scattering length of an atom should be reduced by some amount which is denoted $f'$.

At very high energies, the electrons behave as if they were free, rendering $f'$ negligible. For intermediate energies, $f'$ exhibits resonant behavior near the absorption edges. The response of the electron is also expected to have a phase lag with respect to the driving field. The allowance for this is facilitated by the introduction of the term $if''$, which is analogous to dissipation in forced harmonic oscillators and accounts for absorption. The atomic form factor, incorporating dispersion corrections, is given by:

$$f(\mathbf{q}, \hbar\omega) = f^0(\mathbf{q}) + f'(\hbar\omega) + if''(\hbar\omega), \tag{2.21}$$

where $f'$ describes the suppressed scattering and $f''$ describes absorption by the atom. Both $f'$ and $f''$ are independent of $\mathbf{q}$, but depend heavily on the X-ray energy $\hbar\omega$ near the absorption edge of the particular chemical element.

### 2.3.3 X-ray scattering on one molecule

The next logical step in complexity involves molecules, which are assemblies of atoms (Fig. 2.12). Labeling the atoms in the molecule with the index $j$, the molecular scattering amplitude can be expressed as:

$$F_{\text{mol}}(\mathbf{q}) = \sum_j f_j(\mathbf{q}) e^{-i\mathbf{q}\cdot\mathbf{r}_j}, \tag{2.22}$$

where $f_j(\mathbf{q})$ represents the atomic form factor for the $j$-th atom in the molecule. As in previous discussions, the factor of $-r_0$ must be included when calculating absolute intensity values.

If experimental data for $|F_{\text{mol}}(\mathbf{q})|^2$ are available in a sufficiently wide range of scattering vectors $\mathbf{q}$, it is theoretically possible to determine the atomic positions $\mathbf{r}_j$ within the molecule. However, the scattering length of a single molecule is typically far too small to yield a detectable signal, even with the high-intensity X-ray beams provided by modern synchrotron sources. However, at X-ray free electron laser (XFEL) facilities a single-molecule imaging is possible.

To overcome this limitation, measurements are made on bulk samples containing many molecules. These samples can be organized in either non-crystalline (amorphous) or crystalline forms.

### 2.3.4 X-ray scattering on crystal

Let us examine a crystal, which is defined as a periodic and ordered arrangement of entities such as atoms, ions, molecules, or even macroscopic particles. This structure exhibits long-range order and is characterized by pronounced anisotropy and distinct symmetries, as illustrated in Fig. 2.13. In basic treatments of X-ray scattering from a crystal lattice, Bragg's law is introduced [105]:

$$n\lambda = 2d \sin\theta, n \in \mathbb{N}. \tag{2.23}$$

This equation establishes the condition for constructive interference of X-rays incident at an angle $\theta$ on lattice planes spaced a distance $d$ apart. While useful for identifying diffraction conditions, Bragg's law alone does not provide information about the intensity of the scattered X-rays under these conditions.

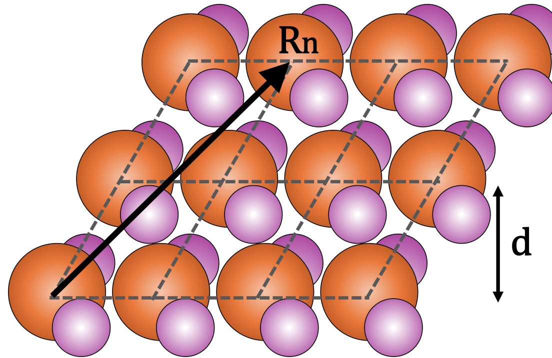


***Figure 2.13:*** *Scattering from a molecular crystal, where molecules are arranged on a lattice with position vectors $\mathbf{R}_n$. A lattice plane spacing is denoted by $d$. Illustration adapted from [102].*

To calculate the scattering intensity, we must extend our analysis by considering the scattering amplitude of the crystal. A crystal structure is defined by a periodic lattice of points, $\mathbf{R}_n$, reflecting its symmetry, and a unit cell containing atoms placed at $\mathbf{r}_j$ relative to a lattice point. The position of any atom in the crystal is thus given by $\mathbf{R}_n + \mathbf{r}_j$. The total scattering amplitude can then be expressed as:

$$F_{\text{crystal}}(\mathbf{q}) = \underbrace{\sum_j f_j(\mathbf{q}) e^{-i\mathbf{q}\cdot\mathbf{r}_j}}_{\text{Unit cell structure factor}} \underbrace{\sum_n e^{-i\mathbf{q}\cdot\mathbf{R}_n}}_{\text{Lattice sum}}. \tag{2.24}$$

The first term is the structure factor of the unit cell, and the second term is the sum over all lattice sites.

In Eq. 2.24, the terms in the lattice sum are phase factors in the unit circle in the complex plane. The sum is negligible unless the scattering vector satisfies the condition:

$$\mathbf{q} \cdot \mathbf{R}_n = 2\pi \times \text{integer} \tag{2.25}$$

at which point the sum scales with $N$, the number of unit cells. Lattice vectors $\mathbf{R_n}$ can be expressed as:

$$\mathbf{R_n} = n_1\mathbf{a}_1 + n_2\mathbf{a}_2 + n_3\mathbf{a}_3, \tag{2.26}$$

where $\mathbf{a}_1, \mathbf{a}_2, \mathbf{a}_3$ are the basis vectors, and $n_1, n_2, n_3$ are integers. To solve Eq. 2.25, we introduce the reciprocal lattice, defined by the basis vectors:

$$\mathbf{a}_1^* = 2\pi \frac{\mathbf{a}_2 \times \mathbf{a}_3}{\mathbf{a}_1 \cdot (\mathbf{a}_2 \times \mathbf{a}_3)}, \tag{2.27}$$

$$\mathbf{a}_2^* = 2\pi \frac{\mathbf{a}_3 \times \mathbf{a}_1}{\mathbf{a}_1 \cdot (\mathbf{a}_2 \times \mathbf{a}_3)}, \tag{2.28}$$

$$\mathbf{a}_3^* = 2\pi \frac{\mathbf{a}_1 \times \mathbf{a}_2}{\mathbf{a}_1 \cdot (\mathbf{a}_2 \times \mathbf{a}_3)}. \tag{2.29}$$

Any reciprocal lattice vector $\mathbf{G}$ can be written as:

$$\mathbf{G} = h\mathbf{a}_1^* + k\mathbf{a}_2^* + l\mathbf{a}_3^*, \tag{2.30}$$

where $h, k, l$ are integers. The scalar product of $\mathbf{G}$ and $\mathbf{R}_n$ simplifies to:

$$\mathbf{G} \cdot \mathbf{R_n} = 2\pi(hn_1 + kn_2 + ln_3) = 2\pi \times \text{integer} \tag{2.31}$$

Thus, the condition for non-zero $F_{\text{crystal}}(\mathbf{q})$ is that $\mathbf{q}$ matches a reciprocal lattice vector:

$$\mathbf{q} = \mathbf{G}. \tag{2.32}$$

This is the Laue condition for diffraction, equivalent to Bragg's law.

Diffraction from a crystal occurs only at discrete points in reciprocal space, with intensity proportional to the squared magnitude of the unit cell structure factor. From a sufficiently large set of Bragg peak intensities, the atomic positions in the unit cell can be determined. This approach has profoundly influenced the determination of molecular structure, with over 95 % known molecular structures

derived from X-ray diffraction studies. Complex cases, such as proteins or viruses, may require tens of thousands of diffraction reflections and sophisticated analysis techniques to reconstruct the molecular structure.

### 2.3.5 X-ray refraction and reflection

The interaction of X-ray photons with matter has primarily been discussed at the atomic scale thus far. However, given that X-rays are electromagnetic waves, refraction phenomena at the interfaces between different media must also be considered. To describe such phenomena, the media are assumed to be homogeneous with distinct boundaries, each characterized by a specific refractive index $n$. By convention, the refractive index of a vacuum is taken as unity.

For visible light in materials such as glass, $n$ can vary significantly, typically ranging between 1.5 and 1.8 depending on the glass type. This variation facilitates the design of lenses to focus light and produce magnified images. In contrast, the deviation of $n$ from unity for X-rays is extremely small, it is around the order of $10^{-5}$ in solids and approximately $10^{-8}$ in air. The refractive index for X-rays can generally be expressed as:

$$n = 1 - \delta + i\beta, \tag{2.33}$$

where $\delta$ (the real part) is of the order $10^{-5}$, and $\beta$ (the imaginary part) is typically much smaller.

The fact that the real part of $n$ is slightly less than one arises from the positioning of the X-ray spectrum on the high-frequency side of various electronic resonances. A direct consequence of this is that the phase velocity inside the material, $c/n$, exceeds the speed of light in a vacuum, $c$. However, this does not violate the principles of relativity, which stipulate that only information-carrying signals travel at the group velocity, which remains less than $c$.

The relationship between the incident grazing angle $\alpha$ and the refracted grazing angle $\alpha'$ is described by Snell's law:

$$\cos\alpha = n\cos\alpha'. \tag{2.34}$$

Since $n < 1$, total external reflection occurs below a critical angle $\alpha_c$, where $\alpha' = 0$. By expanding the cosine term in Snell's law and assuming $\beta = 0$, the critical angle can be approximated as:

$$\alpha_c = \sqrt{2\delta}. \tag{2.35}$$

For $\delta \approx 10^{-5}$, $\alpha_c$ is on the order of hundredths of a degree.

Total external reflection has several key implications for X-ray physics. First, it enables the construction of focusing optics using curved reflective surfaces.

Second, for grazing angles $\alpha < \alpha_c$, an evanescent wave is generated within the medium. This wave propagates normal to the interface and decays exponentially with depth, typically penetrating only a few nanometers into the material. For grazing angles several times $\alpha_c$, the penetration depth extends to several

micrometers.

The limited penetration of X-rays at angles below $\alpha_c$ enhances their sensitivity to surface and near-surface regions. This makes X-rays a suitable tool for investigating the structural and compositional properties of surfaces and interfaces in detail.

# Part II

# Materials & Methods

**Chapter 3**

# Materials

The focus of this thesis is to investigate the growth of thin films of the new semiconductor material dbSeQ and its heterostructures with well-studied OSCs such as DIP and PEN. This chapter provides information about these materials.

## 3.1 Dibenzoselenadiazoloquinoxaline (dbSeQ)

Dibenzo[f,h][1,2,5]selenadiazolo[3,4-b]-quinoxaline (dbSeQ, $C_{16}H_8N_4Se$) is a promising OSC with acceptor properties and is of prime interest in this work. The synthesis of dbSeQ was done by direct exchange of the sulfur atom of the corresponding 1,2,5-thiadiazole by a selenium atom and is described in more detail in [106, 107]. The molecule of dbSeQ depicted in Fig. 3.1 contains two benzene

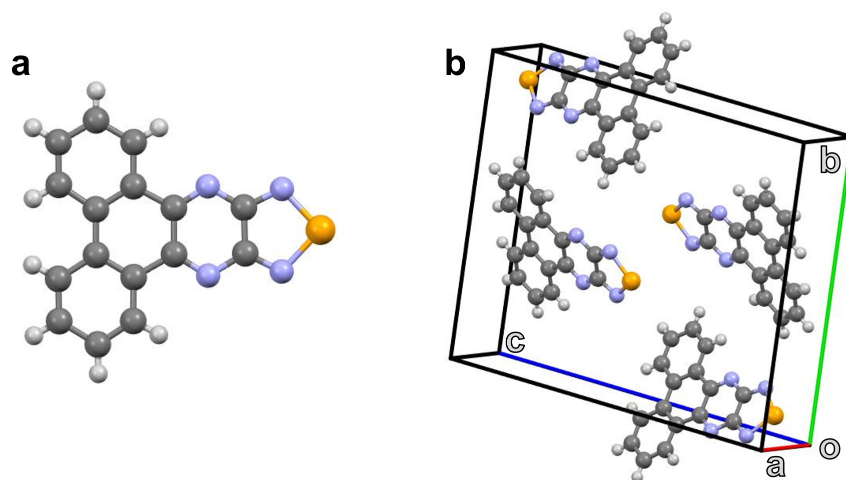


***Figure 3.1:*** *Molecular structure of dbSeQ (a). Unit cell of the dbSeQ (b).*

rings fused to a central core consisting of a quinoxaline and a selenadiazole ring [108, 109]. The molecular weight of dbSeQ equals 335.22 g/mol. The unit cell of dbSeQ is monoclinic and contains four molecules with two conformationally different ones, as pictured in Fig. 3.1 b). The parameters of the unit cell are listed in Tab. 3.1

The dbSeQ used in this study was synthesized and provided by the group of Prof. Zibarev (Novosibirsk Institute of Organic Chemistry) and was used as received

*Table 3.1: Unit cell parameters for the dbSeQ.*

| $a$ [Å] | $b$ [Å] | $c$ [Å] | $\alpha$ [°] | $\beta$ [°] | $\gamma$ [°] |
|---|---|---|---|---|---|
| 3.88 | 15.85 | 20.33 | 90 | 90.567 | 90 |

without further purification.

## 3.2 Diindenoperylene (DIP)

Diindenoperylene (DIP, $C_{32}H_{16}$) is an OSC that was used as a donor material in this thesis. It is a planar derivative of perylene [110], which consists of a perylene core with two indeno-groups attached at the ends as depicted in Fig. 3.2 a). The approximate dimensions of the single molecule are 18.4 Å and 7 Å.

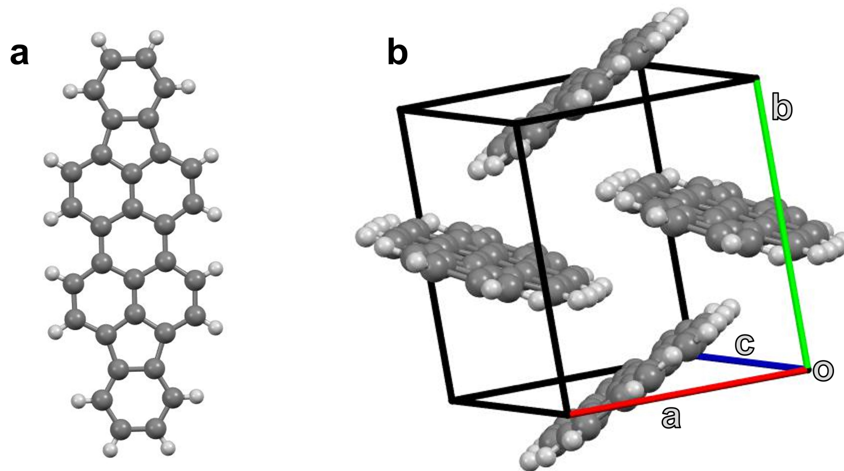


***Figure 3.2:*** *Molecular structure of DIP (a). The thin-film phase unit cell showing the herringbone structure [111] (b).*

DIP crystallizes in a herringbone structure (Fig. 3.2 (b)) and undergoes a reversible structural phase transition between two bulk crystal phases based on temperature. At lower temperatures, DIP adopts the low-temperature $\alpha$-phase, characterized by a triclinic unit cell containing four molecules with two conformers. The high-temperature (HT) $\beta$-phase is characterized by a monoclinic unit cell that contains two nearly planar molecules.

In thin films, the structural arrangement of DIP varies depending on the choice of substrate and substrate temperature. At $T_{sub} \approx 400$ K on weakly interacted substrates, DIP molecules form an ordered polycrystalline structure with nearly upright-standing molecules, referred to as the $\sigma$-phase [112]. The unit cell of the $\sigma$-phase, depicted in Figure 3.2, resembles the HT-phase of the bulk crystals [113].

The lattice parameters for the different DIP structures are summarized in Tab. 3.2.

***Table 3.2:*** *Unit cell parameters for the different DIP structures.*

| Phase | $a$ [Å] | $b$ [Å] | $c$ [Å] | $\alpha$ [°] | $\beta$ [°] | $\gamma$ [°] |
|---|---|---|---|---|---|---|
| $\alpha$-phase [111] | 11.66 | 13.01 | 14.97 | 98.44 | 98.02 | 114.55 |
| $\beta$-phase [111] | 7.17 | 8.55 | 16.8 | 90 | 92.42 | 90 |
| $\sigma$-phase [113] | 7.09 | 8.67 | 16.9 | 90 | 92.2 | 90 |

For low substrate temperatures and metal substrates, a new phase with lying-down molecules (the long molecular axis is parallel to the substrate) emerges known as the $\lambda$-phase. This phase coexists with the $\sigma$-phase after a certain film thickness and shares the same unit cell parameters [114, 115]. The $\lambda$-phase becomes more prevalent at lower temperatures.

DIP growth behavior in thin films is well established [30, 79, 113, 116, 117] and begins with layer-by-layer growth, followed by a sudden transition to island growth, which depends on temperature, growth rate, and substrate. Island formation begins after 3-5 monolayers of layer-by-layer growth [118, 119].

DIP used in this work was received purified by gradient sublimation from the University of Stuttgart, Germany.

## 3.3 Pentacene (PEN)

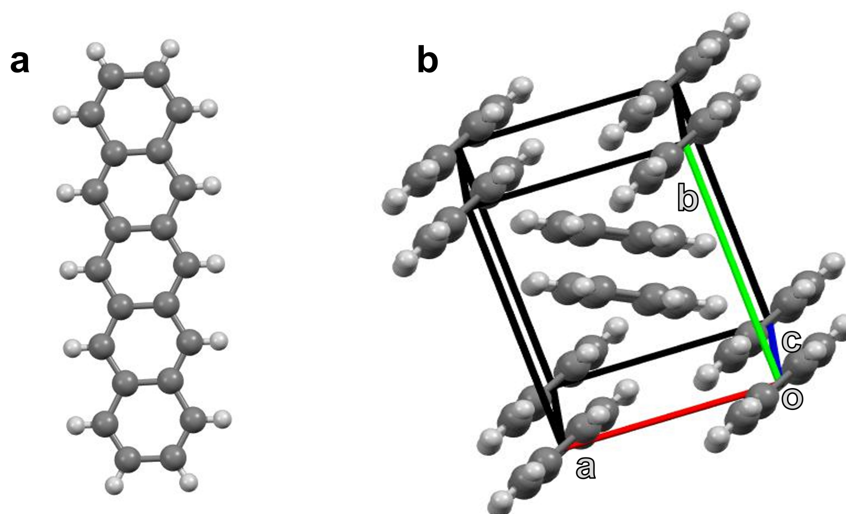


***Figure 3.3:*** *Molecular structure of PEN (a). The thin-film phase unit cell showing the herringbone structure [120] (b).*

Pentacene (PEN, $C_{22}H_{14}$) is another OSC used in this work as a donor material. Due to its prominent properties, such as high charge carrier mobility [121], PEN

is one of the most thoroughly studied OSCs [122–128]. It is a planar molecule that consists of five linearly connected benzene rings, resulting in an approximate length of 16.5 Å [129].

Similarly to other OSCs, depending on substrate temperature and film thickness, several polymorphs have been observed in both thin films and single crystals for PEN [80, 130]. At room temperature, PEN crystallizes in a herringbone structure with a triclinic unit cell containing two molecules per cell.

The thin films of PEN grown on $SiO_x$ exhibit three phases: a Holmes (or bulk) phase, Campbell phase, and thin film phase. The out-of-plane lattice spacings ($d_{001}$) for these phases are not equal: 14.44 Å for the Holmes phase, 16.01 Å for the Campbell phase and 15.61 Å for the thin-film phase, respectively [83, 131, 132]. The growth of PEN films exhibits a Stranski-Kastranov growth, with rapid roughening, characterized by the formation of 3D islands after initial layer-by-layer growth [133, 134]. The unit cell parameters for the PEN structures are listed in Tab. 3.3.

***Table 3.3:*** *Unit cell parameters for various PEN structures.*

| Phase | $a$ [Å] | $b$ [Å] | $c$ [Å] | $\alpha$ [°] | $\beta$ [°] | $\gamma$ [°] |
|---|---|---|---|---|---|---|
| Campbell-phase [83] | 7.90 | 6.06 | 16.01 | 101.9 | 112.6 | 85.8 |
| Holmes-phase [135] | 6.27 | 7.71 | 14.44 | 76.75 | 88.01 | 84.52 |
| Thin-film phase [120] | 5.96 | 7.6 | 15.61 | 81.25 | 86.56 | 89.80 |

The PEN used in this thesis was obtained from Sigma-Aldrich with a purity of 99.9 % and used without further purification.

Chapter 4

# Experimental Methods

This chapter provides a brief overview of the experimental methods used in this work. We will discuss fabrication of thin films and their characterization with various techniques.

## 4.1 Organic molecular beam deposition (OMBD)

In this work, we used organic molecular beam deposition (OMBD) to prepare thin films of the studied OSCs. This deposition method is based on controlled thermal sublimation and subsequent condensation of the organic material on the substrate in a vacuum environment. The evaporation of the material (normally in a form of fine powder) takes place in the Knudsen cell which consists of a ceramic, heat-resistant crucible and tantalum wire, which serves as a heating element wrapped around it [136, 137]. By changing the current through the wire, a deposition rate of the material can be altered. A significant component of the evaporation cell is the shutter positioned above the crucible serving as a switch for a particle flux when the cell is in operation.

After heating, molecules are sublimed and travel towards the substrate, where they are adsorbed and can form a thin film as described in Sec. 2.2. The importance of vacuum in the deposition process cannot be underestimated. The role of vacuum during film formation is multifaceted. Firstly, it serves to minimize contamination on the substrate surface and within the chamber. Secondly, it is used to prevent oxidation of the deposited material. Finally, it ensures that molecules travel ballistically from the crucible to the substrate. To achieve the best results, the base and operational pressures during growth were kept below $10^{-8}$ mbar, which corresponds to ultra-high vacuum conditions (UHV).

The simplest vacuum chamber setup to achieve the UHV can be built by combination of the pre-vacuum and turbomolecular pumps connected one after another. Pre-vacuum pumps allow to create the initial vacuum down to $10^{-3}$ mbar and the subsequent switch of the turbomolecular pump (TMP) allows to reach high and ultra-high vacuum ranges. Among the variety of pre-vacuum pumps, oil rotary pumps and membrane pumps were used in this work. The working principle of both pumps lies in the mechanical transfer of the gas from the main chamber to the exhaust of the pump. The TMP functions by using the principle of transferring kinetic energy from a series of rapidly rotating blades to the

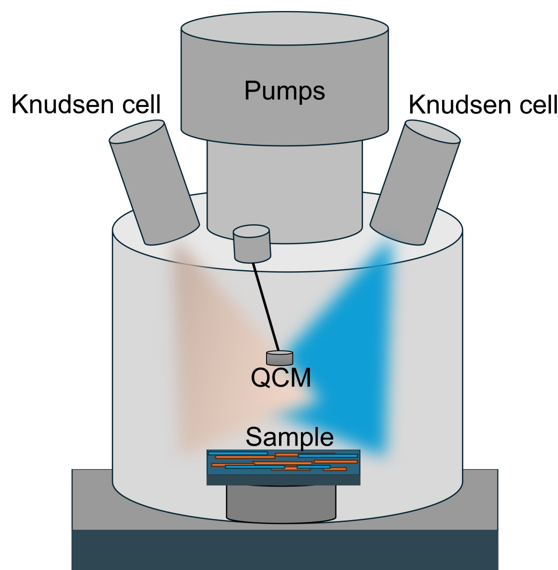


***Figure 4.1:*** *A schematic representation of a standard configuration for OMBD employed in the context of film deposition. The low pressure is achieved by a system of pumps, allowing the molecules sublimed in Knudsen cells travel ballistically onto the substrate surface where they can be adsorbed. A QCM is located on the way of particle beam to ensure precise monitoring of film thickness. Substrate is mounted on a sample holder that connected to the heater/cooler, enabling precise regulation of its temperature.*

contamination molecules. The shape of the blades and their mutual arrangement are constructed in such a manner that the impacted molecules are directed outside the chamber. For one of the vacuum chambers used in the work, we used an ion getter and titanium sublimation pumps. The ion getter pump (IGP) operates by ionizing gas molecules through a strong electric field, typically in the range of 3 to 7 kV, and capturing the resulting ions on chemically reactive cathodes. The titanium sublimation pump (TSP) functions by applying the current and subsequent evaporation of the titanium filament inside the vacuum chamber. In result, a thin layer of titanium is deposited on the chamber walls, providing a chemically active surface for adsorbing and binding contamination gas molecules such as oxygen, nitrogen, and hydrogen. Such systems with all the pumps mentioned above are well suited to achieve and maintain UHV conditions, with pressures as low as $10^{-13}$ mbar.

To control the deposition rate and film thickness, a quartz crystal microbalance (QCM) is placed in the molecular beam. The main element in QCM is a quartz crystal that oscillates at a high frequency, usually several $MHz$, and upon arrival of the particles on its surface, it changes the oscillation frequency. The QCM should be calibrated prior to the main deposition, and in scope of this work it was done by combination of X-ray reflectivity (Sec. 4.4), ellipsometry and atomic force microscopy (Sec. 4.2) techniques. If two or more materials are deposited, QCM

should be installed on the beam path for all materials. Moreover, it should be calibrated for each material separately because the evaporation cells are normally located in different places inside the vacuum chamber, which affects the QCM readings. The schema of the vacuum chamber is presented in Fig. 4.1.

## 4.2 Atomic Force Microscopy (AFM)

This section is based on Refs. [138–140], all other references are explicitly cited.

Invented in 1986 by Binnig et al. [141], atomic force microscopy (AFM) is a versatile tool that allows the characterization of surfaces at the atomic scale. The working principle of AFM is based on the short-range interaction forces between a sharp nanoscale tip and the surface of a sample. These interactions generate adhesion forces on the order of $10^{-9}$ to $10^{-10}$ N. The highly sensitive detection systems are used to measure such tiny forces, utilizing complex optical mirror arrangements in combination with a laser beam, to detect the response of the cantilever with high precision. The basic setup for an AFM measurement is illustrated in Fig. 4.2.

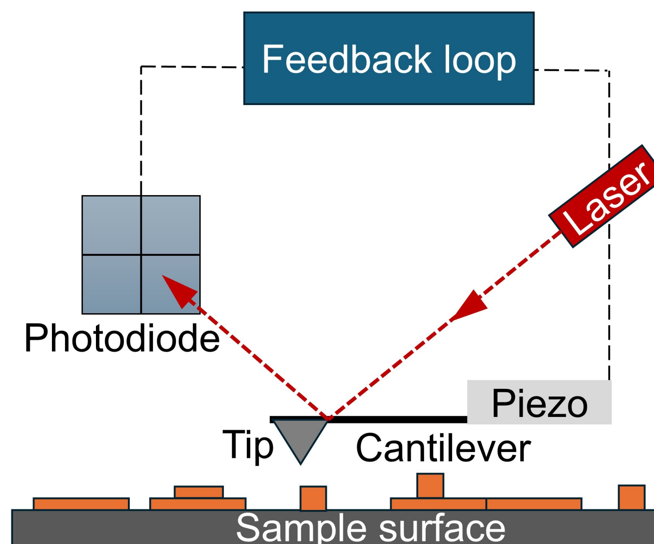


***Figure 4.2:*** *Schematic representation of the working principle of an AFM. A laser beam reflects off the back of the cantilever onto a four-quadrant photodetector. The deflection of the cantilever caused by tip-sample interaction is recorded to create a high-resolution image of the surface.*

The core components of an AFM system are the tip, which acts as the probe, and the cantilever to which it is attached. The tip, typically fabricated from silicon or silicon nitride ($Si_3N_4$), is a few micrometers long and shaped like a cone or pyramid. Its geometry, particularly the radius of curvature and apex angle, directly influences the lateral resolution of the measurements. The deflection of

the cantilever under force $F$ obeys Hooke's law $F = -kx$, making it sensitive to the minute forces arising from tip-surface interactions.

AFM measurements exploit the principle of the optical lever to detect cantilever deflection. A laser beam, reflected off the metallic-coated back surface (typically aluminum or gold), is projected onto a photodetector. Small deflections of the cantilever are amplified by the long optical path of the laser, allowing for high-resolution detection of surface features. A four-quadrant photodiode is commonly used to monitor the laser spot position, enabling accurate determination of vertical and lateral displacements.

AFM can operate in several scanning modes, each tailored to specific materials and applications. These modes are categorized based on the tip-surface interaction potential range:

- Contact Mode: The tip remains in continuous contact with the surface, measuring forces directly. This mode is suitable for hard surfaces, but may damage soft films due to shear forces.
- Intermittent Contact Mode (Tapping Mode): The cantilever oscillates near its resonance frequency, periodically touching the surface. This mode minimizes damage to delicate films while maintaining high sensitivity, making it ideal for studying molecular thin films.
- Non-Contact Mode: The tip oscillates above the surface, detecting long-range attractive forces. This mode is less commonly used for molecular films because of the reduced resolution.

The most widely used mode for organic thin films is tapping mode, where the cantilever alternates between attractive and repulsive interaction regions. This oscillation reduces tip-sample contact time, lowering the risk of damage while achieving nanometer-scale resolution. The surface height profiles $z(x, y)$ are reconstructed by tracking the voltage signal required to maintain a constant oscillation amplitude.

AFM imaging is subject to several technical challenges that must be addressed for reliable measurements:

- Vibrations: Environmental and thermal vibrations can compromise image stability. Anti-vibration tables or isolation systems are essential to reduce such disturbances.
- Humidity: A water film often forms on the sample under ambient conditions, complicating the tip approach.
- Tip artifacts: Damaged or contaminated tips can produce artifacts in the images. Surface profiles represent a convolution of the tip shape with the actual morphology. Regular inspection and replacement of tips are necessary to ensure accuracy.

- Scan settings: Inappropriate settings, such as overly fast scanning on rough surfaces, can degrade image quality or transfer material between surface regions.

In this thesis, AFM measurements were conducted using a Nanowizard-II AFM system from JPK/Bruker. Data visualization and analysis were performed using the open-source software Gwyddion [142]. This software provides a wide range of tools for image processing, including background correction, leveling, and statistical analysis of surface, enabling detailed examination of the obtained AFM data.

## 4.3 Scanning Electron Microscopy (SEM)

Scanning electron microscopy (SEM) is a powerful microscopy method that was used as a complementary technique to AFM. Initially introduced by Knoll in 1935 [143], SEM provides several advantages compared to AFM, offering faster imaging while enabling the characterization of larger areas. It operates by scanning a focused beam of high-energy electrons across the surface of a sample. SEM is particularly effective for detecting features such as protruding needles on thin films, which AFM might miss due to the physical interaction of the tip with the surface. Concurrently, the SEM provides a limited resolution in the direction along the electron beam (i.e. normal to the substrate in most cases).

Initially, the electron beam is generated by the electron gun (Fig. 4.3). The most widely used types of electron guns are thermionic emission guns (TEG) and field emission guns (FEG) [144, 145]. The emitted electrons are accelerated by applying a high voltage (typically between 5 and 30 kV) between the cathode and the anode, forming a high-energy electron beam. The beam is then directed through a series of lenses, diaphragms, and deflectors that focus and guide it onto the sample surface. The focus and spot size of the electron beam are critical for achieving high resolution. The focused electron beam is deflected by scanning coils that control the raster scanning of the beam over the sample surface. This movement allows the SEM to probe different areas of the sample line-by-line [146]. As the electron beam interacts with the sample, it generates various signals, including:

- Secondary Electrons (SE): These are low-energy electrons ejected from the sample surface atoms as a result of inelastic scattering. Secondary electrons provide information on the surface topography [147].
- Backscattered Electrons (BSE): These are high-energy electrons that are elastically scattered back out of the sample. The intensity of backscattered electrons depends on the atomic number of elements in the sample, providing a compositional contrast [146].
- X-rays: Characteristic X-rays are emitted when inner-shell electrons are ejected, and outer-shell electrons fall into the lower energy state. This

process, known as energy-dispersive X-ray spectroscopy (EDS), provides information on the elemental composition [144].

The specimen chamber and beam column are evacuated under high vacuum conditions ($10^{-6}$ mbar in the chamber and $10^{-8}$ to $10^{-9}$ mbar in the column) to minimize contamination and allow precise measurements. The various signals generated by electron-sample interactions are then collected by the corresponding detectors, particularly the secondary and backscattered electrons, which are captured by the Everhart-Thornley detector [148]. The detected signals are converted into electrical signals, amplified, and processed to form an image on a monitor. The intensity of each pixel in the image corresponds to the signal detected at that point on the sample.

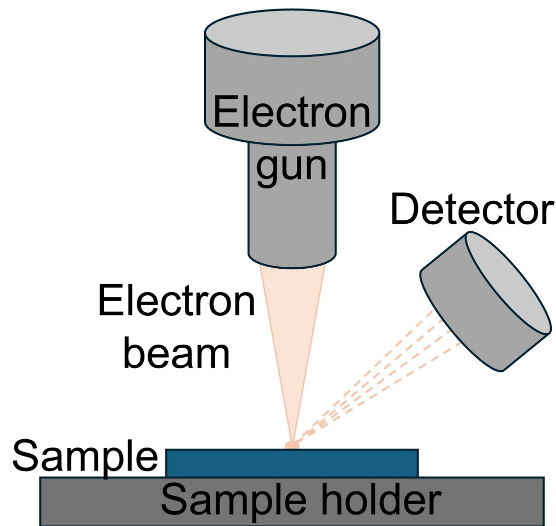


***Figure 4.3:*** *Illustration of a typical SEM setup. Electron gun generates and focuses a beam over the sample surface, and backscattered electrons are captured by the detector.*

In the context of SEM imaging, the presence of contrast effects is a key factor in the generation of a 3D-like effect. These effects arise from various phenomena, namely the inclination, edge, and shadowing effects [149].

In this study, a Philips XL30 SEM system was used, operating with an electron beam accelerated by a high voltage of 20 kV.

## 4.4 X-ray Reflectivity (XRR)

X-ray reflectivity (XRR) is a non-destructive analytical technique used to determine the structural properties of thin films and layered materials, such as thickness, electron density, and surface roughness. XRR provides insight into the electron density profile of a sample along the direction perpendicular to the substrate. A

specular reflection geometry is used for XRR measurements, where the out-of-plane momentum transfer, $q_z$, is probed (see Fig. 4.4) by keeping the same values of the incoming and detector angles ($\theta$ and $\Omega$, respectively). In this configuration, in general, the reflectivity deviates from the Fresnel reflectivity, which assumes perfectly flat interfaces. In practice, imperfections in interface flatness lead to additional off-specular contributions [150, 151].

The basic setup for XRR involves directing a monochromatic X-ray beam onto a sample at a shallow angle of incidence ($\theta$), typically below 0.5°. At these small angles, X-rays undergo total external reflection due to the refractive index of the materials for X-rays being slightly less than unity [102].

The reflected intensity $I$ is measured as a function of the incidence angle $\theta$. The intensity of the reflected beam decreases exponentially with increasing angle beyond the critical angle for total reflection. Reflectivity $R(\theta)$ is defined as the ratio of reflected intensity to incident intensity, $R(\theta) = I_{\text{ref}}(\theta) \cdot I_{\text{inc}}^{-1}$. The critical angle $\theta_c$ for total reflection is determined by the electron density of the material and can be described by $\theta_c = \sqrt{2\delta}$, where $\delta$ is the real part of the refractive index [152].

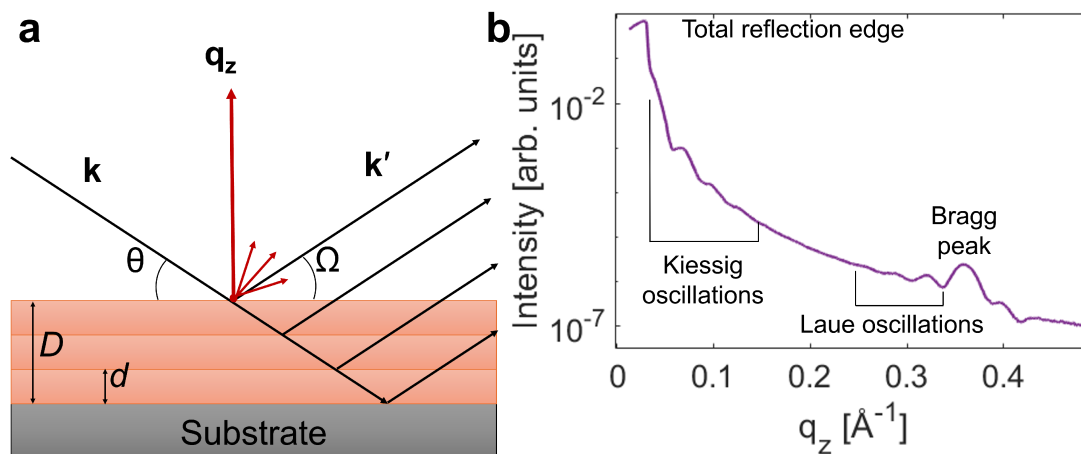


***Figure 4.4:*** *Schematic representation of XRR geometry, illustrating the molecular planes within a thin film (a). The characteristic spacing is denoted by $d$ and total film thickness by $D$. The angle between the incident and reflected beams remains fixed, resulting in the momentum transfer $q_z$ being perpendicular to the substrate. The small red arrows indicate the off-specular contributions to the reflectivity. Example of a XRR data for a DIP film grown on Si/SiO$_x$ at RT (b).*

The reflectivity curve, obtained from an XRR experiment, can yield a series of oscillations known as Kiessig fringes (Fig. 4.4), which, in case of a single-layer film, result from the interference of X-rays reflected at the top and bottom interfaces of the thin film. The periodicity of these fringes provides insight into the film thickness and surface roughness [153, 154].

From the periodicity of the Kiessig fringes, the thickness $D$ of the thin film can be extracted using:

$$D = \frac{2\pi}{\Delta q_z}, \tag{4.1}$$

where $\Delta q_z$ is the spacing between consecutive fringes in $q_z$-space. In crystalline thin films, Bragg reflections occur at angles where constructive interference from X-rays scattered by the crystal planes is observed. This phenomenon is described by Bragg's law, that was previously described in Sec. 2.3.4. Laue oscillations, visible around the Bragg peaks, provide information on the coherence length or the size of crystalline domains normal to the substrate. The presence of both Kiessig and Laue oscillations indicates a well-ordered crystalline film over its entire thickness [102]. To extract precise structural parameters, the experimental reflectivity curve is fitted using models based on the Parratt recursion formalism, which calculates the reflectivity for a stratified medium [151].

## 4.5 Grazing Incidence Small Angle X-ray Scattering (GISAXS)

This and the following section are based on Refs. [44, 155–157], and all other references are explicitly cited.

Grazing Incidence Small Angle X-ray Scattering (GISAXS) is a specialized form of Small Angle X-ray Scattering (SAXS), performed in a grazing incidence geometry [158–160]. In contrast to SAXS, which employs a transmission geometry, GISAXS involves the X-ray beam that impinges on the surface of the sample at a shallow incident angle $\alpha_i$ (typically less than 1°). The scattered intensity is collected at small exit angles $\alpha_f$ and out-of-plane angles $\psi$ by the detector located several meters afar from the sample. A typical geometry for the GISAXS experiments is depicted in Fig. 4.5.

A common coordinate system for GISAXS has the $x$-axis along the X-ray beam direction, the $y$-axis parallel to the sample surface and the $z$-axis along the surface normal. Specular scattering, which fulfills $\alpha_i = \alpha_f$, occurs in the absence of lateral structures. In contrast, lateral deviations in the refractive index produce diffuse scattering, which carries information about the sample morphology.

The components of the scattering vector $\mathbf{q}$ are:

$$q_x = \frac{2\pi}{\lambda}(\cos\psi\cos\alpha_f - \cos\alpha_i), \tag{4.2}$$

$$q_y = \frac{2\pi}{\lambda}\sin\psi\cos\alpha_f, \tag{4.3}$$

$$q_z = \frac{2\pi}{\lambda}(\sin\alpha_i + \sin\alpha_f). \tag{4.4}$$

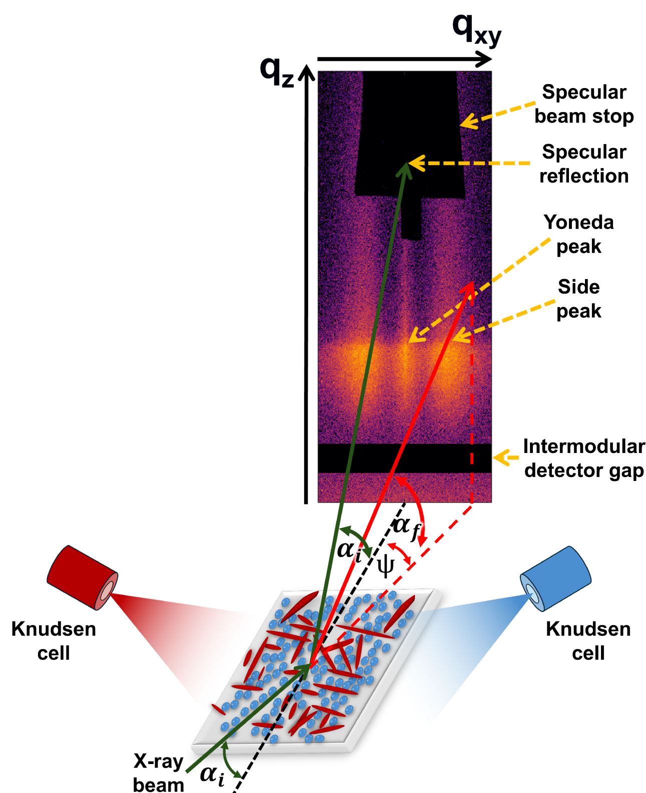


***Figure 4.5:*** *Schematic representation of a GISAXS experiment. Image adapted from [116].*

GISAXS takes advantage of the critical angle $\alpha_c$, at which total external reflection occurs. When the exit angle corresponds to the critical angle, the scattering intensity is significantly increased (this is due to, for instance, waveguide modes). This intense scattering streak is known as the Yoneda peak [161].

The change in $\alpha_i$ in the GISAXS experiment significantly affects the penetration depth of the X-ray beam and thus the sensitivity to different layers within the sample. For $\alpha_i < \alpha_c$, the penetration is limited to a few nanometers, providing high surface sensitivity. For $\alpha_i > \alpha_c$, the beam penetrates deeper, averaging over the thickness of the entire film. This tunability is advantageous in applications such as OPV, where detailed morphological characterization is essential.

GISAXS data analysis often involves Distorted Wave Born Approximation (DWBA), a first-order perturbation theory, which includes dynamic effects on the intensity distribution in the region of total external reflection [162, 163]. Software packages like FitGISAXS [164] or BornAgain [165, 166] allow modeling the full 2D GISAXS intensity distribution, despite some limitations due to the specific options available in each package.

## 4.6 Grazing Incidence Wide Angle X-ray Scattering (GIWAXS)

Grazing-incidence wide-angle X-ray scattering (GIWAXS) is a versatile tool that simultaneously provides information about both in-plane and out-of-plane structure of the sample. Experimentally, the main difference between GISAXS and GIWAXS setup lies in the sample-detector distance - typically, the distance is considerably reduced in the GIWAXS setup, compared to the GISAXS configuration. By positioning the 2D detector closer to the sample, a broader angular range can be probed with the same detector size. Consequently, each pixel of the detector captures data from a wider angular sector, which enhances signal detection. The GISAXS signal still appears faintly in the center of reciprocal space, unless blocked by a beamstop.

In both GISAXS and GIWAXS, the incident angle can be varied, allowing the extraction of different types of structural information:

- $\alpha_i < \alpha_c$(active layer) provides details about the crystalline arrangement near the surface of the active layer
- $\alpha_c$(active layer) $< \alpha_i < \alpha_c$(substrate) gives insights into the crystal structure throughout the full active layer
- $\alpha_c$(substrate) $< \alpha_i$ provides structural data almost exclusively about the substrate.

The analysis of GIWAXS data provides insight into the crystalline structure of the materials under investigation. The four scenarios that appear most frequently in the GIWAXS patterns are depicted in Fig. 4.6:

- a) For highly crystalline films with crystals oriented parallel to the substrate surface, well-pronounced Bragg peaks appear.
- b) If the film contains both parallel and perpendicular orientations of crystallites, Bragg peaks appear in both vertical and horizontal directions.
- c) A more textured film with domains oriented around the horizontal alignment results in broadened Bragg peaks in the azimuthal direction.
- d) Powder-like films with a high degree of orientational disorder produce Debye-Scherrer-like rings.

In grazing incidence, geometry can introduce image distortions that must be corrected prior to analysis. One issue is that the 2D detector misses part of the reciprocal space in the vertical direction. Missing information can be obtained through additional measurements or by using geometries that satisfy the specular condition, such as tilting the sample to match the Bragg angle of interest.

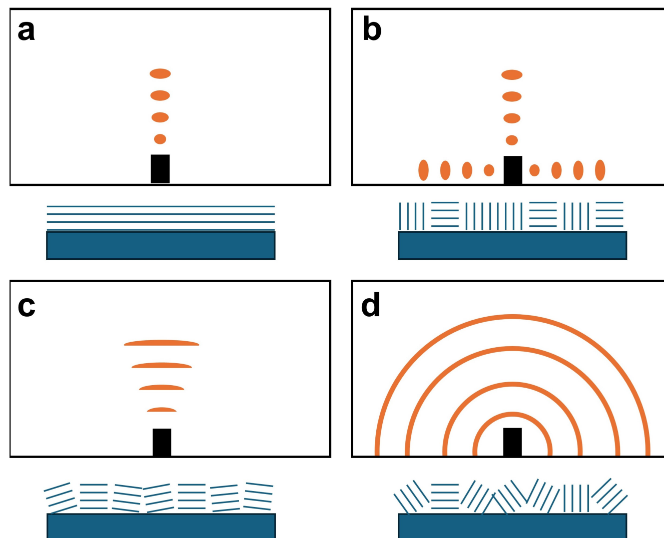


***Figure 4.6:*** *Schematic illustration of film crystallinity and associated 2D GIWAXS patterns for different scenarios: vertical lamellar stacking (a), crystallites with both vertical and horizontal orientations (b), oriented domains (c), and complete rotational disorder of crystallites (d). The black rectangle in the center of each picture represents a beamstop. Image adapted from [155].*

## 4.7 UV-Vis absorption spectroscopy (UV-Vis)

UV-Vis spectroscopy is a non-invasive technique used to analyze the absorption properties of thin films across a wavelength range of 200 to 900 nm. These measurements provide averaged information about the system without the need for an optical model. However, in the transmission mode used in the present work, they offer only semi-quantitative data about the extinction coefficient $k$ of the thin films. A simple transmission geometry with non-polarized light at normal incidence was used, excluding back- and diffuse scattering effects. The measurements were performed at normal incidence, capturing only in-plane absorption. A typical setup includes a monochromator that isolates a narrow spectral band from a white light source. The intensity of the light passing through the sample is measured by a photodetector. The fundamental principle of absorption follows the Beer-Lambert law, where transmittance $T$ is defined as the ratio of the transmitted intensity $I(D)$ to the incident intensity $I_0$ through the material (Fig. 4.7):

$$T(\lambda) = \frac{I(\lambda)}{I_0(\lambda)} = e^{-\alpha(\lambda)D} \tag{4.5}$$

Here, $\alpha$ represents the absorption coefficient, which can be derived for thin films if the film thickness $D$ is known. The in-plane component of the extinction coefficient $k_{xy}$, related to the absorption coefficient and wavelength $\lambda$, can be calculated using the following equation:

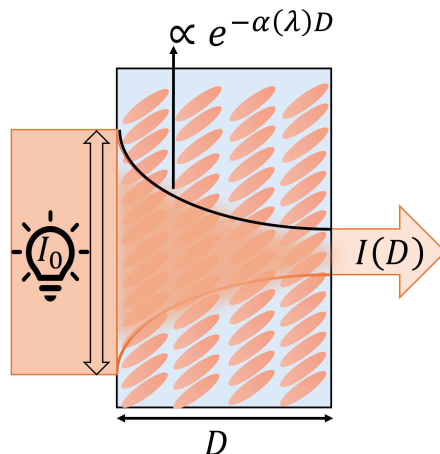


***Figure 4.7:*** *Schema of absorption spectroscopy in transmission mode. The unpolarized beam with initial intensity $I_0$ is aligned parallel to the sample surface. The beam undergoes attenuation within the organic film of thickness $D$, following the Beer-Lambert law (Eq. 4.5). Image adapted from [140].*

$$k = k_{xy} = \frac{\lambda \cdot \alpha(\lambda)}{4\pi} \tag{4.6}$$

Since only the in-plane component of $k$ is measured in this setup, the scattering effects at the glass interfaces are neglected. A measurement of a clean quartz substrate was taken as a reference in advance and subtracted from the spectra.

All absorbance measurements were performed in-house using a Lambda 950 spectrometer by Perkin Elmer, covering a spectral range from 200 to 900 nm. A deuterium lamp was used for wavelengths shorter than 319.2 nm, and a halogen lamp was used for longer wavelengths. A lead sulfide detector was used for wavelengths beyond 820 nm, replacing the photomultiplier tube used for shorter wavelengths.

## 4.8 Photoluminescence spectroscopy (PL)

Photoluminescence (PL) spectroscopy is a sensitive, non-destructive optical technique widely used to investigate the electronic and structural properties of materials. This technique is particularly useful for examining intermolecular interactions within the solid-state arrangement of organic films, providing insights into the charge-transfer (CT) states, which are the lowest-lying excited states [167–169]. Temperature-dependent PL measurements are often conducted at low temperatures to achieve more precise and well-resolved spectral peaks because lower temperatures reduce the number of possible relaxation pathways and thermal broadening effects. This makes it easier to detect CT states in the PL spectra of organic thin films at reduced temperatures [128].

PL setup consists of a continuous-wave laser that excites the sample at a fixed wavelength. A laser beam is directed through a series of optical components and focused onto the sample using an objective lens. After excitation, electrons from the valence band move to the conduction band, creating electron-hole pairs or excitons. These excited states are not stable and tend to relax back to their ground state, emitting photons in the process. The energy (or wavelength) and intensity of the emitted light provide valuable information about the electronic structure of the material. This emission is then collected by a lens directed to a detector. A band stop filter is placed between the lens and the detector to protect the detector from laser radiation. Adjustable gratings (with 150 or 1800 lines per mm) are installed to set the desired resolution of the diffracted light before reaching a charge-coupled device detector. A video camera and interchangeable objectives enable the use of the spectrometer as a microscope for detailed sample inspection. The intensity of the laser can be controlled using density filters, which also help minimize potential damage to the sample.

In this work, PL experiments were conducted using a frequency-doubled Nd:YAG laser with a wavelength of 532 nm. A LabRam HR 800 spectrometer (HORIBA Jobin Yvon) equipped with a nitrogen-cooled 1024 $\times$ 256 pixel CCD detector was used. For temperature-dependent PL measurements, a CryoVac cooling system employing liquid nitrogen or helium was used, covering a temperature range from 293 K down to 80 K or 15 K.

# Part III

# Results

Chapter 5

# Results of pristine dibenzoselenadiazoloquinoxaline thin film growth and annealing kinetics

This chapter contains results on the structural and optical properties of thin films of pristine dbSeQ with different thicknesses that were grown under various conditions. The results included here are partially published in [170, 171].

In recent years, organic semiconductors based on polymers and $\pi$-conjugated small molecules have attracted considerable interest due to their potential applications in electronics and optoelectronics [172–175]. A major advantage of these materials is their tunability through chemical modification, which allows their properties to be tailored by adding or substituting specific functional groups. In particular, 1,2,5-thia- and selenadiazole derivatives, with various substitutions, are widely used as electron-accepting cores in materials for field-effect transistors [176, 177], solar cells [178, 179], and light-emitting diodes [180], due to their electron-deficient, planar heteroaromatic structures. The distinctive molecular arrangement of 1,2,5-selenadiazoles enables these molecules to form supramolecular synthons, where characteristic Se$\cdots$N square motifs arise from the chalcogen bonding [181]. During the past two decades, this type of secondary bonding interaction has attracted increasing attention [182, 183]. The chalcogen bonding comes from the interaction of $\sigma$-holes (positively charged regions) on selenium atoms with the lone pairs of nitrogen atoms acting as Lewis bases [184]. The strength and directionality of this interaction enable the formation of dimers and polymers, which can potentially allow electron transfer between molecules and promote the development of well-ordered structures [182, 183, 185–187]. The molecular ordering is crucial, as it governs charge transport, energy transfer, and optical properties, thereby influencing the overall performance of the devices [188–190]. Furthermore, the self-association of $\pi$-conjugated molecules through efficient $\pi - \pi$ stacking interactions can improve structural organization and ordering at mesoscopic scales [191]. To optimize crystallinity within these materials, a promising design strategy involves extending the conjugated framework by incorporating aromatic systems into the chalcogenadiazole core. This approach not only adjusts the electronic structure but also improves self-association through the expanded $\pi$-surface.

Previously studied $\pi$-conjugated polymers that incorporate a chalcogenadiazole scaffold typically exhibit disordered thin films [192, 193]. Consequently, there has been increased interest in small-molecule derivatives [176, 194–196], as they offer not only improved crystallinity but also several additional advantages, such as low polydispersity, well-defined chemical structures, and reliable synthetic reproducibility [172].

An important consideration regarding the arrangement of molecules within the material is the dependency of electrical and optical properties of thin films and, thus, device efficiency on the molecular orientation relative to the substrate. This effect has been particularly observed for low-symmetry $\pi$-conjugated molecules [197–201].Therefore, a comprehensive understanding and precise control over molecular orientation are critical for unlocking the full potential of these materials in future applications.

In this chapter, we present a detailed structural and optical characterization of $\pi$-extended dibenzo[f,h][1,2,5]selenadiazolo[3,4-b]-quinoxaline (dbSeQ) in thin films, which were fabricated using the OMBD method. Using a combination of *ex situ* GIWAXS, together with AFM and XRR, and *in situ* real-time GISAXS techniques, we analyzed the structure and morphology evolution of dbSeQ films on silicon substrates at various temperatures and growth rates. Optical characterization by UV-Vis and PL was performed to obtain a comprehensive evaluation of the structural, optical, and electronic properties of thin films.

Our results demonstrate that controlling the substrate temperature during film growth significantly influences the molecular orientation, resulting in noticeable changes in the film morphology and optical properties. It was also observed that the thin films grown at LT exhibited low thermal stability, as evidenced by a significant change in morphology during annealing to RT.

## 5.1 Growth conditions and sample preparation

DbSeQ was synthesized and provided by the group of Prof. Zibarev (Novosibirsk Institute of Organic Chemistry) and used as received.

Co-deposited and bilayer thin films of dbSeQ were grown in a portable vacuum chamber under UHV conditions using the OMBD method [38, 41, 56, 202]. We used two types of substrates: silicon wafers (Si(100), p-type) with a native oxide layer for X-ray and AFM characterization and quartz wafers for UV-Vis absorption spectroscopy. Before deposition, we cleaned the substrates in an ultrasonic bath with acetone and isopropanol for 10 minutes each, followed by heating to 480 K inside the vacuum chamber for 12 hours.

During film growth, the substrate temperature was maintained at 303 K (room temperature, RT) or 173 K (low temperature, LT). The deposition rate was monitored using a quartz crystal microbalance (SQM-160, Inficon). The deposition rate was 0.3 nm/min if not specified explicitly.

*In situ* XRR scans and real-time GISAXS measurements were performed at

the beamline ID10-SURF at the ESRF (Grenoble, France) using an X-ray beam focused to 17 × 35 $\mu$m$^2$ (hor. × vert.) with a wavelength of 1.033 Å. GISAXS measurements were conducted at the incidence angle of 0.4° (i.e. above the critical angle of the Si/SiO$_x$ substrate and all organic layers) using a 2D detector (Dectris EIGER X 4M, pixel size 75 × 75 $\mu$m$^2$) placed at the distance of 4000 mm from the sample.

Structural investigations were performed using XRR and GIWAXS techniques. All the *ex situ* XRR scans were measured on a diffractometer (GE XRD-3003TT) using CuK$_{\alpha 1}$ radiation ($\lambda$ = 1.5406 Å). *Ex situ* GIWAXS characterization was performed on a Xeuss 2.0 (Xenocs) in-house instrument using CuK$_\alpha$ radiation $\lambda$ = 1.542 Å at an incidence angle of 0.2°, employing a PILATUS 300 K detector (Dectris).

The surface morphology of the thin films was characterized *ex situ* using AFM in tapping mode, which was performed using a NanoWizard II microscope (JPK Instruments). Additional *ex situ* morphology characterization was performed using SEM, where a Philips XL30 SEM system was used, operating with an electron beam accelerated by a high voltage of 20 kV. The AFM data was analyzed using the Gwyddion software package [142]. Data evaluation for AFM starts with image processing, including scar healing and removing the defects. The next step is to mark the grains with one of the program built-in tools that uses a watershed algorithm to detect grains [203]. After marking the grains, we can extract surface coverage, average grain sizes (length and width of the grain), grain roundness (width/length ratio), and correlation length (that corresponds to the inter-island distance in this case). The following step involves the extraction of the height-height correlation function (HHFC), which is a useful instrument to characterize growth-induced surface roughness [56, 204]. It is defined as the mean square height difference:

$$g(R) = \langle [h(x, y) - h(x', y')]^2 \rangle$$

for pairs of points laterally separated by $R = \sqrt{(x - x')^2 + (y - y')^2}$. The HHCF can be computed from real-space images by averaging over one or more regions that are significantly larger than $R$, in order to minimize edge effects [79]. HHCFs were fitted by function

$$f(x) = 2\sigma^2[1 - \exp(-(x/\xi)^2)]$$

where $\sigma$ is the root-mean-squared (RMS) roughness and $\xi$ is the lateral correlation length. For a better understanding of what is $\xi$, it is important to mention that during the growth process we observe the emergence of correlations across the surface, which means that the sites are not fully independent, but are affected by the heights of neighboring sites. The typical distance over which the heights "feel" each other, or, in other words, the characteristic distance over which they are correlated, is referred to as the *correlation length*, usually denoted by $\xi$ [205]. Essentially, it describes the distance over which the surface height of the thin film

is statistically similar to another point on the surface. More details about the fit procedure can be found in Sec. 9.1 in the Appendices.

*Ex situ* UV-Vis absorption spectra were measured in transmission mode using a PerkinElmer Lambda 950 UV-Vis-NIR spectrometer. PL spectra were acquired with a Labram HR 800 spectrometer (Horiba Jobin Yvon, France) equipped with a 1024 × 256 pixel CCD detector and an excitation source from a frequency-doubled Nd:YAG laser operating at a wavelength of 532 nm. Temperature-dependent PL measurements were performed using a CryoVac system cooled with liquid nitrogen, allowing data acquisition in a temperature range of 80 to 290 K.

XRR data were fitted using the custom-developed program based on the `refnx` data analysis package [206] and the `reflectorch (mlreflect 2.0)` data analysis package that utilizes the machine learning approach [207–209]. GIWAXS data were processed using `pygid` Python data analysis package for fast GIWAXS data reduction [210].

## 5.2 Morphology evolution during growth

GISAXS proved to be a powerful instrument for investigating the evolution of the morphology in thin films. In the context of this work, GISAXS is the main method to characterize dbSeQ films, due to its versatility, applicability to rough surfaces [211] and its ability to explore the growth of thin films *in situ* in real-time with high temporal and spatial resolution [45, 158, 212]. Before the description of the experimental data, a data evaluation procedure should be discussed in detail. The typical real-time GISAXS experiment produces a large sequence of 2D intensity patterns, one example of the typical image depicted in Fig. 5.1 (a). In addition to useful information, a standard GISAXS image contains various artifacts, including regions with zero intensity, manifested as horizontal and vertical lines. These lines correspond to the intermodular detector gaps, i.e. the spaces between the detection modules within the detector. Another area of the image that exhibits zero intensity is located in the upper central part of the image. This area corresponds to the specular beam stop that serves to protect the detector from the radiation damage caused by high-intensity illumination occurring in this area, which could be several orders of magnitude higher than the scattered intensity in the rest of the pattern. The beam stop seen in the lower central part of the detector image in Fig. 5.1 (a) serves for the same purpose at the position of the direct beam.

The whole detector image contains a lot of irrelevant information; therefore, for the analysis, we picked a smaller region (pink rectangle) that contains the vertical intensity streak with an intensity maximum in the lower part of it. This maximum is called the Yoneda peak, and its position is defined by the critical angle of the scattering material; therefore, it is a characteristic feature of the deposited material [161, 213]. To create a $q$-map, we convert the pixels of the detector image into the corresponding $q$ values in reciprocal space, and the example of the resulting image is depicted in Fig. 5.1 (b). Rather than processing the entire

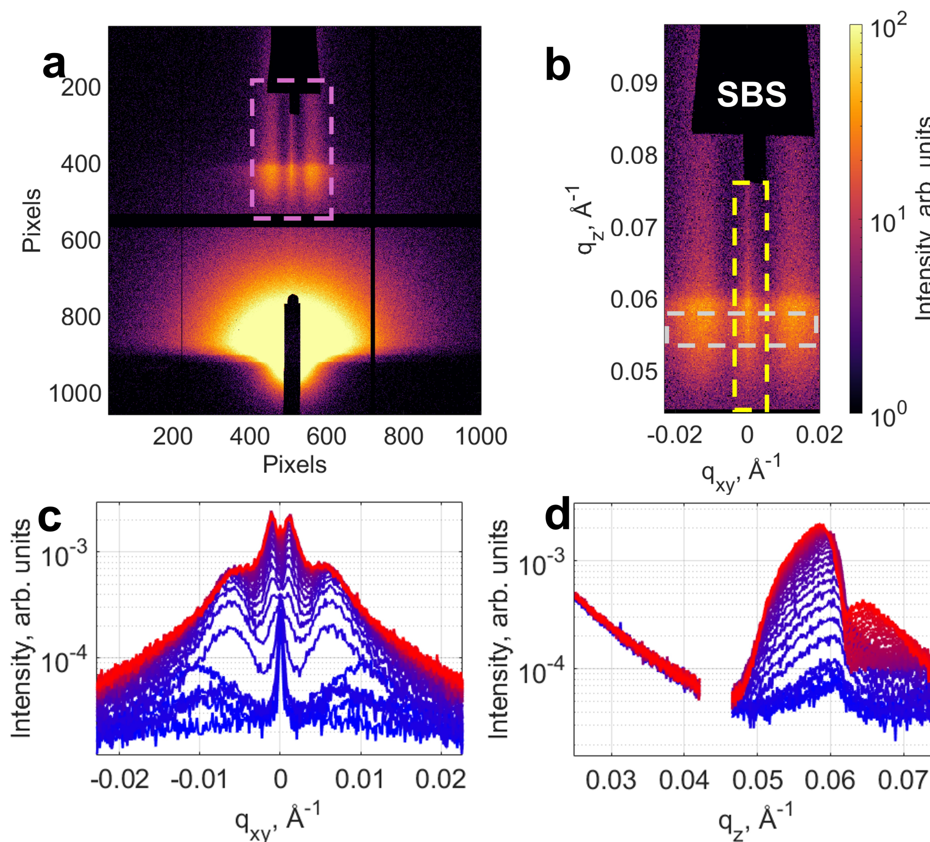


*Figure 5.1: An example of GISAXS data evaluation procedure. A typical detector image with 2D GISAXS pattern (a). Pink dashed rectangle shows the region of interest (ROI) that contains all information about the investigated structure. The ROI transferred to the q-space (b). The horizontal gray and vertical yellow dashed rectangles demonstrate the region for the vertical and horizontal cuts [150, 158, 162]. SBS stands for specular beam stop. Horizontal (c) and vertical (d) line cuts extracted from the experimental data.*

two-dimensional intensity distribution (which could take a lot of computational resources and subsequently a lot of time), the scattering data analysis can be simplified by focusing on specific sections, or "cuts" [158, 214]. Two types of cuts are particularly useful: horizontal slices at constant $q_z$ and vertical slices at constant $q_{xy}$, where horizontal and vertical refer to the sample surface [215]. The horizontal cut depends only on the wave vector component $q_{xy}$, so only parallel to the surface structures of the sample are investigated. In contrast, the vertical cut depends on $q_z$ so the only perpendicular to the surface structures are probed [158]. Both line cuts are usually integrated over several lines of detector pixels to enhance statistical accuracy [216]. In the following section they were integrated over 20 pixels (marked as gray and yellow dashed rectangles in Fig. 5.1 (b)). The resulting plots of both line cuts plotted versus the scattering intensity are presented in Fig. 5.1 (c) and (d).

Data analyzing procedure contains three main parts: we extract data from HDF5 files, convert it to the reciprocal space map, then make line cuts to obtain 2D plots of intensity versus $q_z$ and $q_{xy}$. Then we plot waterfall plots to see the changes over the deposition process in detail and the last step is to fit the data with Lorentzian, Gaussian, or Voigt functions (see Sec. 9.3 in the Appendices for more details). The fit provides useful information on the evolution of the peak intensity, width, and position that can later be interpreted with physical concepts. The peak intensity is related to the roughness and the amount of deposited material in the volume illuminated by X-rays [43]. The width of the side peak is associated with the distribution of correlation distances when the form factor contributions are neglected, meaning that the narrower the peak, the narrower the size distribution of the islands [45, 217, 218]. The peak position of the side maximum corresponds to the correlation length [43]. It is important to note that the side peaks are located symmetrically about the $q_z$-axis; therefore, for a complete description of the morphology evolution, it is sufficient to use data from one peak.

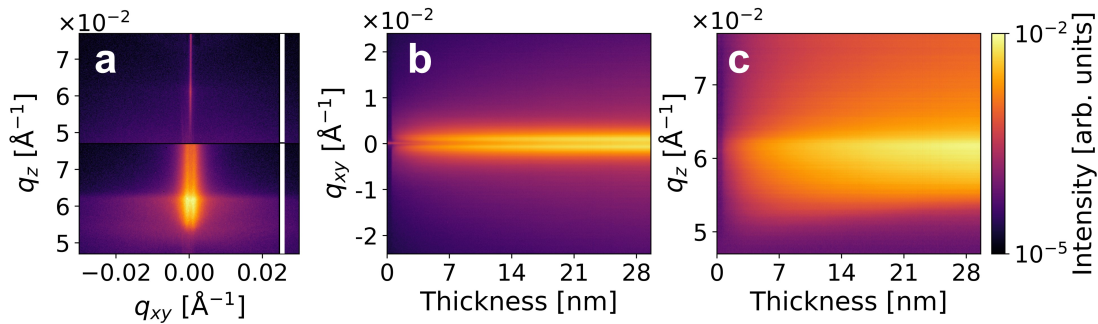


***Figure 5.2:*** *In situ GISAXS data for the growth of neat dbSeQ thin film ($d_{nom}$ = 30 nm) on Si/SiO$_x$ at RT. 2D GISAXS patterns measured at the beginning (top part) and end (bottom part) of the deposition (a), and evolution of the intensity in the horizontal cut of the GISAXS pattern (integrated in the range of $q_z = 0.056 - 0.060$ Å$^{-1}$) (b) and vertical cut (integrated in the range of $q_{xy}$ = -0.001 – 0.001 Å$^{-1}$) (c) during the deposition as a function of the thickness. The white vertical lines are presenting intermodular gaps of the detector.*

A starting point in our investigations is the deposition of neat dbSeQ at RT, and Fig. 5.2 (a) shows GISAXS patterns taken at the beginning and at the end of the deposition. At the initial deposition stage, the prominent central streak at $q_{xy} = 0$ originating from the Si/SiO$_x$ substrate is observable. As deposition continues, two symmetrically located side peaks emerge, suggesting the formation of laterally correlated structures on the substrate [218]. The position of the side peaks corresponds to the correlation length $D_{\text{corr}} \approx 2\pi/q_{xy}$, where $q_{xy}$ is the fitted peak position [43]. $D_{\text{corr}}$ can be interpreted as a characteristic length scale of the features on the substrate and is affected by the island shape (e.g. form factor) and the inter-island distance (e.g. structure factor). Subsequently, these side peaks obscure the central peak, due to the increased roughness of the film [116].

Those peaks appear first at the very beginning of the deposition and remain distinguishable until the end of the experiment. As the nominal thickness increases, the intensity of the side peaks also increases because of more scatterers in the illuminated volume. Notably, we do not observe any new features along the $q_{xy}$ and $q_z$ axes during the growth, indicating the absence of additional correlation lengths in horizontal and vertical directions.

Quantitative information is extracted by making line cuts along $q_{xy}$ (horizontal line cut) at the Yoneda peak position of dbSeQ ($\alpha_c(dbSeQ) + \alpha_i$, corresponding to $q_{z,c}(dbSeQ) = 0.558$ Å$^{-1}$ in the current experiment). In addition, vertical line cuts are made along $q_z$ at $q_{xy} = 0$. Fig. 5.2 (b) and (c) present waterfall plots of the horizontal and vertical line cuts, respectively, plotted versus the nominal thickness of the deposited film. As demonstrated in Fig. 5.2 (b), the RT growth exhibits two symmetrically positioned peaks with respect to $q_{xy} = 0$ as the nominal thickness approaches 1 nm and at this point $D_{\mathrm{corr}}$ equals $617 \pm 15$ nm. As the growth continues, we observe the increase in intensity of side peaks that arises from the increase in the amount of dbSeQ at the substrate surface. The correlation length slightly increases and decreases throughout the deposition, and as nominal thickness of the film equals 10 nm the correlation length $D_{\mathrm{corr}} = 807 \pm 4$ nm and by the end of the deposition $D_{\mathrm{corr}} = 795 \pm 5$ nm. As illustrated in Fig. 5.2 (c), the waterfall plot of the vertical line cuts reveals a pronounced Yoneda peak that becomes more intense during the deposition process. This is attributed to an increase in the amount of material illuminated by the X-ray beam. For neat dbSeQ films grown at RT, the XRR analysis (typical XRR curves for various RT-grown dbSeQ films are presented in Fig. 9.4 in Appendices) does not show any features because of very high surface roughness of the film. The growth of dbSeQ film at RT is characterized by weak molecule-substrate interaction and stronger molecule-molecule interaction where the strong interaction between molecules dominates at every growth stage [56]. We conclude that for the RT growth of neat dbSeQ, pronounced island growth is observed from the beginning of the deposition and the growth mode remains unchanged.

A comparison of the growth of neat dbSeQ at LT with its growth at RT reveals several differences. As demonstrated in Fig. 5.3 (a), for the LT growth of dbSeQ, a prominent central peak at $q_{xy} = 0$ that arises from the $Si/SiO_x$ substrate is observable. Throughout the entire deposition process, the central peak remains uncovered by the side peaks. A well-defined central streak usually corresponds to a smooth surface, while a broader streak may indicate increased roughness or irregularities on the surface. This indicates a low film roughness, a finding that is confirmed by the XRR measurements presented in the next section. Figs. 5.3 (b) and 5.3 (c) present waterfall plots of the horizontal and vertical line cuts, respectively, plotted versus the nominal thickness of the deposited film. As illustrated in Fig. 5.3 (b), it is possible to differentiate between two distinct phases of growth, namely 0 - 10 and 10 - 30 nm. In the initial phase, the side peaks appear at relatively large $q_{xy}$ values.

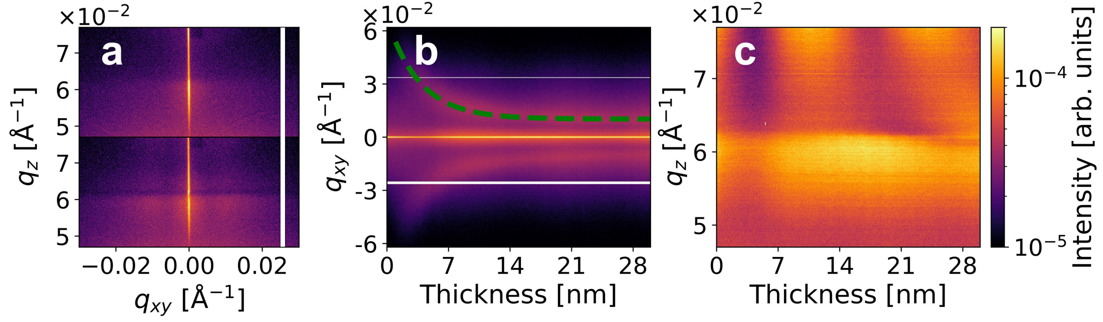


***Figure 5.3:*** *In situ GISAXS data for the growth of neat dbSeQ thin film ($d_{nom}$ = 30 nm) on Si/SiO$_x$ at LT. 2D GISAXS patterns measured at the beginning (top part) and end (bottom part) of the deposition (a), and evolution of the intensity in the horizontal cut of the GISAXS pattern (integrated in the range of $q_z = 0.056 - 0.060$ Å$^{-1}$) (b) and vertical cut (integrated in the range of $q_{xy}$ = -$0.001 - 0.001$ Å$^{-1}$) (c) during the deposition as a function of the thickness. The green dashed line in panel (b) shows the fit result of the side peak position. The white vertical and horizontal lines are presenting intermodular gaps of the detector.*

During deposition, these peaks undergo a rapid shift toward lower $q_{xy}$ values. As the nominal film thickness reaches 10 nm, the peak position becomes almost unchanged with minimal fluctuations. The shift in the side peak position can be described by an exponential function $q_{xy}(d) = q_0 + A\exp\left(-\frac{d}{d_0}\right)$, where $q_0 = 0.010$ Å$^{-1}$, $A = 0.057$ Å$^{-1}$, and $d_0 = 2.67$ nm (dashed line in Fig. 5.3 (b)). The fit is presented in Fig. 5.4. The corresponding correlation length $D_{corr}$ at the beginning of the deposition ($d_{nom}$ = 1.7 nm) equals $20 \pm 1$ nm, and at the end ($d_{nom}$ = 30 nm) it is $63.0 \pm 0.8$ nm. The extrapolated to $d_{nom} = 0$ nm value of $D_{corr}$ equals 9.4 nm. The vertical line cut waterfall plot presented in Fig. 5.3 (c) shows the intensity modulations throughout the entire deposition. They shift towards lower $q_z$ values, as the thickness increases, indicating the continuous vertical growth of a smooth film [43, 218].

We assume that the growth of neat dbSeQ at LT is characterized by flat islands and proceeds as follows. At the onset of the initial phase, a high number of islands emerge on the substrate surface. The intensity observable at the very beginning of the initial stage ($d_{nom}$ < 1.5 nm) for vertical line cut in Fig. 5.3 (c) arises from the Si/SiO$_x$ substrate and the intensity modulations indicating continuous layer growth. Then, the islands coalesce to form larger islands, as evidenced by the increase in the correlation length. In the second phase, the increase in correlation length is negligible, indicating that the film grows predominantly vertically. These observations are also confirmed by the post-growth XRR presented in the next section. The evolution of the film morphology during the annealing to RT is also presented in the next section.

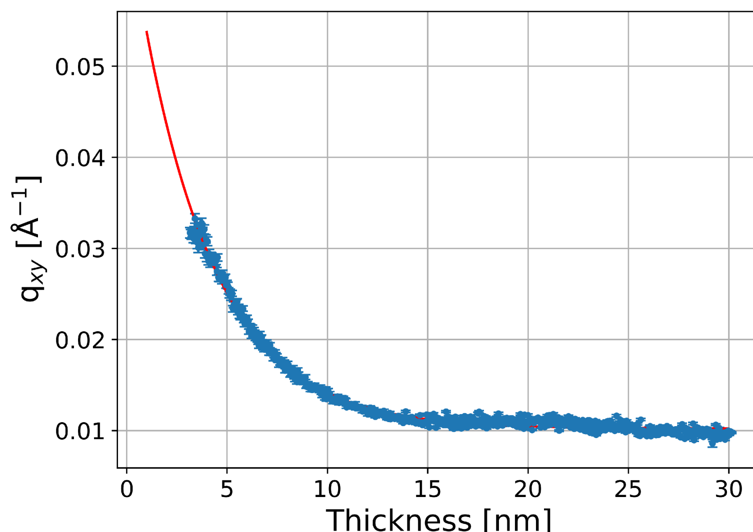


***Figure 5.4:*** *Fit (red curve) of the peak position curve (blue dots) with an exponential function, plotted versus film thickness for the LT-grown dbSeQ film.*

## 5.3 Morphology evolution during annealing

To investigate the evolution of the morphology of thin films grown at RT during their annealing to 333 K, *in situ* XRR and GISAXS measurements were performed. The post-growth annealing of the thin film was performed in three steps, by subsequent heating of the substrate to 313, 323 and 333 K, respectively.

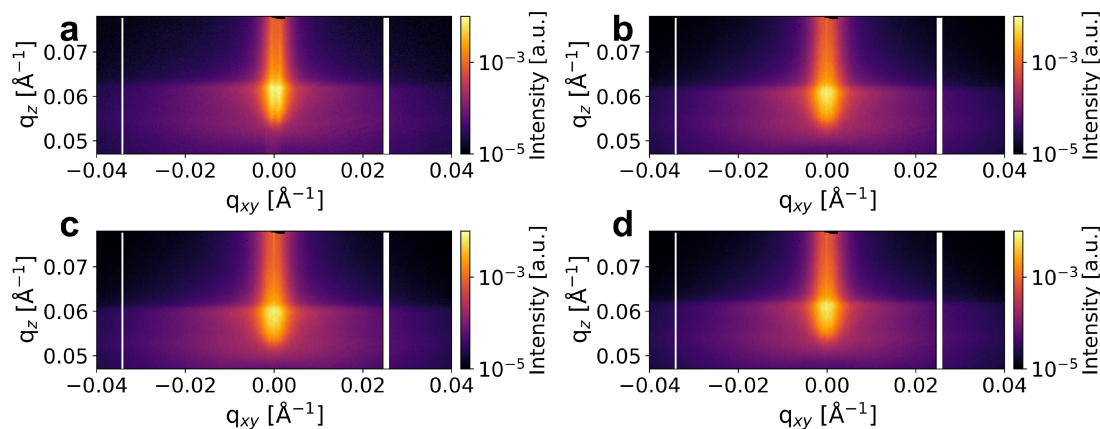


***Figure 5.5:*** *Averaged GISAXS images for every annealing step for the RT-grown neat dbSeQ film: 303 K (a), 313 K (b), 323 K (c), 333 K (d). The white vertical lines are presenting intermodular gaps of the detector.*

The post-growth *in situ* XRR scan is presented in Fig. 9.4 (f) in the Appendices, and reveals the absence of scattering features making further XRR analysis not feasible. The absence of distinct characteristic features is attributed to the high

surface roughness. These observations are consistent with the results of the *ex situ* analysis presented in the next section.

The selected GISAXS patterns taken during the annealing are presented in Fig. 5.5. At the post-growth scan in Fig. 5.5 (a) we can distinguish two side peaks located very close to each other, and the correlation length $D_{\text{corr}} = 801 \pm 7$ nm.

At T = 313 K (Fig. 5.5 (b)) we observe that the pronounced central streak appeared at $q_{xy} = 0$, but the side peaks overlap and become indistinguishable. For the next annealing steps depicted in Fig. 5.5 (c, d), we observe minor changes in the GISAXS patterns compared to T = 313 K. These findings indicate that the correlation length during annealing increases and exceeds the experimental resolution. We assume that the increase in the correlation length is caused by the desorption of dbSeQ islands from the substrate surface.

To investigate the evolution of the morphology of thin films grown at LT during their annealing to RT, *in situ* XRR and GISAXS measurements were performed. *In situ* XRR measurements conducted after deposition and during subsequent annealing provided important information on the thin films of dbSeQ. Post-growth annealing was performed in three steps from 173 to 313 K, and the selected XRR patterns for the annealing steps are presented in Fig. 5.6.

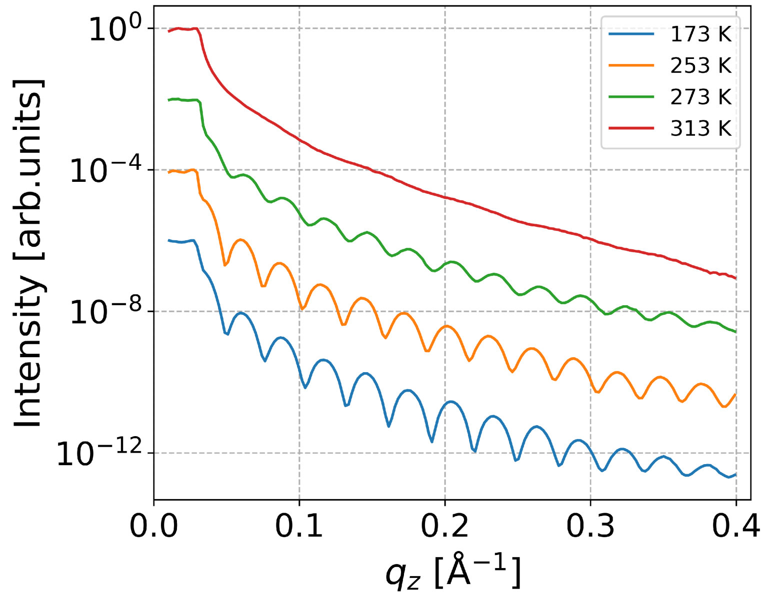


***Figure 5.6:*** *XRR measurements of neat dbSeQ on Si/SiO$_x$ grown at LT post growth and during the annealing to RT. All curves are vertically offset for clarity. For fitting and data analysis see Fig. 5.7.*

In Fig. 5.6 we observe a post-growth XRR scan of a neat dbSeQ film with a nominal thickness $d_{\text{nom}} = 30$ nm deposited at LT (blue curve) along with subsequent annealing steps up to 313 K. The pronounced Kiessig fringes are visible at each annealing stage up to 273 K. Above 273 K, the XRR results resembled those

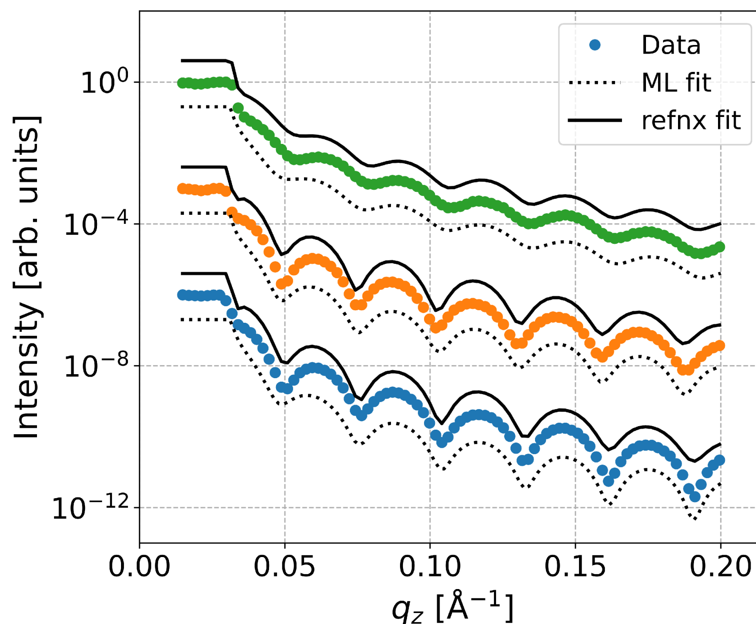


***Figure 5.7:*** *Fits of the XRR data for post-growth and subsequent annealing steps (253 and 273 K) for LT-grown neat dbSeQ film, utilizing* **`refnx`** *[206] and* **`reflectorch (mlreflect 2.0)`** *[207–209] packages. All curves are vertically offset for clarity.*

previously observed in RT-grown films. This indicates that, initially, the LT-grown film is relatively smooth and remains smooth as the temperature increases, until it reaches 273 K. In the temperature region between 273 and 313 K, the film exhibits strong roughening, which leads to the absence of fringes in the XRR pattern. Fitting the data using two approaches, as shown in Fig. 5.7, reveals the low roughness for the dbSeQ film ($\sigma = 0.41 \pm 0.03$ nm) which persists up to 273 K. Strong roughening is attributed to the strong dewetting of the thin film as a result of an increased thermal energy. The AFM studies presented in the next section confirm that the films of dbSeQ grown at LT and annealed to RT, have high roughness and high jaggedness due to dewetting. This indicates that the film has limited thermal stability.

Unlike annealing of the RT-grown film, for the LT-grown dbSeQ film, we observe the changes in the GISAXS patterns for every annealing step. Additional GISAXS data was obtained during each annealing step and the results are presented in Fig. 5.8. The discernible side peaks along the intense central streak at $q_{xy} = 0$ are observable in the post-growth scan in Fig. 5.8 (a). At T = 253 K (Fig. 5.8 (b)) we observe the shift of the side peaks towards $q_{xy} = 0$, which means an increase in the correlation length and the widening of the central streak. At T = 273 K and at T = 313 K (Figs. 5.8 (c) and (d), respectively) we observe an increase in the distance between the side peaks, indicating a decrease in the correlation length. Fig. 5.9 shows the horizontal line cuts taken from the averaged images and

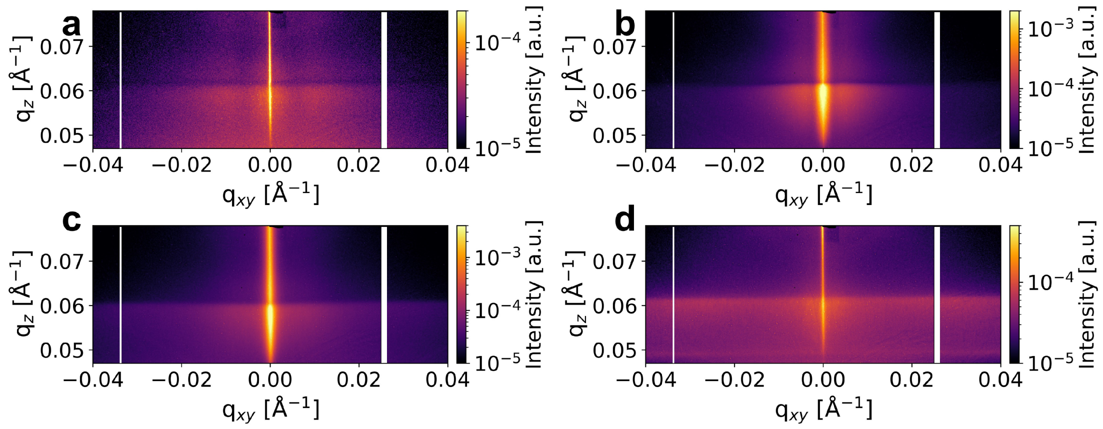


***Figure 5.8:*** *Averaged GISAXS images for every annealing step for the LT-grown neat dbSeQ film: 173 K (a), 253 K (b), 273 K (c), 313 K (d). The white vertical lines are presenting intermodular gaps of the detector.*

confirms that the correlation length for the neat LT-grown film changes with each annealing step, from where after the growth $D_{\mathrm{corr}} = 62 \pm 3$ nm at T = 173 K, to $D_{\mathrm{corr}} = 182 \pm 5$ nm at T = 313 K.

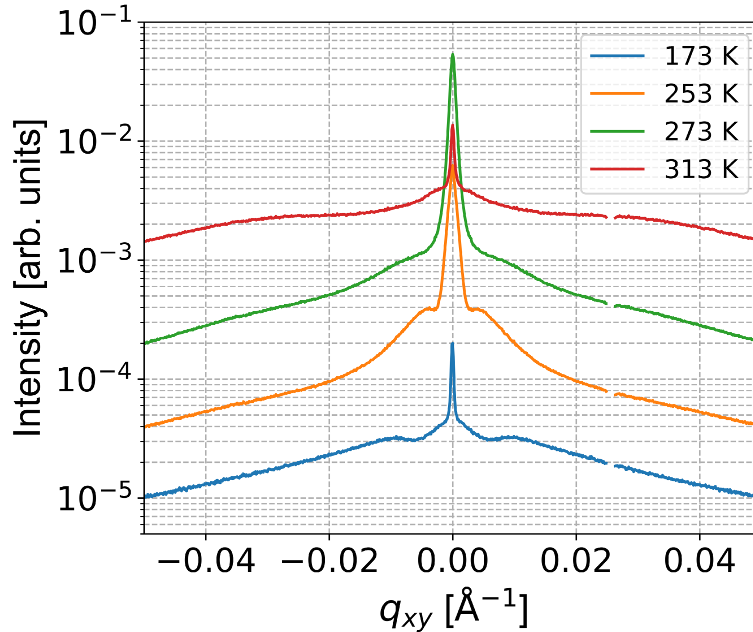


***Figure 5.9:*** *Horizontal line cuts taken from the averaged image from the post-growth and annealing scans for neat dbSeQ film grown at LT. Gaps at about $q_{xy} = 0.023$ Å$^{-1}$ originate from the intermodular detector gap. All curves are vertically offset for clarity.*

In summary, we found that the *in situ* XRR analysis for dbSeQ thin films grown

at RT is not possible because of the high roughness of the film. We found that the *ex situ* and *in situ* XRR scans show almost the same results, which means that the roughening of the RT-grown film is not a post-growth effect that appears during the exposure of the film to the atmosphere. The GISAXS scans that were made during the annealing revealed that the RT-grown film is characterized by large correlation lengths that exceed the resolution of the experiment. We speculate that the correlation length increases with each annealing step as a result of the desorption of the film from the substrate surface. The growth of dbSeQ at LT is characterized by the formation of the film with extremely low roughness. We found that the film remains smooth after growth and subsequent annealing to T = 273 K. In the interval from 273 to 293 K, film roughness increases drastically. We attribute this finding to a strong dewetting that occurs after temperature reaches 273 K. GISAXS data showed that the changes in the correlation length were present during each annealing step, meaning that the LT-grown dbSeQ film exhibits changes in morphology due to annealing. The resulting morphology after exposure of the film to RT is presented in the next section.

## 5.4 Ex situ morphology studies

The surface morphology plays an important role in the characterization of the thin films, as the shape, orientation, and arrangement of the deposited molecules, as well as the roughness, mosaicity, and porosity of the thin film formed from the deposited atoms or molecules, significantly affect various device characteristics. For instance, the surface morphology influences the luminescence [219–221] and plays a crucial role in determining the thermal and electrical conductivity of devices [222–226]. Furthermore, it is critical for the photovoltaic properties of solar cells [227].

Typically, for industrial purposes, the goal is to create smooth films, as rough interfaces often result in poor contact properties [205]. To mitigate roughness, it is essential to understand the mechanisms that cause it and the processes that influence the overall morphology. This knowledge can then be applied to develop films under conditions in which roughening is minimized or eliminated.

Depending on the amount of deposited material, the growth mode in the thin film can change [115, 134, 228] as well as various characteristics of the thin film, such as grain size or roughness [56, 229, 230]. By adjusting growth parameters, such as growth rate or substrate temperature, one can influence the resulting morphology of the thin film [199, 231, 232], therefore we prepared series of thin films of various thickness grown on weakly-interacting Si/SiO$_x$ substrates at different growth conditions. Oxidized silicon wafers are the most widely used substrates for thin film growth due to their smoothness, ease of cleaning, and stability in air [56].

To observe the morphology evolution in the thin film *ex situ*, we grew a set of thin films of various thicknesses, at 303 K (RT) at the same growth rate of 0.3 nm/min. To study the influence of substrate temperatures on the film morphology, we grew a set of films at different substrate temperatures, namely $T_{sub} = 173, 303, 318$

and 328 K. Furthermore, thin films at LT were grown with various thicknesses, $d_{\text{nom}} = 5, 10, 30$ and 50 nm, respectively. To obtain insights on the impact of the rate on the resulting thin film, we grew films with the same nominal thickness of 10 and 20 nm at the different growth rates, i.e. 0.13, 0.3 and 0.52 nm/min. Additionally, we grew a thick film ($d_{\text{nom}} = 50$ nm) with an extra-high rate of 1 nm/min.

The AFM technique was implemented to obtain surface images from which we quantified the changes in roughness, boundary length, island size, and correlation length. Producing AFM images of thin films of dbSeQ is a difficult, time-consuming process, because of the high roughness of the film, needle-like shape of the dbSeQ islands and their interaction with the cantilever. To confirm the AFM morphology data we employed additional SEM characterization, depicted in Fig. 9.3 in the Appendices.

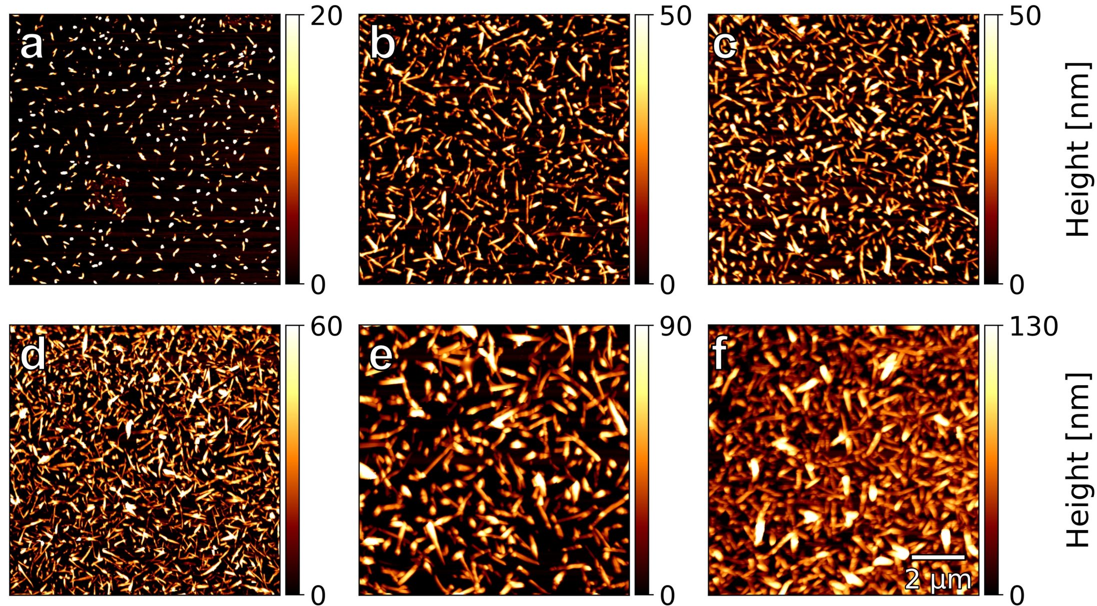


***Figure 5.10:*** *AFM images of dbSeQ thin films of various thicknesses grown on Si/SiOx with a same deposition rate of 0.3 nm/min at RT. Film thicknesses are: 2 nm (a), 8 nm (b), 11 nm (c), 14 nm (d), 18 nm (e), and 36 nm (f).*

Similarly to the Sec. 5.2, we start with a deposition of neat dbSeQ at RT. In Fig. 5.10 the representative AFM topography images of RT-deposited dbSeQ thin films of different thicknesses are shown. The data extracted from these images are shown in Fig. 5.11. At $d = 2$ nm (Fig. 5.10 (a)) we observe the formation of relatively large needle-like structures, randomly oriented on the substrate. The extracted numerical data reveal the average island length $250 \pm 71$ nm, the average width $87 \pm 20$ nm and the roundness of $0.38 \pm 0.18$. The islands of dbSeQ are high, with many islands are higher than 15 nm, thus the surface roughness is high, namely $\sigma_{\text{RMS}} = 7.7 \pm 0.2$ nm and the surface coverage about 6%. For comparison,

the same analysis of AFM images (more details on analysis are presented in Sec. 9.1 in the Appendices) of two thin films of two other materials used in this work, PEN and DIP grown at the same conditions to comparable thickness of 3 nm, reveals that for PEN $\sigma_{\mathrm{RMS}} = 6 \pm 1$ nm and the surface coverage is $\sim 57\%$; for DIP $\sigma_{\mathrm{RMS}} = 0.7 \pm 0.1$ nm, and the surface coverage is $\sim 83\%$. The inter-island distance for dbSeQ is $D_{\mathrm{ii}} = 451 \pm 140$ nm, which is less than the correlation length extracted from the real-time GISAXS data for the comparable film thickness, where $D_{\mathrm{corr}} = 620 \pm 15$ nm. All of these findings indicate the preferred molecule-molecule interaction during the film crystallization.

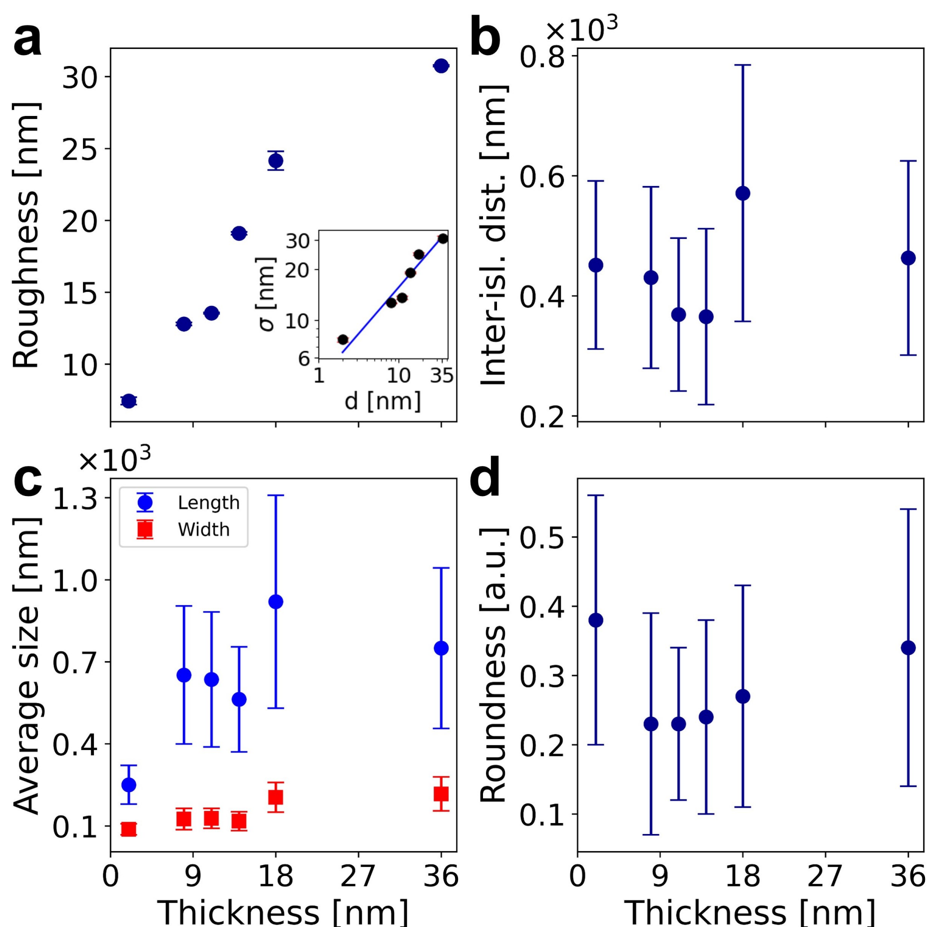


***Figure 5.11:*** *Numerical values extracted from AFM images of the RT-grown films and plotted versus film thickness: rms roughness (a), inter-island distance (b), average island size (c), average roundness (d). The inset in panel (a) shows a log-log scale plot with data fit with a power law $\sigma \sim D^{\beta}$.*

As the film thickness increases, we observe that the length of the islands increases, making them more elongated. We observe that despite the higher amount of deposited material, the substrate is still visible, indicating the relatively low surface coverage. The extracted numerical values for the film with thickness $d =$ 8 nm

(Fig. 5.10 (b)) showing that the average length has drastically increased to the 652±252 nm while the average width 125±39 nm meaning that the island roundness equals $0.23 \pm 0.16$. The roughness increases drastically $\sigma_{RMS} = 12.7 \pm 0.1$ nm and the surface coverage increases to $\sim 32\%$. The inter-island distance remains almost unchanged, where $D_{ii} = 431 \pm 151$ nm.

As more material is deposited (Fig. 5.10 (c) and (d)), rod-like structures grow preferably in the direction perpendicular to the substrate surface, as is evident from the slightly changed average length, width, and roundness presented in Fig. 5.11 (c) and (d), respectively. The extracted surface coverage values show that it is relatively low and equals $\sim 41\%$ and $\sim 43\%$ for films with thicknesses $d = 11$ nm and $d_{nom} = 14$ nm, respectively. The inter-island distances are slightly decreasing for these films, namely to $D_{ii} = 369 \pm 127$ nm and $D_{ii} = 365 \pm 147$ nm, respectively. Similarly to the previous results, the inter-island distances are smaller than the correlation length from the GISAXS data, $D_{corr} \approx 800$ nm. As can be seen from the images, the islands often overlap, which we speculate is the reason for this large difference. We can conclude that the deposited dbSeQ molecules bear to interact with the substrate as little as possible, even at high film thicknesses. One consequence of this phenomenon is that the measured roughness is constantly increasing, up to $\sigma_{RMS} = 19.2 \pm 0.3$ nm for the 14 nm-thick film.

For the last two films with thicknesses $d = 18$ nm and $d = 36$ nm depicted in Fig. 5.10 (e) and (f), respectively, we observe the increase in the island size. The extracted values for the roughness show a constant increase to $\sigma_{RMS} = 31.1 \pm 0.1$ nm for the 36 nm-thick film. The average length for the thickest film is $750 \pm 294$ nm and the average width 217±62 nm. The roundness is slightly increases to 0.34±0.20 and the surface coverage equals almost 70%. The inter-island distance at this point is equal to $D_{ii} = 463 \pm 162$ nm.

From the overall roughness evolution presented in Fig. 5.11 (a) we can conclude that roughness increases almost linearly with thickness. The inset of the figure shows the same plot in log-log scale, where the blue line is the fit of the roughness data with a power law $\sigma \sim D^{\beta}$, where $D$ is the thickness of the film, $\beta$ is the growth exponent. In result, $\beta = 0.55$, which corresponds to the rapid roughening phenomenon, for which $\beta$ should be greater than 0.5 [79]. This means that the roughness increases with thickness, at a rate that exceeds that of the random deposition limit $\beta = 0.5$ [56, 233]. Notably, the roughness plot looks similar to the case of 3D growth scenario, described in detail in the work of E. Empting et al. [234]. The inter-island distance plot depicted in Fig. 5.11 (b) shows that $D_{ii}$ does not change significantly for film with different thicknesses which corresponds to real-time GISAXS data, where the correlation length did not change significantly during the deposition. In general, the inter-island distances extracted from the AFM data are lower than the values of correlation length extracted from the GISAXS data, which can be explained by the overlap of dbSeQ islands. RT-grown films of dbSeQ are crystallizing in elongated islands, where the film with the lowest thickness has the most round islands. We speculate that after film thickness of 2 nm, islands tend to grow more elongated. It can be explained by a preferred one-

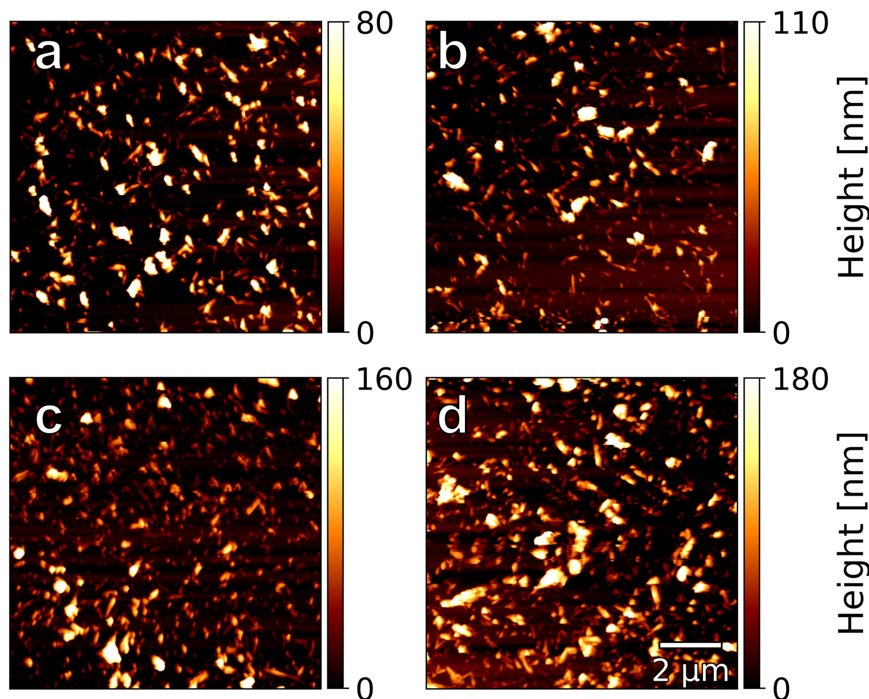


***Figure 5.12:*** *AFM images of dbSeQ thin films of various thicknesses grown on Si/SiO$_x$ with a same deposition rate of 0.3 nm/min at LT. Film thicknesses are: 7 nm (a), 11 nm (b), 17 nm (c), and 28 nm (d).*

dimensional (1D) packing, likely formed by $\pi$-stacks of dbSeQ molecules randomly oriented across the substrate surface. We conclude that dbSeQ does not change the growth mode during its growth at RT, which correlates with the real-time GISAXS data.

A decrease in substrate temperature generally reduces the thermal energy available to the deposited molecules, lowering their kinetic energy and thus minimizing their ability to move and diffuse across the surface. Furthermore, the molecules exhibit different orientation on the substrate surface, a phenomenon observed for dbSeQ (see Sec. 5.5) and other organic semiconductors [199, 235], resulting in a change in morphology. Fig. 5.12 shows the AFM images of thin films of various thicknesses, grown at LT with the same deposition rate of 0.3 nm/min and annealed to RT. The numerical results extracted from the AFM data are presented in Fig. 5.13. We observe the presence of numerous randomly oriented islands that do not exhibit the same needle-like morphology as the RT-grown films. Generally, the islands are much higher and are not as uniform as those of RT-grown films. For the 7 nm-thick film depicted in Fig. 5.12 (a) we observe that the surface coverage is much smaller than the one of RT-grown film of comparable thickness. The extracted data shows that the coverage for the LT-grown film is about 17% when for the 8 nm-thick RT-grown film is $\sim 32\%$. The inter-island distance $D_{\mathrm{ii}} = 537 \pm 233$ nm, while the GISAXS data shows the correlation length

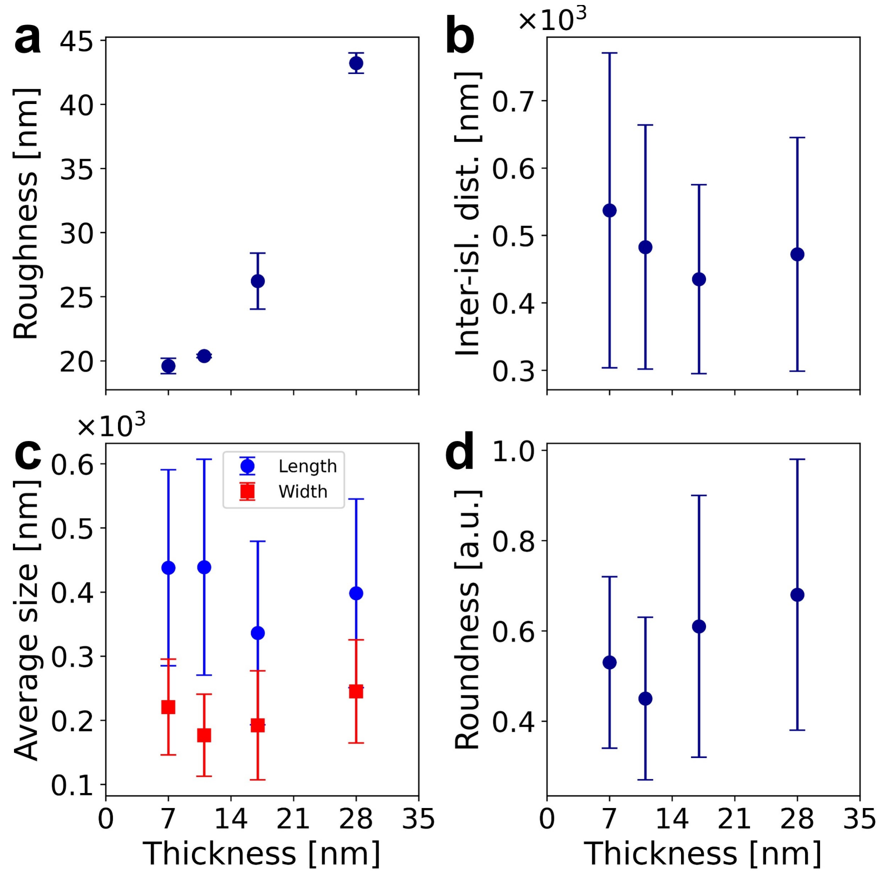


***Figure 5.13:*** *Numerical values extracted from AFM images of the LT-grown films and plotted versus film thickness: rms roughness (a), inter-island distance (b), average island size (c), average roundness (d).*

$D_{\mathrm{corr}} = 41.0 \pm 0.4$ nm for the film of comparable thickness. This discrepancy can be explained by the strong dewetting during annealing of the film to RT after growth at LT. The roughness of the LT-grown films annealed to RT is high, resulting in high amount of defects and high jaggedness of the resulting images taken in tapping mode of AFM. The surface roughness equals $\sigma_{\mathrm{RMS}} = 20.2 \pm 0.6$ nm versus $\sigma_{\mathrm{RMS}} = 12.7 \pm 0.1$ nm for the RT-grown film. The average length of the islands is $438 \pm 153$ nm and the average width is $221 \pm 75$ nm. The mean roundness of the islands is $0.53 \pm 0.19$, which is closer to the round particles than the islands appearing in the RT-grown sample ($0.23 \pm 0.16$).

AFM images of the thicker films grown at LT ($d = 11$ nm and $d = 17$ nm) presented in Fig. 5.12 (a) and (b), respectively, reveal that the form of the islands is not influenced much by the film thickness. For the 17 nm-thick film, the surface coverage is about 26%, and the inter-island distance $D_{\mathrm{ii}} = 435 \pm 159$ nm, while the GISAXS data shows the correlation length $D_{\mathrm{corr}} = 63.0 \pm 0.8$ nm for the film of comparable thickness. Similarly to the previous results, this discrepancy can be explained by the strong dewetting during annealing of the film to RT after growth

at LT. The average length of the islands is $336 \pm 143$ nm and the average width is $192 \pm 85$ nm. The mean roundness of the islands is $0.61 \pm 0.22$.

For the thickest LT-grown film ($d = 28$ nm) the surface coverage is still low, namely $\sim 23\%$, while the the inter-island distance $D_{\mathrm{ii}} = 472 \pm 173$ nm while the GISAXS data shows the correlation length $D_{\mathrm{corr}} = 65.0 \pm 0.9$ nm for the film of comparable thickness. The surface roughness is $\sigma_{\mathrm{RMS}} = 44.0 \pm 0.8$ nm. The average length of the islands is $398 \pm 147$ nm and the average width is $245 \pm 80$ nm, while the roundness equal $0.68 \pm 0.30$.

We conclude that the comparison of *ex situ* and *in situ* morphology for the LT-grown films is not reliable, because of a strong dewetting that occurs during the annealing of the film to RT. We speculated that it leads to the dewetting and desorption of dbSeQ molecules from the substrate and the smooth dbSeQ film grown at LT becomes very rough, with many separated islands on the substrate.

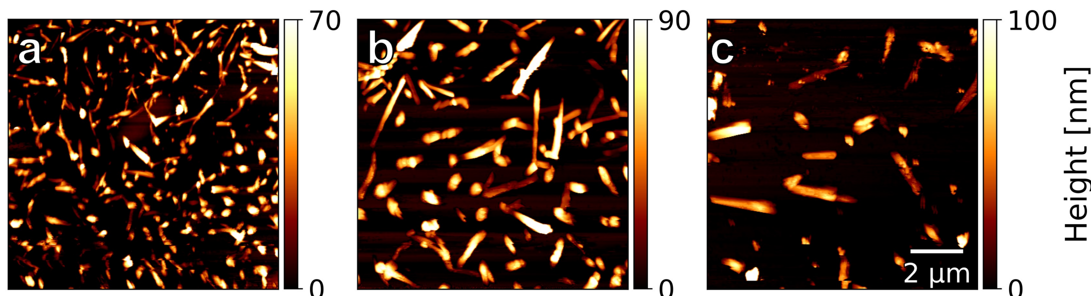


***Figure 5.14:*** *AFM images of dbSeQ thin films ($d = 9$ nm) grown on Si/SiO$_x$ with a same deposition rate of 0.3 nm/min at various substrate temperatures: 308 K (a), 318 K (b), and 328 K (c).*

After the LT growth, the next step in our investigations was a deposition at higher substrate temperatures to see how the higher thermal energy influences the film morphology. Fig. 5.14 contains images of thin films with nominal thickness of 9 nm grown at the same deposition rate of 0.3 nm/min, but at different substrate temperatures, namely 308, 318 and 328 K, respectively. Qualitatively, we notice the decrease in the number of islands on the substrate surface with a temperature increase.

For the film grown at 308 K (Fig. 5.14 (a)) the surface coverage is slightly above 21%, which is slightly lower than the coverage for the RT-grown film ($\sim 32\%$). The inter-island distance $D_{\mathrm{ii}} = 554 \pm 199$ nm, while for the RT-grown film $D_{\mathrm{ii}} = 431 \pm 151$ nm.The average length of the islands is $824 \pm 339$ nm and the average width is $220 \pm 58$ nm. The mean roundness of the islands is $0.32 \pm 0.19$ and the roughness is $\sigma_{\mathrm{RMS}} = 22.1 \pm 0.4$ nm.

For the film grown at 318 K (Fig. 5.14 (b)), the surface coverage is about 24%, and the inter-island distance $D_{\mathrm{ii}} = 1024 \pm 429$ nm, the average length of the islands is $1084 \pm 590$ nm and the average island width is $283 \pm 82$ nm. The mean roundness of the islands is $0.32 \pm 0.16$.

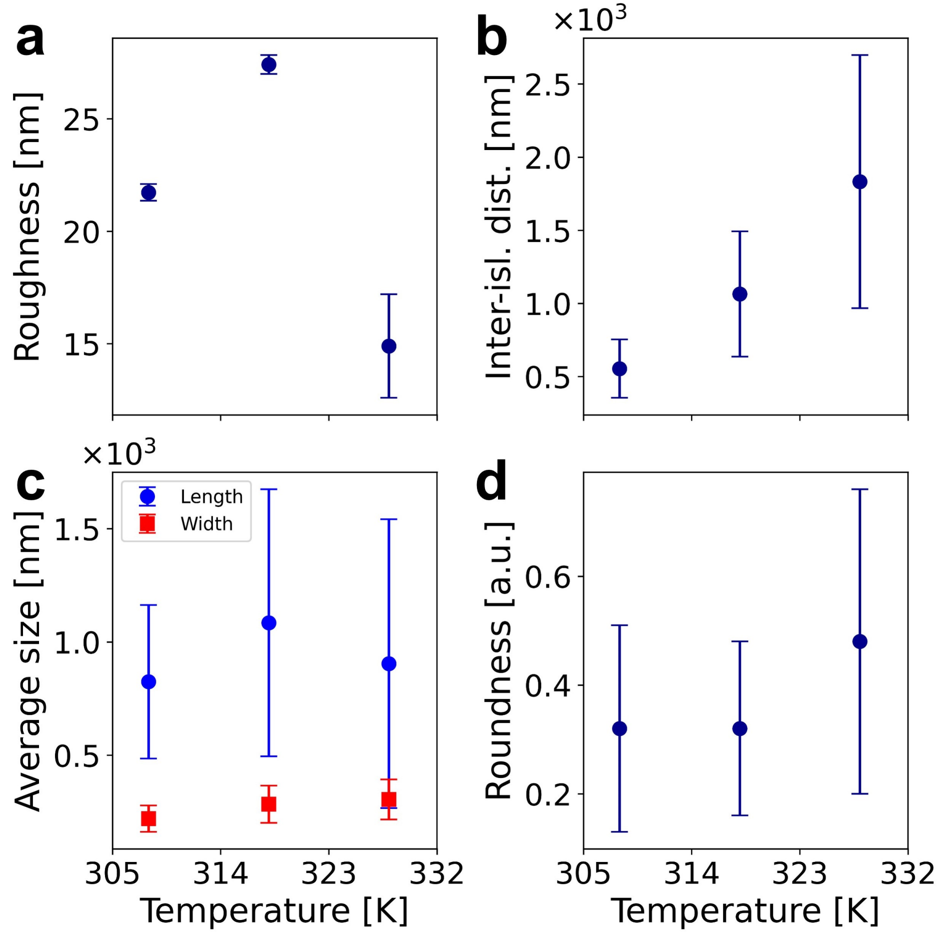


***Figure 5.15:*** *Numerical values extracted from AFM images of the LT-grown films and plotted versus film thickness: rms roughness (a), inter-island distance (b), average island size (c), average roundness (d).*

For the last film deposited at 328 K (Fig. 5.14 (c)) the desorption due to the elevated substrate temperatures is evident from the small amount of islands on the substrate, and the extracted surface coverage is slightly below 15%. Consequently, inter-island distance increases to $D_{\text{ii}} = 1832 \pm 865$ nm. The average length of the islands is $904 \pm 637$ nm and the average width is $304 \pm 88$ nm. The mean roundness of the islands is $0.48 \pm 0.28$. Interestingly, the film roughness decreases to $\sigma_{\text{RMS}} = 17.2 \pm 2.4$ nm.

From the numerical data, presented in Fig. 5.15 we see that the average size and the roundness remain largely unchanged, but there is a clear trend of the increase in inter-island distances with a temperature. We conclude that higher substrate temperatures give rise to the increased surface diffusion and desorption processes, which leads to fewer islands on the substrate surface.

As stated previously, the other factor that influences the resulting film morphology is the deposition rate [236]. The AFM images for 9 nm-thick films deposited

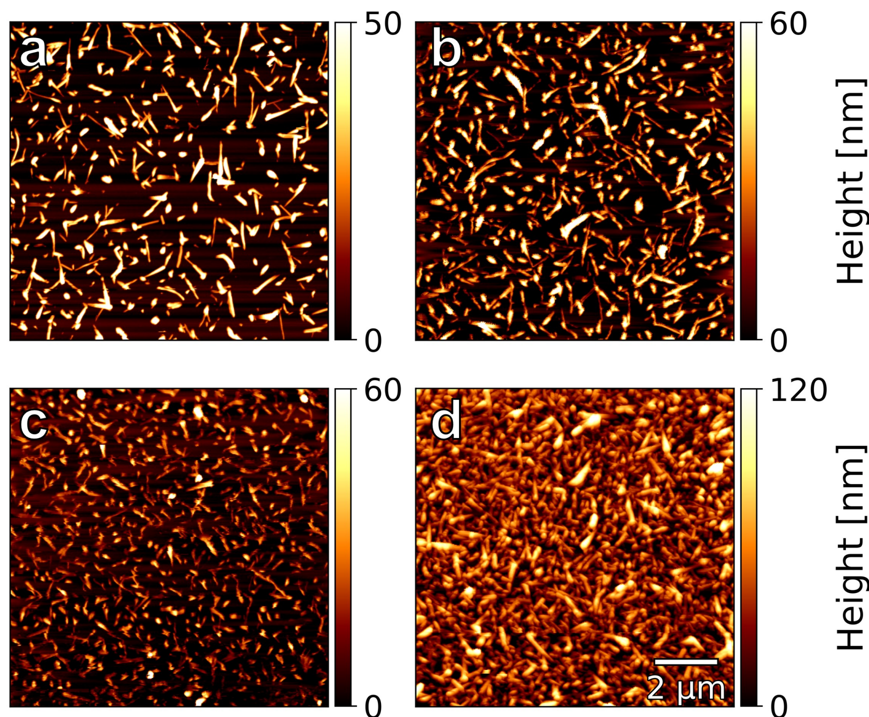


***Figure 5.16:*** *AFM images of dbSeQ thin films ($d = 9$ nm) grown on Si/SiO$_x$ at RT with various deposition rates: 0.13 nm/min (a), 0.3 nm/min (b), and 0.52 nm/min (c). Thin film ($d = 35$ nm) grown at high deposition rate 1 nm/min (d).*

at RT, at different growth rates of 0.13, 0.3, and 0.52 nm/min are presented in Fig. 5.16 (a)-(c). Fig. 5.16 (d) presents the AFM image of a thicker film ($d = 35$ nm) deposited at higher deposition rate (1 nm/min). For the properties comparison that were used in Fig. 5.17 we focus only on 9 nm-thick films.

For the film grown with deposition rate of 0.13 nm/min (Fig. 5.16 (a)) the surface coverage is slightly above 23%. The inter-island distance $D_{\text{ii}} = 558 \pm 247$ nm. The average length of the islands is $687 \pm 291$ nm and the average width is $113 \pm 33$ nm. The mean roundness of the islands is $0.23 \pm 0.18$ and the roughness is $\sigma_{\text{RMS}} = 13.7 \pm 0.1$ nm.

For the next film grown with rate 0.30 nm/min (Fig. 5.16 (b)) we see that the roughness and roundness increase slightly (to $15.9 \pm 0.1$ nm and $0.29 \pm 0.19$, respectively) compared to film with lower deposition rate, but the inter-island distance decreases to $D_{\text{ii}} = 502 \pm 179$ nm. The average length of the islands is $673 \pm 293$ nm and the average width is $152 \pm 47$ nm. The surface coverage remains almost the same at $\sim 25\%$.

For the next film grown with rate 0.52 nm/min (Fig. 5.16 (c)) we observe the rapid decrease in average island sizes, where the average length of the islands is $497 \pm 190$ nm and the average width is $130 \pm 56$ nm. The mean roundness of the islands is $0.30 \pm 0.17$. The roughness decreases drastically to $\sigma_{\text{RMS}} = 10.0 \pm 0.2$ nm,

indicating smoothening of the film. The inter-island distance decreases to $D_{\text{ii}} = 413 \pm 134$ nm.

For the film with higher nominal thickness of 35 nm, grown at a high deposition rate of 1 nm/min, we observe that the substrate is almost covered by dbSeQ (surface coverage is around 97%). At the same time mean roundness of the islands remains almost the same and is $0.30 \pm 0.17$. The average length of the islands is $582 \pm 219$ nm and the average width is $218 \pm 148$ nm. Interestingly, that the film has roughness $\sigma_{\text{RMS}} = 22.4 \pm 0.3$ nm. A similar trend of increasing surface smoothness with higher deposition rates has also been previously observed in both organic materials and metals [45, 237].

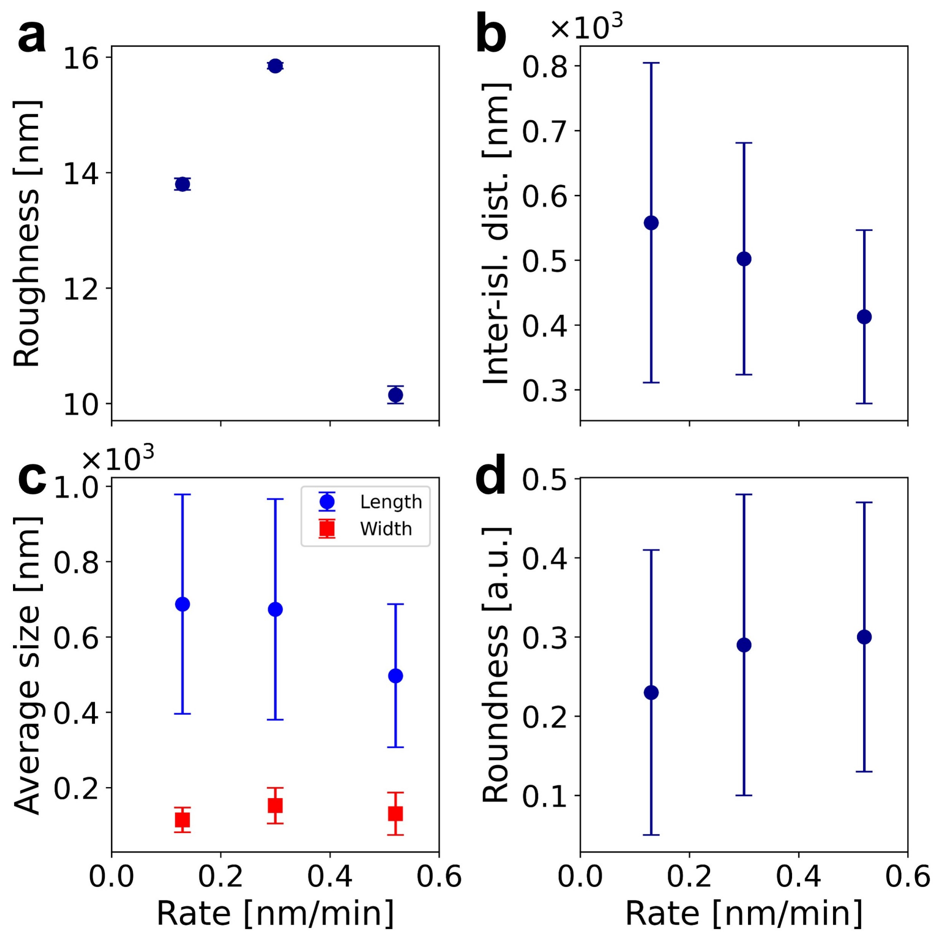


***Figure 5.17:*** *Numerical values extracted from AFM images of the LT-grown films and plotted versus film thickness: rms roughness (a), inter-island distance (b), average island size (c), average roundness (d).*

The general trend observable in Fig. 5.17 is the decrease of inter-island distance with a rate increase. The surface coverage and the mean roundness remain largely unchanged, while the average length and roughness decreases. It correlates with the general idea that during vacuum deposition an increase in particle flux leads

to a lower surface diffusion time, thus the deposited molecule has less time to diffuse and for example coalescence with another island before the next molecule arrives on the substrate. It results in generally smoother films with smaller islands. A similar trend of decreasing grain size and increasing surface smoothness with higher deposition rates has also been previously observed in both organic materials and metals [45, 237].

## 5.5 Crystalline structure of the films

To explore the molecular structure of dbSeQ thin films, we used *ex situ* GIWAXS. The reciprocal space maps from GIWAXS measurements of thin films with a nominal thickness of 50 nm, grown at RT and LT, are presented in Fig. 5.18 (a) and (b), respectively.

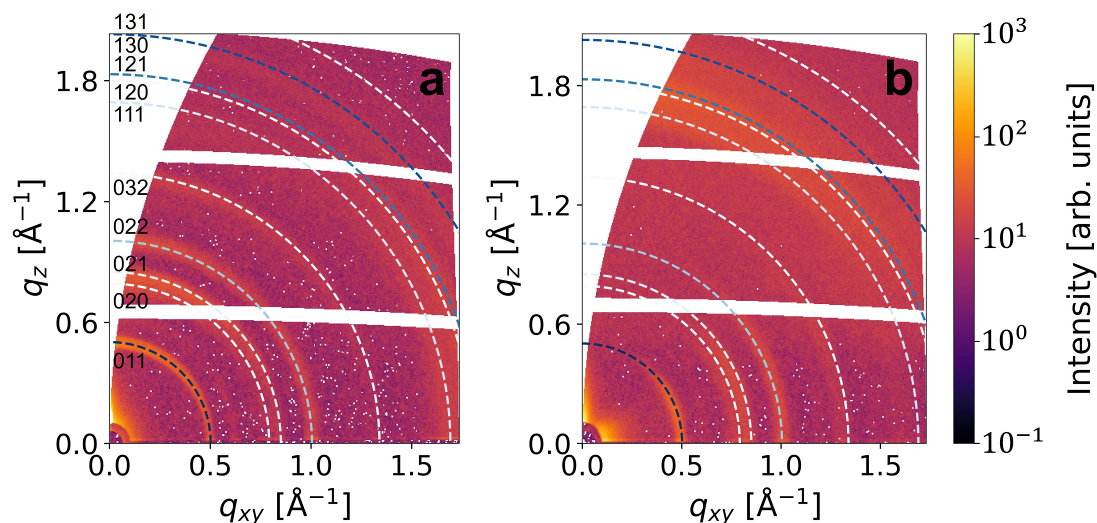


***Figure 5.18:*** *Reciprocal space maps of dbSeQ thin films with a nominal thickness of 50 nm, grown at RT (a) and LT (b). The dashed rings indicate the positions of the diffraction peaks corresponding to the dbSeQ structure, as determined from the single-crystal analysis [106, 170].*

For the RT-grown and LT-grown films of neat dbSeQ, we observe the difference in the GIWAXS patterns caused by the reorientation of the unit cells on the substrate under the influence of substrate temperature. Thin films of dbSeQ grown at RT show the Debye-Scherrer rings at $q = 0.50, 0.79, 0.85, 1.00, 1.34$ Å$^{-1}$ with the maximum of intensity aligned along $q_z$ and rings at $q = 1.69, 2.03, 2.26$ Å$^{-1}$ with the maximum of intensity aligned along $q_{xy}$. This corresponds to the known dbSeQ structure with the unit cell parameters $a = 3.88$ Å, $b = 15.85$ Å, $c = 20.33$ Å, $\alpha = \gamma = 90°$, $\beta = 90.567°$ with the preferred [001] orientation ($\sigma$-phase with the edge-on orientation of molecules) as depicted in Fig. 5.19 (left). For films with lower nominal thicknesses, the diffraction patterns remain largely unchanged, with

the intensity scaling proportionally to the thickness. The observed Debye-Scherrer rings correspond to the previously determined single-crystal structure of dbSeQ and indicate the randomly oriented domains of dbSeQ on the surface [155, 156].

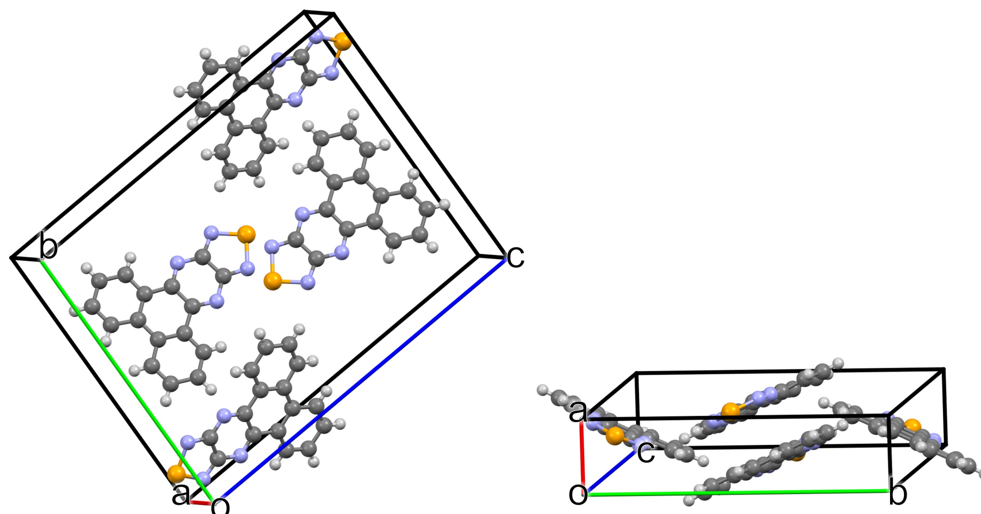


***Figure 5.19:*** *The predominant orientations of the dbSeQ unit cell, namely, 011 plane perpendicular to the substrate at RT (left), and parallel to the substrate at LT (right).*

A key distinction between the LT- and RT-grown films lies in the azimuthal intensity distribution of the (*0kl*) diffraction peaks. The LT-grown dbSeQ film also shows the Debye-Scherrer rings at the same $q$-values, but compared to the RT-grown film, most of the intensity for rings at $q = 0.50, 0.79, 0.85, 1.00$ and $1.34$ Å$^{-1}$ is aligned along $q_{xy}$, and for rings at $q = 1.69, 2.03, 2.26$ Å$^{-1}$ the most of intensity is aligned along $q_z$. This intensity realignment indicates the [100] orientation of the same unit cell corresponding to the $\lambda$-phase of the dbSeQ, where the molecules exhibit the face-on orientation as depicted in Fig. 5.19 (right). The angular distribution of the Bragg peak intensity for the (*011*) plane exhibits a full width at half maximum (FWHM) of 51° for LT-grown films and 41° for RT-grown films (Fig. 5.20), indicating a noticeable but moderate alignment. In contrast, the diffraction intensity from the (*1kl*) planes shows an opposite trend, with the majority of the intensity aligned along $q_{xy} = 0$ Å$^{-1}$ for LT films, while it aligned along $q_z = 0$ Å$^{-1}$ for RT films. Importantly to note the results for the LT-grown film were obtained at RT; therefore, these data are for the annealed film after its dewetting.

These results suggest that the crystalline domains formed during LT deposition are predominantly oriented with the b- and c-axes of the unit cell parallel to the substrate, resulting in the a-axis being perpendicular to the substrate surface and the molecules adopting a tilted face-on configuration. In contrast, films grown at RT exhibit a 90° rotation of the unit cell, with the (*011*) plane perpendicular to the substrate surface and the a-axis parallel to it. In this arrangement, the

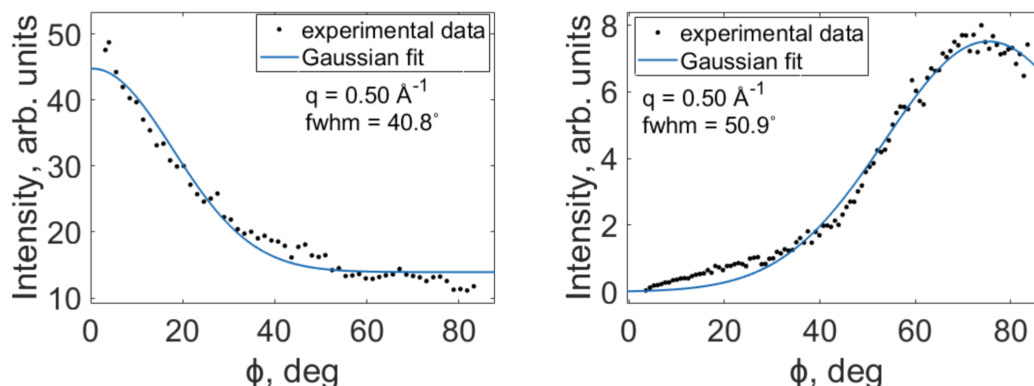


***Figure 5.20:*** *Angular distributions of the diffracted intensity at* $q_z = 0.50$ Å$^{-1}$ *(011 Bragg peak) extracted from the q-map of dbSeQ films grown at RT (left) and LT (right), as shown in Fig. 5.18. The intensity profile for the both films has been corrected for the background and* ϕ *stands for azimuthal angle.*

molecules exhibit a tilted edge-on configuration, leading to $\pi$-stacking along the substrate surface at RT and perpendicular $\pi$-stacking at LT, consistent with the AFM data.

The structural differences observed between dbSeQ films grown at LT and RT are analogous to those reported for other organic semiconductors such as pentacene, diindenoperylene and $\alpha$-sexithiophene [199, 235], though dbSeQ films exhibit a higher degree of mosaicity. Previous studies have proposed that at lower substrate temperatures, molecules initially adopt a face-on orientation to maximize van der Waals interactions with the substrate but lack the thermal energy necessary to transition to the edge-on orientation observed at RT [199, 238, 239]. However, this explanation suggests the formation of energetically favorable closed monolayers, which is inconsistent with the AFM data for dbSeQ films grown at LT and annealed to RT.

## 5.6 Optical Properties

To explore the electronic structure of thin films grown we implemented absorption spectroscopy in UV-Vis range and photoluminescence spectroscopy.

Fig. 5.21 shows the UV-Vis absorption spectra for dbSeQ thin films with a nominal thickness of 30 nm, deposited on quartz substrates at both RT and LT and normalized to film thickness. For the RT-grown film we observe five absorption peaks, at 2.50, 2.85, 3.17, 3.90 and 4.89 eV. In the region between 2 and 3.5 eV, there is a pronounced peak at 2.85 eV, accompanied by two lower-intensity peaks at 2.50 eV and 3.17 eV. Similarly to other $\pi$-extended chalcogenadiazoles [195, 240, 241], the absorption spectrum of the dbSeQ thin film grown at RT, resembles the overall shape, but is broadened and red-shifted compared to the

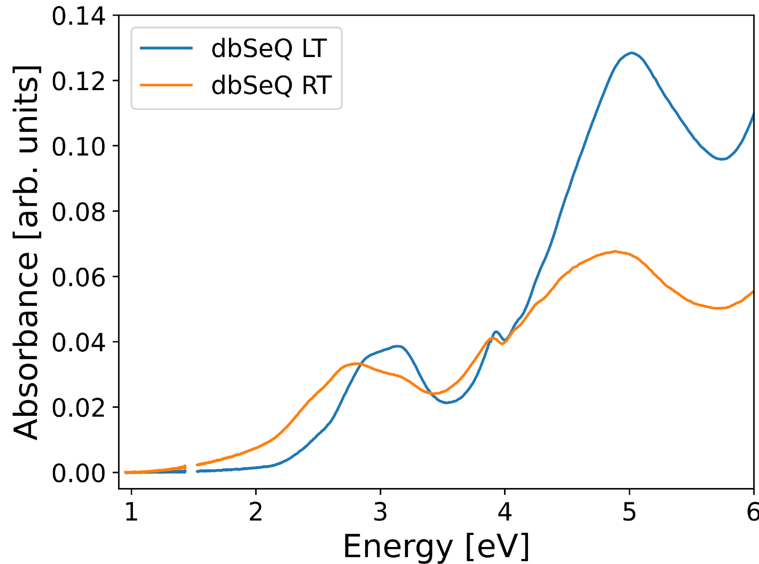


***Figure 5.21:*** *Absorption spectrum of RT- and LT-grown films of dbSeQ.*

absorption spectrum in solution. Additionally, sub-optical band gap absorbance probably results from light scattering on the rough thin film surface.

For the LT-grown film, we observe an absorption spectrum that generally resembles that of the RT-grown film but with some differences in realtive peak intensities. The position of the maximum peak remains largely unchanged, with the exception of the peak at 3.90 eV for the RT-grown film, which exhibits a slight red shift of 0.09 eV for the LT-grown film. The peak at 3.17 eV in the LT film has the highest intensity among adjacent ones, while for the RT-grown film the peak at 2.50 eV has the highest intensity. The absorption peak at 4.89 eV for the LT-grown film has much higher intensity compared to the RT-grown film. Considering the GIWAXS data, we attribute peaks at 2.85 and 3.17 eV to different electronic transitions with differently oriented transition dipole moments (TDMs). The molecular tilt toward the substrate and significant mosaicity explain the subtle differences between the optical spectra of RT and LT films. We attribute these differences to the partial reorientation of the dbSeQ crystallites in the thin film during LT growth.

To further analyze the optical properties, temperature-dependent photoluminescence (PL) measurements were conducted. With a 532-nm laser excitation, only the low-energy shoulder of peak at 2.50 eV is excited. At 290 K, the PL spectra for both the RT- and LT-grown dbSeQ films (Fig. 5.22 (a)) show three peaks at 1.75 eV, 1.87 eV and 2.07 eV. In the RT-grown film, the peak at 2.07 eV is the most intense, with other two peaks contributing to a broad lower energy tail. A significant Stokes shift of 0.43 eV, previously observed in selenium-containing chalcogenadiazoles [242], is also evident.

For the LT-grown film, the relative intensities shift again: peak at 2.07 eV de-

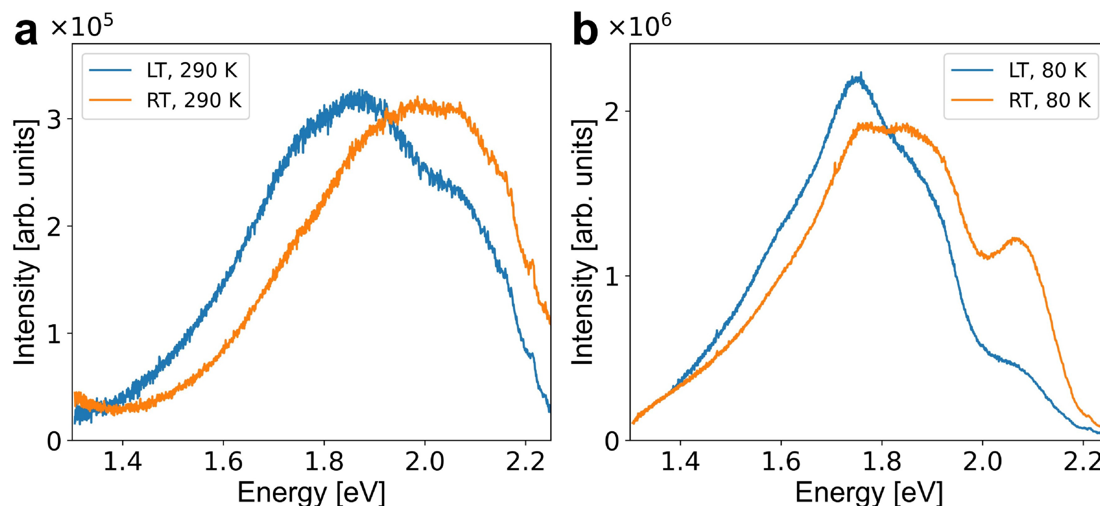


***Figure 5.22:*** *PL spectra of dbSeQ thin films with a nominal thickness of 30 nm grown at RT and LT, measured at 290 K (a) and 80 K (b).*

creases, while peak at 1.75 eV and peak at 1.87 eV become more prominent. These differences between RT and LT films become even clearer at 80 K (Fig. 5.22 (b)), where peak narrowing occurs, and the relative intensity changes are more pronounced. Specifically, the peak at 2.07 eV weakens significantly in the LT-grown film, while the peak at 1.75 eV intensifies. A similar trend is observed in the RT film, although the peak at 2.07 eV retains higher intensity.

## 5.7 Summary and conclusion

In summary, the present study has explored the growth behavior and optical properties of novel semiconductor material - dbSeQ. Furthermore, we have studied the growth of these systems at LT and have delved into the structural changes during their annealing to RT. Additionally, we studied the influence of the rate and elevated substrate temperatures on the growth behavior.

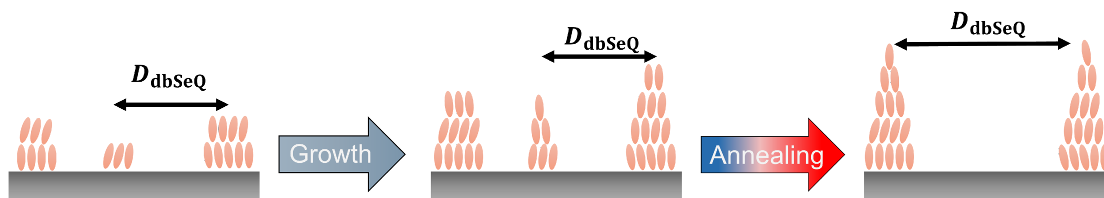


***Figure 5.23:*** *Schematic representation of growth and annealing behavior of RT-grown dbSeQ.* $D_{dbSeQ}$ *stands for correlation length of dbSeQ.*

It was found that dbSeQ on $Si/SiO_x$ substrate at RT grows in the form of rough, randomly oriented, needle-shaped, long crystallites. The correlation distances

obtained by GISAXS and AFM are in the sub-$\mu$m range. Annealing of the film increases the correlation distance, due to the desorption of dbSeQ from the substrate. Films of dbSeQ crystallize predominantly in the $\sigma$-phase, where the molecules are standing with a tilted edge-on configuration. We confirmed quantitatively that films grown at RT exhibit a rapid roughening phenomenon. The simplified growth and annealing schema of the LT-grown dbSeQ film is shown in Fig. 5.23. The absorption spectrum in the UV-Vis range exhibits five distinct peaks and resembles the one measured in solution. The extinction spectrum exhibits three distinct peaks that are distinct at 80 K.

Conversely, the growth of dbSeQ at LT is characterized by significantly smaller correlation lengths and lower roughness, compared to the RT-grown film, which we attribute to the change in the molecular orientation of dbSeQ. An important characteristic of LT-grown dbSeQ films is low thermal stability. It was observed that the low thermal stability of the LT-grown dbSeQ films resulted in strong dewetting during their annealing to RT. This, in turn, resulted in high roughness of the resulting film. The resulting islands are generally smaller and more circular than that observed for the RT-grown film. From the GIWAXS results, it is evident that the crystallites exhibit the $\lambda$-phase in contrast to the $\sigma$-phase formed during the RT growth. The simplified growth and annealing schema of LT-grown dbSeQ film is shown in Fig. 5.24. This change in molecular orientation leads to alterations in the absorption spectrum, resulting in a variation in the relative intensity of the peaks, as was previously found for the RT and LT-grown DIP films by G.Duva et al. [199]. The extinction spectrum exhibits three distinct peaks that are distinct at 80 K.

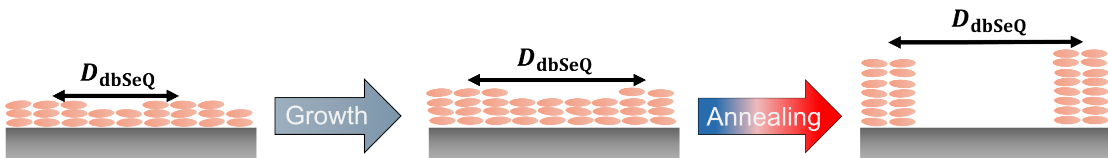


***Figure 5.24:*** *Schematic representation of growth and annealing behavior of LT-grown dbSeQ. $D_{dbSeQ}$ stands for correlation length of dbSeQ.*

We investigated the influence of elevated substrate temperature and influence of the rate on the dbSeQ thin films using exclusively AFM. We found that with increasing substrate temperature dbSeQ tends to desorb from the substrate, which results in decreased surface coverage and increased inter-island distances. In addition, the roundness of the islands increases with increasing substrate temperatures. There is a clear trend of decreasing inter-island distance with a rate increase. The increased rate leads to a decrease in the average island size and smoothening of the film. Furthermore, the change in rate does not influence the substrate coverage.

The results obtained in this chapter are crucial for the investigation of co-deposited and bilayer films with dbSeQ presented in the next chapter. We think

these results are interesting from the perspective of tailoring the morphology of films which crystallize in rod-like islands during their growth.

## Chapter 6

# Results of thin film growth and annealing kinetics of bilayer and mixed complexes incorporating dibenzoselenadiazoloquinoxaline, diindenoperylene and pentacene

This chapter contains results on the structural and optical properties of planar heterostructures and mixed thin films incorporating dibenzoselenadiazoloquinoxaline (dbSeQ), diindenoperylene (DIP) and pentacene (PEN). The results included here are partially published in [171].

The performance of organic electronic devices depends on the ability to prepare thin films that are smooth, continuous, and structurally well ordered [243, 244]. Many molecular semiconductors that display excellent intrinsic electronic properties, however, suffer from morphological instabilities during deposition or post-growth. In particular, strong roughening during growth and post-growth dewetting are challenges for the reliable preparation of high-quality thin-film devices.

Dewetting phenomena in molecular thin films have long been recognized as a challenge in organic thin-film fabrication and have been the subject of extensive studies [245] Well-studied examples of post-growth dewetting include dinaphtho[2,3-b:2',3'-f]thieno[3,2-b]thiophene (DNTT) [246, 247], $\alpha$-Sexithiophene (6T) [248], and DIP [249].

Dewetting and roughening are governed mainly by substrate–molecule and molecule-molecule interactions. During deposition, dewetting tendencies may already manifest and intermingle with kinetic roughening processes, making it challenging to disentangle the contributions of thermodynamics and kinetics. After growth, additional reorganization can occur dependent on temperature, revealing the activation barriers associated with interfacial instabilities.

As was shown in the previous chapter (see Chap. 5), dbSeQ despite its excellent electronic properties has a tendency to dewet on $Si/SiO_x$ substrates that appears to limit its applicability in optoelectronic devices. To improve the morphology of the resulting film and create charge transfer states, we combined dbSeQ with two donor materials, DIP and PEN, extensively studied organic semiconductors with

excellent electronic properties and high structural order [57, 79, 228, 250–255]. In this chapter, we study both their growth and structure as well as complementary optical properties.

By comparing low-temperature (LT) growth with deposition at room temperature (RT), we probe how temperature controls the onset and strength of dewetting during film formation. Furthermore, by annealing the LT-grown films to room temperature, we study the post-growth evolution of morphology, allowing us to extract information on the activation temperature of the dewetting transition. We examined the growth and structure of both on-top deposition and co-deposition of dbSeQ with DIP and PEN. *In situ* X-ray scattering is an ideal tool to gain insights into dewetting growth process and associated thin film parameters in real-time (layer thickness, roughness, island sizes) [41]. X-ray reflectivity (XRR), grazing-incidence wide-angle X-ray scattering (GIWAXS), and grazing-incidence small-angle X-ray scattering (GISAXS) provided insights into thin-film structure and growth mechanisms, while atomic force microscopy (AFM) and optical absorption spectroscopy allowed for a detailed analysis of morphological and optical properties. Our results reveal differences in the growth dynamics of dbSeQ in layered and co-deposited systems, shedding light on templating effects and mixing scenarios. By comparing these findings, we establish a direct correlation between the deposition conditions, molecular interactions, and the resulting film morphology, which is crucial for the design of next-generation organic electronic devices.

## 6.1 Morphology evolution during growth

The ability to deposit thin films in a portable vacuum chamber under UHV makes it possible to study film growth and, more specifically, morphology evolution *in situ* during film growth using the GISAXS technique. We employed GISAXS to observe the changes in the surface morphology of the heterostructures of dbSeQ with DIP and PEN at both RT and LT. The GISAXS investigation of neat DIP and PEN thin films grown on Si/SiO$_x$ are well known in the literature [119, 256], and the GISAXS data for dbSeQ were described in detail in a previous chapter (Sec. 5.2).

### 6.1.1 Morphology evolution during growth of the heterostructures incorporating dbSeQ and DIP

To understand the influence of the organic templating layer on the growth of the dbSeQ overlayer, we studied the growth of the bilayer dbSeQ/DIP thin films. Fig. 6.1 (a) presents the GISAXS patterns for the growth of bilayer dbSeQ/DIP film (nominal thicknesses $d_{\mathrm{nom}}$(dbSeQ) = 30 nm, $d_{\mathrm{nom}}$(DIP) = 20 nm) on Si/SiO$_x$ at RT.

The two pronounced intensity peaks observed at the initial stage of the deposition (Fig. 6.1 (a), top part) correspond to the pre-deposited at RT DIP layer. As the

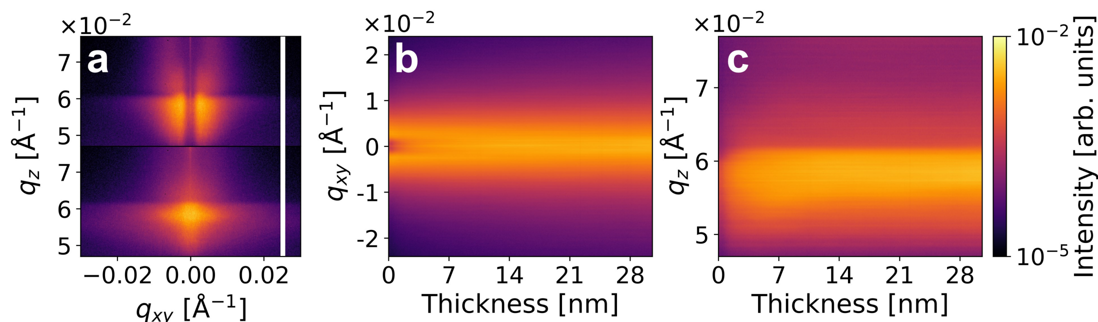


***Figure 6.1:*** *In situ GISAXS data for the growth of bilayer dbSeQ/DIP thin film on Si/SiO$_x$ at RT ($d_{\mathrm{nom}}$(dbSeQ) = 30 nm). 2D GISAXS patterns measured at the beginning (top part) and end (bottom part) of the deposition (a), and evolution of the intensity in the horizontal cut of the GISAXS pattern (integrated in the range of $q_z = 0.056 - 0.060$ Å$^{-1}$) (b) and vertical cut (integrated in the range of $q_{xy}$ =-0.001 − 0.001 Å$^{-1}$) (c) during the deposition as a function of the thickness. The white vertical lines are presenting intermodular gaps of the detector.*

deposition reaches its final stage (Fig. 6.1 (a), bottom part), the initially discernible peaks merge. Fig. 6.1 (b, c) shows waterfall plots of horizontal and vertical line cuts. The horizontal line cuts show that at the initial growth stage there are two DIP-related side peaks present, corresponding to a correlation length $D_{\mathrm{corr}}$ equals $238 \pm 3$ nm. At a nominal thickness of 1 nm, dbSeQ-related peaks are visible at low $q$. Unfortunately, because of the large correlation length of the dbSeQ islands it is not possible to resolve the peaks and extract peak position. The vertical line cut data in Fig. 6.1 (c) show the minor differences compared to the growth of neat dbSeQ at RT. It is hypothesized that in a manner analogous to the case of RT growth of a neat dbSeQ, island formation occurs from the onset of deposition. It is also hypothesized that there is a mutual influence between the two compounds, where dbSeQ growth in large islands with the large corresponding correlation lengths which is evident from the merged correlation peaks. The XRR data for the RT-grown bilayer dbSeQ/DIP film presented in the next section (Fig. 6.7 (a)) show that there are no scattering features that are characteristic of the new structures, only the DIP-related features are observable during the deposition and subsequent annealing. We attribute this to the limited impact of DIP on the dbSeQ layer.

As discussed in a previous chapter, thin films of dbSeQ grown at LT have different morphology and growth behavior than those grown at RT. Similarly to the case of neat dbSeQ, the growth of dbSeQ on DIP at LT differs from its growth at RT. GISAXS data for the LT growth of bilayer dbSeQ/DIP film (nominal thicknesses $d_{\mathrm{nom}}$(dbSeQ) = 30 nm, $d_{\mathrm{nom}}$(DIP) = 20 nm) is presented in Fig. 6.2 (a) and shows significant differences compared to the RT growth of similar heterostructure. Similarly to the growth of neat dbSeQ at LT, we observe a central peak of the highest intensity during the entire deposition. This indicates a high smoothness of the film (which is confirmed by XRR measurements in

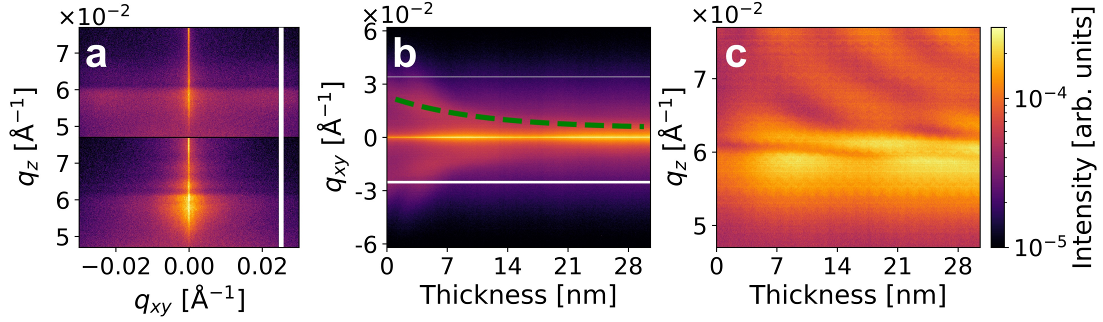


***Figure 6.2:*** *In situ GISAXS data for the growth of bilayer dbSeQ/DIP thin film on Si/SiO$_x$ at LT ($d_{\mathrm{nom}}$(dbSeQ) = 30 nm). 2D GISAXS patterns measured at the beginning (top part) and end (bottom part) of the deposition (a), and evolution of the intensity in the horizontal cut of the GISAXS pattern (integrated in the range of $q_z = 0.056 - 0.060$ Å$^{-1}$) (b) and vertical cut (integrated in the range of $q_{xy}$ =-0.001 – 0.001 Å$^{-1}$) (c) during the deposition as a function of the thickness. The green dashed line in panel (b) shows the fit result of the side peak position. The white vertical and horizontal lines are presenting intermodular gaps of the detector.*

the following section). The waterfall plot of horizontal line cuts presented in Fig. 6.2 (b), reveals that in the beginning of the deposition only DIP-related peaks (corresponding correlation length $D_{\mathrm{corr}} = 28.0 \pm 0.4$ nm) are observable. As the nominal thickness of dbSeQ equals 3 nm, we could resolve the dbSeQ-related side peaks and to extract the correlation length $D_{\mathrm{corr}} = 34.0 \pm 0.2$ nm. In the last resolvable point ($d_{\mathrm{nom}}$(dbSeQ) = 10 nm) it equals 66±5 nm. Beyond this point, the correlation length exceeds the experimental resolution. The decay in peak position can be described by an exponential function $q_{xy}(d) = q_0 + A\exp\left(-\frac{d}{d_0}\right)$, where $q_0 = 0.005$ Å$^{-1}$, $A = 0.018$ Å$^{-1}$, and $d_0 = 10.5\,\mathrm{nm}$ (dashed line in Fig. 6.2 (b)). We can conclude that the correlation length $D_{\mathrm{corr}}$ in bilayer film decays almost five times slower than the one for neat LT-grown dbSeQ. From extrapolation of the fit to the experimental data, we derived at a correlation length $D_{\mathrm{corr}} = 104$ nm for the fully grown, 30 nm thick dbSeQ film (Fig. 6.3). A vertical line cut mapping in Fig. 6.2 (c) reveals the pronounced intensity modulations that are indicating the continuous vertical layer growth, similarly to the growth of neat dbSeQ at LT. For the LT growth of bilayer dbSeQ/DIP, we assume that the observed growth behavior is analogous to that of the growth of neat dbSeQ at LT. However, at the initial stage, dbSeQ inherits the correlation length of the pre-deposited DIP layer. The evolution of the film morphology during the annealing to RT is presented in the next section.

The next step in our investigations is a co-deposition of dbSeQ with DIP at RT, and 2D GISAXS patterns taken during the RT growth of the co-deposited dbSeQ:DIP 1:1 film ($d_{\mathrm{nom}}$(total) = 36 nm) are presented in Fig. 6.4 (a). In the

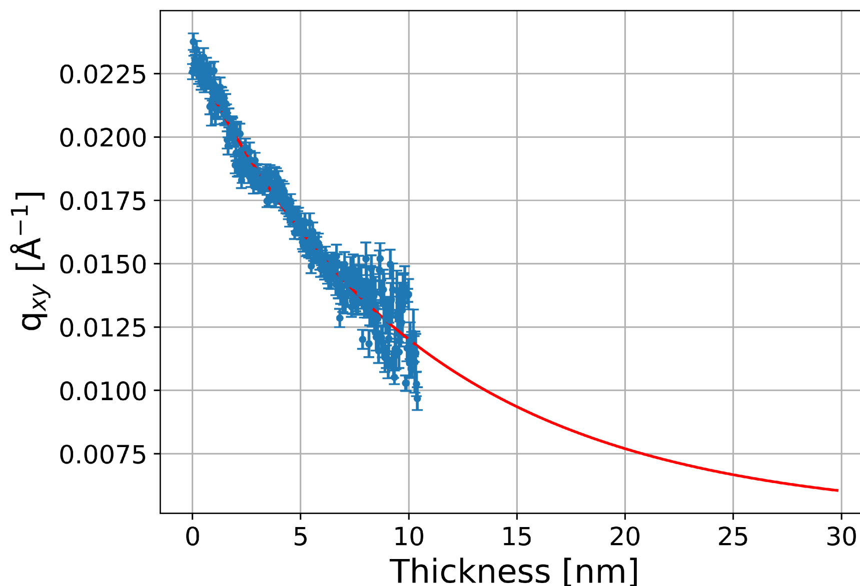


***Figure 6.3:*** *Fit (red curve) of the peak position curve (blue dots) with an exponential function, plotted versus film thickness for the LT-grown bilayer dbSeQ/DIP film.*

beginning of the deposition, we observe only a central streak which is completely covered by side peaks by the end of the deposition. This can be attributed to an increased roughness of the deposited film. We observe two sets of side peaks that belong to both compounds, dbSeQ-related peaks closer to $q_{xy} = 0$ and DIP-related peaks at larger values. In the horizontal line cut waterfall plot in Fig. 6.4 (b), we observe two distinct length scales that belong to both compounds. It is evident that the DIP- and dbSeQ-related peaks demonstrate behavior consistent with that observed for pure compounds [116, 119, 257]. We observe a completely closed layer of DIP that results in the absence of intensity in the horizontal line cut mapping at the thickness of $\approx$ 4 nm in Fig. 6.4 (b). This nominal thickness of the film corresponds to the thickness of DIP $d_{\mathrm{nom}}(\mathrm{DIP}) = 2.1$ nm which is close to one monolayer. Interestingly, that neat DIP at RT tends to form 3-5 monolayers in the beginning of the deposition in layer-by-layer mode, and in the mixture with dbSeQ it forms only one closed layer before transition to island growth. The correlation length $D_{\mathrm{corr}}(\mathrm{DIP})$ in the beginning of the deposition ($d_{\mathrm{nom}}(\mathrm{total}) = 1$ nm) equals to $63.0 \pm 0.5$ nm. Then the growth mode of DIP carries over to the island growth scenario, as can be seen from the minor changes in peak position. The correlation length as the thickness $d_{\mathrm{nom}}(\mathrm{total}) = 7$ nm equals $D_{\mathrm{corr}}(\mathrm{DIP}) = 108 \pm 1$ nm, and stays almost constant reaching at the end of the deposition ($d_{\mathrm{nom}}(\mathrm{total}) = 36$ nm) the value $D_{\mathrm{corr}}(\mathrm{DIP}) = 119.0 \pm 0.4$ nm.

In a co-deposited film, dbSeQ exhibits a behavior analogous to that of the RT growth of a neat compound, showing island growth from the initial stage of deposition, without a change in the growth mode. We could resolve dbSeQ-

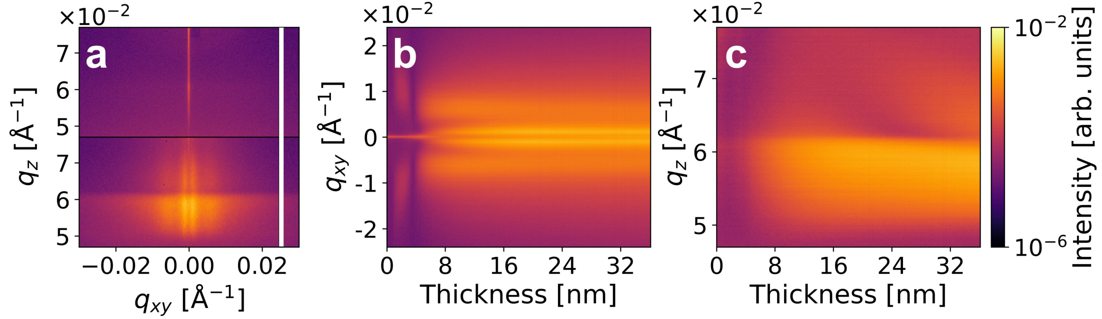


***Figure 6.4:*** *In situ GISAXS data for the growth of co-deposited dbSeQ:DIP 1:1 thin film on Si/SiO$_x$ at RT ($d_{\mathrm{nom}}$(total) = 36 nm). 2D GISAXS patterns measured at the beginning (top part) and end (bottom part) of the deposition (a), and evolution of the intensity in the horizontal cut of the GISAXS pattern (integrated in the range of $q_z = 0.056 - 0.060$ Å$^{-1}$) (b) and vertical cut (integrated in the range of $q_{xy}$ =-0.001 − 0.001 Å$^{-1}$) (c) during the deposition as a function of the thickness. The white vertical lines are presenting intermodular gaps of the detector.*

related peaks corresponding to $D_{\mathrm{corr}}$(dbSeQ) = 647 ± 6 nm at the thickness $d_{\mathrm{nom}}$(total) = 7 nm, and at the end of the deposition the correlation length $D_{\mathrm{corr}}$(dbSeQ) slightly decreases to 628 ± 4 nm. As illustrated in Fig. 6.4 (c), the vertical line cut mapping exhibited only minor alterations in comparison to the growth of pristine dbSeQ film at RT. Slight intensity modulations in the $q_z$ direction point to continuous vertical growth of the DIP layer. In the case of the co-deposited dbSeQ:DIP 1:1 film, it is suggested that phase separation should take place from the early stages of the deposition. A decrease in correlation length for the dbSeQ islands is observable in comparison to the growth of neat dbSeQ. This phenomenon can be attributed to the influence of DIP in the mixture. Fig. 6.7 (b) in SI shows the *in situ* XRR post-growth scans of the RT-grown co-deposited dbSeQ:DIP 1:1 film with a nominal thickness of 36 nm. We observe only the features related to the RT-grown DIP film, including the Bragg peak at $q_z = 0.375$ Å$^{-1}$.

### 6.1.2 Morphology evolution during growth of the heterostructures incorporating dbSeQ and PEN

Another organic material, the layer of which we predeposited to understand the influence of the organic templating layer on the growth of the dbSeQ overlayer, is PEN. Fig. 6.5 presents the waterfall plots of the horizontal and vertical line cuts from GISAXS patterns for the growth of bilayer dbSeQ/PEN film (nominal thicknesses $d_{\mathrm{nom}}$(dbSeQ) = 30 nm, $d_{\mathrm{nom}}$(PEN) = 20 nm) on Si/SiO$_x$ substrate at RT.

Due to the intense diffuse scattering from the surface roughness and, therefore, a wide central streak, the line cut at the Yoneda position of the dbSeQ (which corresponds to $q_z = 0.0558$ Å$^{-1}$) contains limited information. In the region above

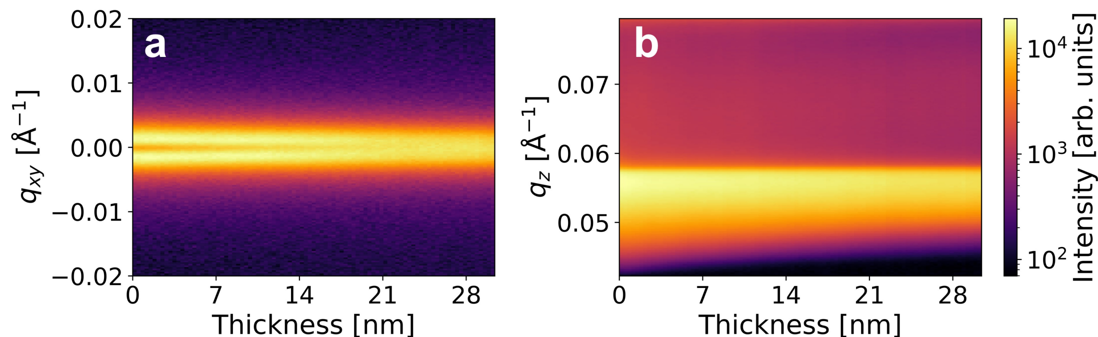


***Figure 6.5:*** *In situ GISAXS data for the growth of bilayer dbSeQ/PEN thin film on Si/SiO$_x$ at RT ($d_{nom}$(dbSeQ) = 30 nm). The evolution of the intensity in the horizontal cut of the GISAXS pattern (integrated in the range of $q_z = 0.056 - 0.060$ Å$^{-1}$) (a) and vertical cut (integrated in the range of $q_{xy}$ =-0.001 − 0.001 Å$^{-1}$) (b) during the deposition as a function of the thickness.*

$q_z = 0.098$ Å$^{-1}$ two correlation streaks are distinguishable. The horizontal line cuts in Fig. 6.5 (a) show the distinct side peaks around $q_{xy} = 0$ that tend to merge as the nominal thickness increases. It is evident that the two pronounced intensity peaks observed at the initial stage of the deposition correspond to the pre-deposited at RT PEN layer. The correlation length for these peaks $D_{corr}$ equals $349 \pm 3$ nm. During the deposition of dbSeQ, the side peaks shift towards $q_{xy} = 0$, indicating the increase in the correlation to $D_{corr} = 731 \pm 11$ nm at the nominal thickness of 15 nm. As the deposition reaches its final stage ($d_{nom}$(dbSeQ) ≈ 30 nm), we observe that the well-defined peaks, which were initially discernible, have now become indistinguishable. The vertical line cut data in Fig. 6.5 (b) shows the pronounced single Yoneda peak and no additional scattering features. We found that it shows slight differences compared to the growth of neat dbSeQ at RT. We assume that in a manner similar to the case of RT growth of a bilayer dbSeQ/DIP or neat dbSeQ film, island formation occurs from the onset of deposition. We also hypothesize that there is a mutual influence between the two compounds, where the corresponding correlation lengths for dbSeQ exceed the resolution achievable in the experiment, indicating large dbSeQ islands. We found that the *ex situ* XRR data for the RT-grown bilayer dbSeQ/PEN film presented in the next section (Fig. 6.18) in SI) show that there are no scattering features that are characteristic of the new structures, only the PEN-related features are observable after the deposition. Similarly to bilayer with DIP, we attribute the absence of new features to the limited impact of PEN on the dbSeQ layer.

To understand the mixing behavior of co-deposited films, the next step in our investigations is a co-deposition of dbSeQ with PEN at RT, and the waterfall plots from the line cuts of 2D GISAXS patterns taken during the growth of the co-deposited dbSeQ:DIP 1:1 film ($d_{nom}$(total) = 36 nm) are presented in Fig. 6.6. Initially, in the horizontal line cut waterfall plot (Fig. 6.6 (a)) we can distinguish

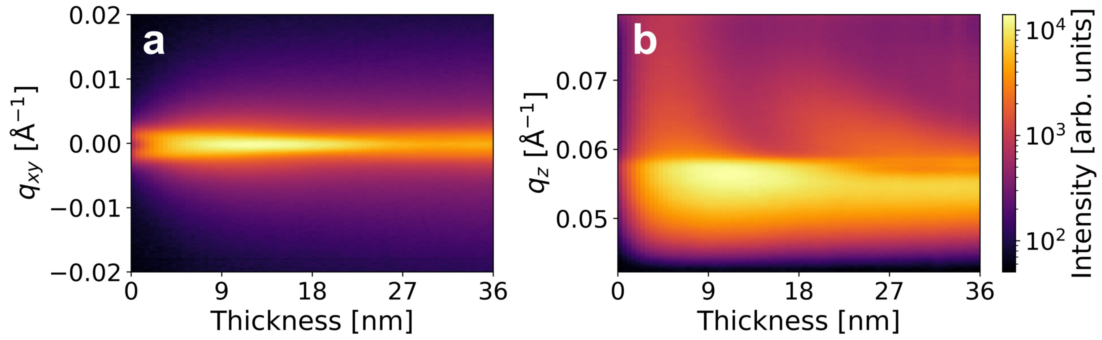


***Figure 6.6:*** *In situ GISAXS data for the growth of co-deposited dbSeQ:PEN 1:1 thin film on Si/SiO$_x$ at RT ($d_{nom}$(total) = 36 nm). The evolution of the intensity in the horizontal cut of the GISAXS pattern (integrated in the range of $q_z = 0.056 - 0.060$ Å$^{-1}$) (a) and vertical cut (integrated in the range of $q_{xy}$ =-0.001 − 0.001 Å$^{-1}$) (b) during the deposition as a function of the thickness.*

two side peaks, likely belonging to PEN islands, and at this point $D_{\mathrm{corr}}$ equals $456 \pm 5$ nm. At $d_{\mathrm{nom}}(\mathrm{total}) = 2.5$ nm peaks are covered by the central streak, indicating large correlation length for both deposited compounds. After this point, the further analysis is not feasible, because the resolution of the experimental setup is not sufficient to discrete side peaks at large $D_{\mathrm{corr}}$. The vertical line cut mapping in Fig. 6.6 (b) shows the pronounced peak at high $q_z$ values at the beginning of the deposition and another peak at $d_{\mathrm{nom}}(\mathrm{total}) = 15$ nm. Both peaks shift toward the lower $q_z$, indicating the continuous layer growth of the film. Based on *ex situ* morphology data presented in Sec. 6.3.2, we assume that co-deposited dbSeQ:PEN 1:1 film, likewise dbSeQ:DIP 1:1 film exhibit phase separation during the growth. Fig. 6.18 in shows the *ex situ* XRR post-growth scans of the RT-grown co-deposited dbSeQ:PEN 1:1 film with a nominal thickness of 36 nm. We observe only the features related to the RT-grown PEN film, including the Bragg peak at $q_z = 0.41$ Å$^{-1}$.

## 6.2 Morphology evolution during annealing of heterostructures incorporating dbSeQ and DIP

In the next step of the characterization of the thin films incorporating dbSeQ and DIP, we employed XRR and GISAXS to obtain more information about the morphology of thin films during their annealing. XRR allows us to determine the thickness and roughness values with a high degree of precision if the thin film is not very rough. It also allows for the identification of Bragg peaks associated with atomic planes that are oriented parallel to the surface in a direction perpendicular

to the substrate if the thin film is crystalline [258]. We used this technique to

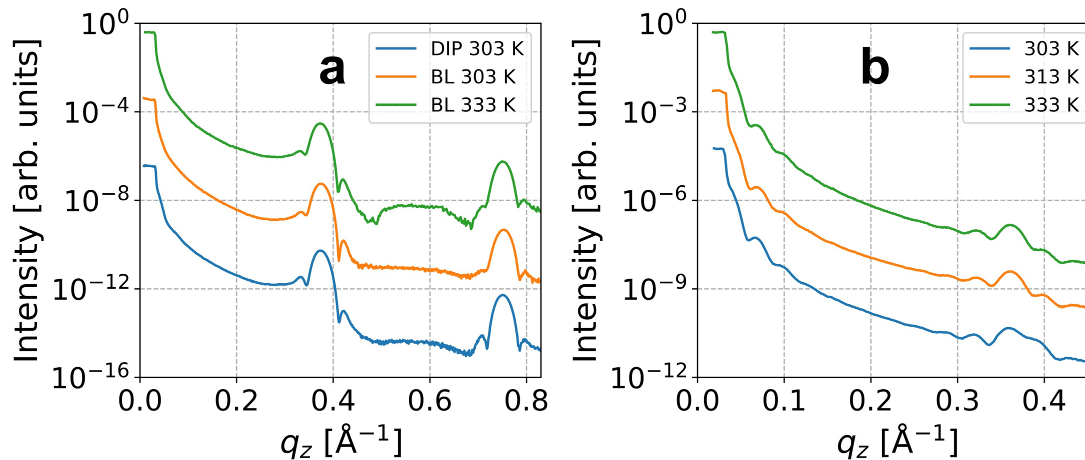


***Figure 6.7:*** *Post-growth and annealing XRR measurements of heterostructures incorporating dbSeQ and DIP grown at RT on Si/SiO$_x$: bilayer (a) and mixed (b) thin films. All curves are vertically offset for clarity.*

obtain information on the samples grown at RT and LT *in situ*. The reflectivity curves of neat DIP thin films are well known in the literature [259], and the XRR data of dbSeQ were described in detail in a previous chapter (Sec. 5.3).

To investigate the evolution of the morphology of bilayer film of dbSeQ/DIP ($d_{\text{nom}}$(dbSeQ) = 30 nm, $d_{\text{nom}}$(DIP) = 20 nm) and mixed film of dbSeQ:DIP 1:1 ($d_{\text{nom}}$(total) = 36 nm) grown at RT during their annealing to 333 K, *in situ* XRR and GISAXS measurements were performed. The post-growth annealing of the thin film was performed in three steps, by subsequent heating of the substrate to 313, 323 and 333 K, respectively.

The post-growth and annealing *in situ* XRR scans for both RT-grown heterostructures is presented in Fig. 6.7 (a) and (b). We observe minor differences in all three XRR curves for the bilayer film, as can be seen in Fig. 6.7 (a). After deposition of neat DIP layer, we observe two pronounced DIP-related Bragg peaks at $q_z = 0.375$ and $q_z = 0.750$ Å$^{-1}$ and weak Kiessig fringes in region $q_z < 0.2$ Å$^{-1}$. Near the Bragg peaks the Laue oscillations are observable. After the deposition of dbSeQ, Kiessig fringes vanish because of the increased surface roughness, and the Laue oscillations diminish slightly. There are no additional dbSeQ-related Bragg peaks visible. After the annealing to 333 K the curve remains almost unchanged, and we do not observe an increase in crystallinity or smoothing for the dbSeQ layer, significant enough to see it in the reflectivity pattern.

GISAXS patterns obtained during annealing are presented in Fig. 6.8. In the post-growth scan in Fig. 6.8 (a) we see the region of high intensity around $q_{xy} = 0$, but the side peaks are not distinguishable due to the large correlation length of dbSeQ on DIP. At T = 313 K (Fig. 6.8 (b)) we observe that the pronounced central streak appeared at $q_{xy} = 0$, but the side peaks are not distinguishable. For the

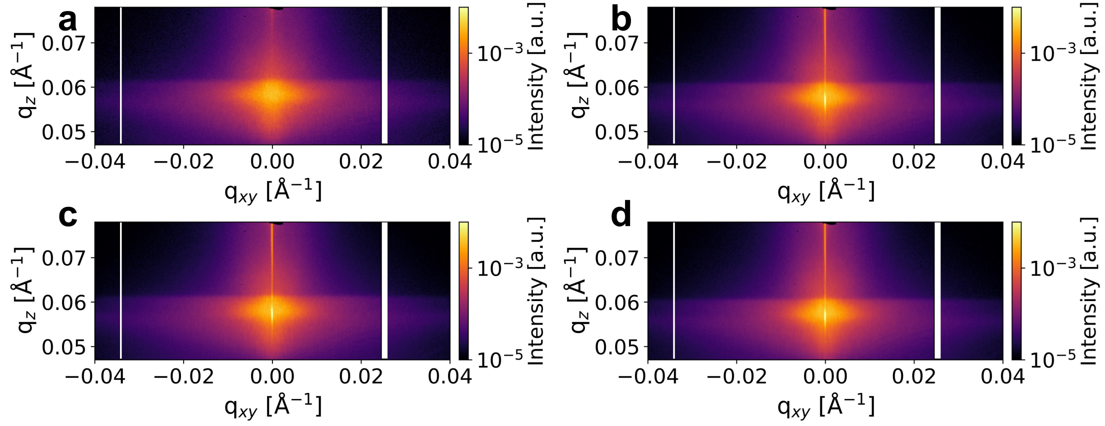


***Figure 6.8:*** *Averaged GISAXS images for post-growth and each annealing step for the RT-grown bilayer dbSeQ/DIP film: 303 K (a), 313 K (b), 323 K (c), 333 K (d). The white vertical lines are presenting intermodular gaps of the detector.*

next annealing steps depicted in Figs. 6.8 (c,d), we observe negligible changes in the GISAXS patterns compared to T = 313 K. It indicates that the annealing to 333 K does not significantly influence the morphology of the bilayer dbSeQ/DIP film.

XRR scans for the mixed dbSeQ/DIP 1:1 film are presented in Fig. 6.7 (b). Similarly to the bilayer film with DIP, we observe the Bragg reflection at $q_z$ = 0.375 Å$^{-1}$ that is related to DIP. The Kiessig fringes and Laue oscillations are more pronounced than for a bilayer film, which means a generally smoother film. Subsequent annealing does not change the reflectivity curve, indicating the stability of the film during annealing.

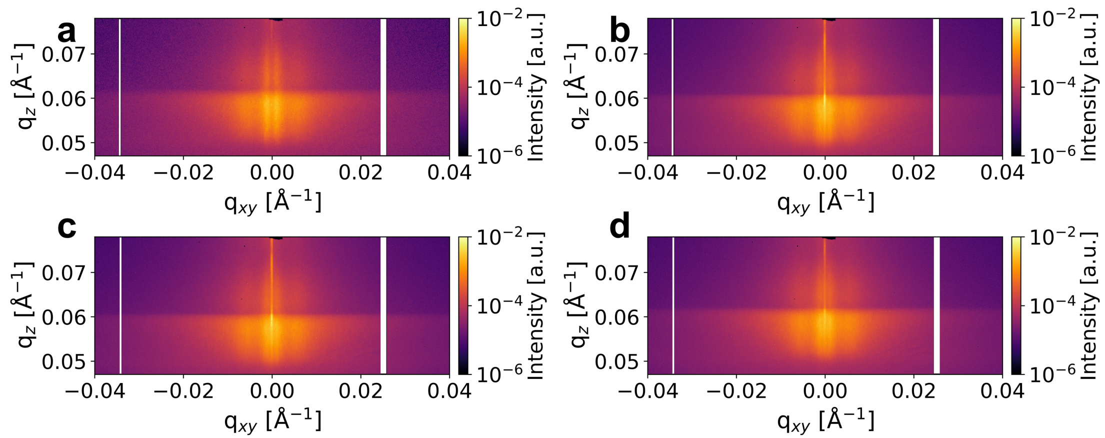


***Figure 6.9:*** *Averaged GISAXS images for post-growth and each annealing step for the RT-grown mixed dbSeQ:DIP 1:1 film: 303 K (a), 313 K (b), 323 K (c), 333 K (d). The white vertical lines are presenting intermodular gaps of the detector.*

The selected GISAXS patterns taken during the annealing of RT-grown dbSeQ:DIP 1:1 film are presented in Fig. 6.9. In the post-growth scan in Fig. 6.9 (a) two sets of side peaks related to dbSeQ and DIP are recognizable. At this point, the correlation length for DIP $D_{\mathrm{corr}}(\mathrm{DIP}) = 120.0 \pm 0.6$ nm and for dbSeQ $D_{\mathrm{corr}}(\mathrm{dbSeQ}) = 629 \pm 4$ nm. After the annealing to T = 313 K (Fig. 5.5 (b)) we observe that the pronounced central streak appeared at $q_{xy} = 0$, similarly to RT-grown bilayer dbSeQ/DIP film. Previously distinguishable dbSeQ-related side peaks are covered by the central streak and are no longer discernible. We attribute this to an increase in the correlation length due to desorption of dbSeQ. DIP-related peaks are not changing the position, meaning high thermal stability of DIP. For the next annealing steps depicted in Figs. 6.9 (c,d), we observe minor changes in the GISAXS patterns compared to the pattern at T = 313 K, where the DIP-related peaks remain at the same position and the dbSeQ-related peaks remain indistinguishable. We conclude that the presence of DIP in the mixture does not influence the thermal stability of dbSeQ and we observe the annealing behavior similar to the one of neat RT-grown dbSeQ film. At the same time, dbSeQ does not decrease the thermal stability of DIP, which is evident from the stable side peak position of the DIP-related peaks.

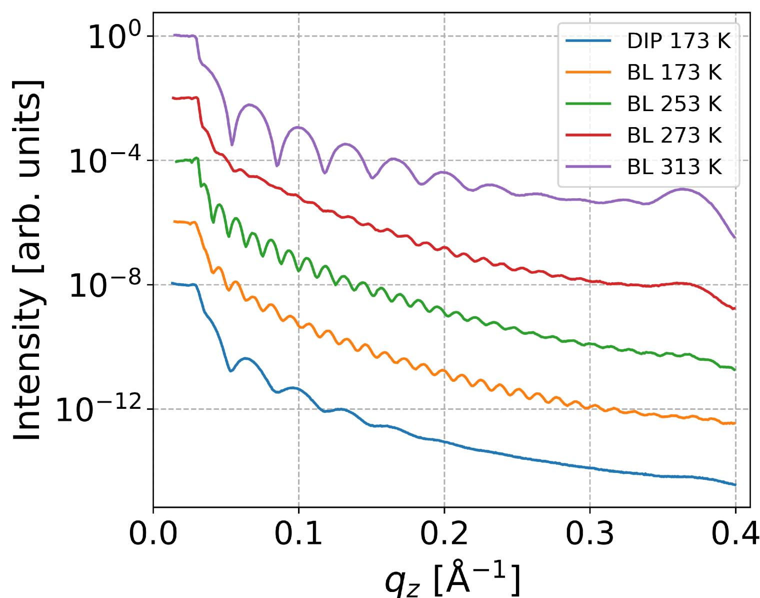


***Figure 6.10:*** *Post-growth and annealing XRR measurements of neat dbSeQ grown on Si/SiO$_x$ at LT during the annealing to RT. All curves are vertically offset for clarity. For fitting and data analysis see Fig. 6.11.*

The completely different annealing scenario from the RT-grown films was observed during the annealing of LT-grown bilayer dbSeQ/DIP film. *In situ* XRR data for bilayer dbSeQ/DIP film ($d_{\mathrm{nom}}(\mathrm{dbSeQ}) = 30$ nm, $d_{\mathrm{nom}}(\mathrm{DIP}) = 20$ nm) grown at LT are shown in Fig. 6.10. DIP films grown at low temperature on SiO$_x$ consist predominantly of $\lambda$-crystalline phase with the lying-down molecules and are

characterized by a smooth surface [113, 260]. At the same time, on the curve for the LT-grown DIP film, we observe a weak Bragg peak at approximately 0.37 $\mathring{A}^{-1}$ that is characteristic of the $\sigma$-phase of DIP with standing-up molecules, which is known to coexist with the $\lambda$-phase [115, 261, 262]. The roughness of the DIP layer defined from the fit of the Kiessig oscillations (Fig. 6.11) is $1.10 \pm 0.02$ nm. After dbSeQ was deposited, the roughness decreased to $0.44 \pm 0.01$ nm. We observe slight roughening of the film at 253 K, where the roughness of dbSeQ layer equals $0.91 \pm 0.02$ nm and as temperature reaches 273 K, we observe changes in contrast for the Kiessig fringes which indicate the change in coverage of the dbSeQ layer.

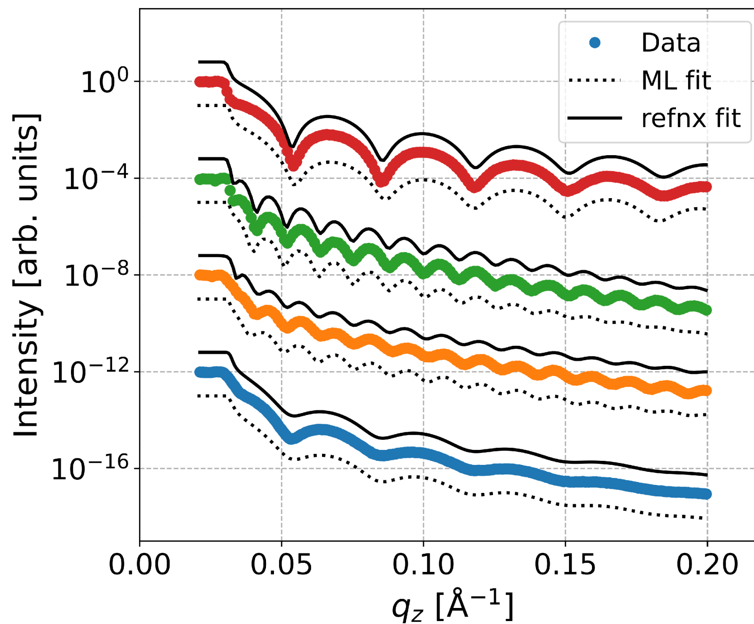


***Figure 6.11:*** *Fits of the XRR data for post-growth and subsequent annealing steps (253 and 313 K) for LT-grown bilayer dbSeQ/DIP film, utilizing* `refnx` *[206] and* `reflectorch (mlreflect 2.0)` *[207–209] packages. All curves are vertically offset for clarity.*

Starting from T = 253 K, the Bragg reflection at $q_z \approx 0.37$ $\mathring{A}^{-1}$ is visible and becomes more pronounced as the temperature increases, due to the reorientation of the DIP domains from $\lambda$ to $\sigma$- orientation. As temperature reaches 313 K, we observe the absence of the dbSeQ-related features, and the smoothening of DIP film, to the roughness of $0.20 \pm 0.01$ nm. We do not observe new Bragg peaks from the dbSeQ neither directly after its growth nor after the annealing.

Similarly to the XRR data, the GISAXS annealing patterns for the LT-grown film exhibit visible changes with each annealing step and the results are presented in Fig. 6.12. Due to the large correlation distances, the side peaks that are located along the intense central streak at $q_{xy} = 0$ are not observable in the post-growth scan in Fig. 6.12 (a). The pronounced modulations in the vertical direction along

$q_z = 0$ are visible and are related to the waveguide effect arising from the conformal roughness between the DIP and dbSeQ layers [170, 263, 264].

At T = 253 K (Fig. 6.12 (b)) we observe the shift of the side peaks towards larger $q_{xy} = 0$, which means a decrease in the correlation length, namely to $D_{\text{corr}} = 190 \pm 7$ nm. The width of the central streak increases as well as can be seen from Fig. 6.13.

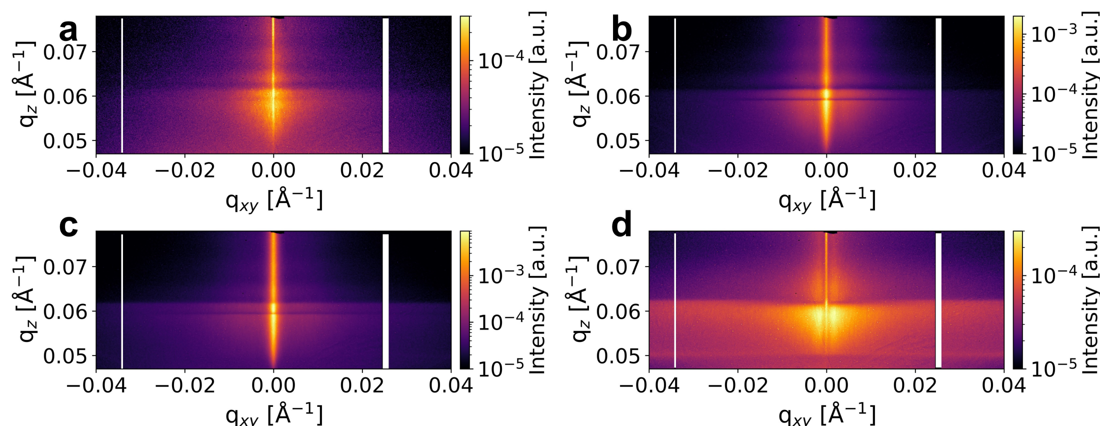


***Figure 6.12:*** *Averaged GISAXS images for every annealing step for the LT-grown bilayer dbSeQ/DIP film: 173 K (a), 253 K (b), 273 K (c), 313 K (d).*

At T = 273 K (Fig. 6.12 (c)) we observe an increase in the distance between the side peaks, indicating a decrease in the correlation length, namely, to $D_{\text{corr}} = 70 \pm 5$ nm. At T = 313 K (Fig. 6.12 (d)) we observe a completely different scattering pattern than for previous annealing steps. The horizontal line cut depicted in Fig. 6.13 shows the sudden shift of side peaks towards $q_{xy} = 0$, where the correlation length $D_{\text{corr}} = 246 \pm 4$ nm. This drastic increase in correlation length can be attributed to the desorption of the dbSeQ molecules, which in turn uncovers the DIP with higher correlation length. This indicates that changes in the film occur under the influence of temperature.

In summary, we explored the annealing kinetics of heterostructures incorporating dbSeQ and DIP and found that the bilayer dbSeQ/DIP film grown at RT is relatively stable under heat. Additionally, we found that the presence of a templating organic layer does not improve crystallinity of the overlayer, and we found that the dbSeQ layer increases the roughness of the bilayer film. GISAXS data showed that the scattering patterns are largely unchanged meaning that the film exhibits minor changes in correlation length during the annealing.

In the case of the co-deposited dbSeQ:DIP 1:1 film grown at RT we found the same scenario that applies for the analogous bilayer compound. The XRR data show the absence of dbSeQ-related features and the absence of changes in the XRR pattern during annealing, implying the stability of the co-deposited film. The GISAXS data show that the correlation length related to DIP does not change, and the correlation length of the dbSeQ islands increases beyond the experimental

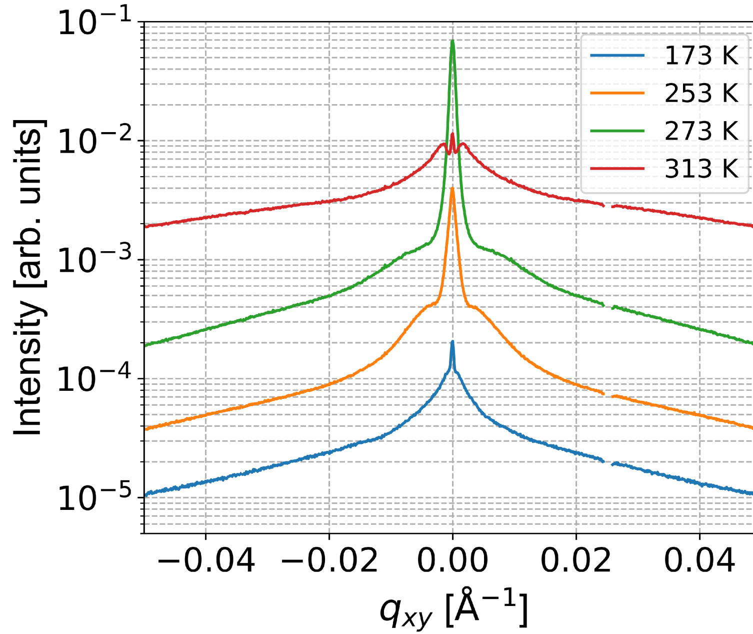


***Figure 6.13:*** *Horizontal line cuts taken from the averaged image from the post-growth and annealing scans for bilayer dbSeQ/DIP film grown at LT. Gaps at about* $q_{xy} = 0.023$ $\mathring{A}^{-1}$ *originate from the intermodular detector gap. All curves are vertically offset for clarity.*

resolution during annealing.

The growth of a bilayer dbSeQ/DIP film at LT, likewise the growth of neat dbSeQ at LT, is characterized by the formation of the film with extremely low roughness. We found that the film remains smooth until the substrate temperature increases to T = 273 K after which the roughness increases drastically. We attribute this finding to a strong dewetting that occurs after temperature reaches 273 K. Interestingly, that the layer of dbSeQ does not prevent the DIP from the reorientation to its $\sigma$-phase. GISAXS showed that the changes in the correlation length were present during each annealing step, meaning that the LT-grown dbSeQ film has limited thermal stability. We also found that at the last annealing step, the DIP layer is being uncovered by the dbSeQ overlayer because of dewetting. The resulting morphology after exposure of the film to RT is presented in the next section.

## 6.3 Ex situ morphology studies

The next step in the analysis of the thin films is studying the morphology *ex situ* to investigate the influence of post-growth processes. In order to achieve this, high-resolution microscopy (AFM and SEM) and X-ray reflectivity techniques were employed to obtain information in real-space and reciprocal-space. Initially, the discussion will cover bilayer and co-deposited dbSeQ thin films containing DIP.

The co-deposited and bilayer films incorporating PEN are additionally investigated by XRR. The morphology of neat DIP and PEN thin films is well known in the literature [265, 266], and the morphology of dbSeQ was described in detail in a previous chapter (Sec. 5.4).

### 6.3.1 Ex situ morphology studies of the heterostructures incorporating dbSeQ and DIP

The AFM data for the dbSeQ complexes that include DIP were obtained exclusively for films grown at RT.

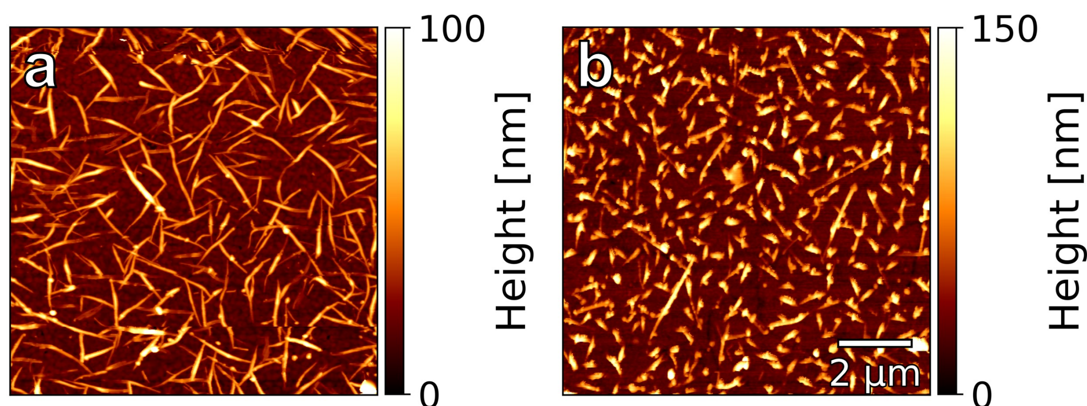


***Figure 6.14:*** *Real space AFM data: bilayer dbSeQ/DIP film grown at RT (a) and co-deposited dbSeQ:DIP 1:1 grown at RT (b).*

The AFM image of the bilayer dbSeQ/DIP film ($d_{\mathrm{dbSeQ}} = 8$ nm, $d_{\mathrm{DIP}} = 20$ nm) grown at RT is presented in Fig. 6.14 (a). The morphology of this bilayer film differs from the pristine dbSeQ film grown on the Si/SiO$_x$, where the bilayer film has more pronounced and homogeneous needle-like dbSeQ islands. The presence of needle-like islands of dbSeQ is observed, and the surface coverage is about 33%. The inter-island distance is $D_{\mathrm{ii}} = 530 \pm 12$ nm, while the correlation length from the GISAXS data is higher than the experimental resolution. We speculate that this is due to the overlapping of the needles of dbSeQ. The average length of the islands is $881 \pm 351$ nm, and the average width is $116 \pm 28$ nm. The average roundness of the islands equals $0.21 \pm 0.13$, indicating that the dbSeQ islands in the bilayer film are more elongated than the islands in neat dbSeQ film.

The morphology for a RT-grown co-deposited dbSeQ:DIP 1:1 film ($d_{\mathrm{dbSeQ}} = 17$ nm, $d_{\mathrm{DIP}} = 25$ nm) is presented in Fig. 6.14 (b). The average island length equals $549 \pm 316$ nm and the average width equals $165 \pm 35$ nm, with average roundness equal to $0.33 \pm 0.17$, while the surface coverage is about 36%. The average inter-island distance of dbSeQ $D_{\mathrm{ii}} = 556 \pm 15$ nm is in a good agreement with the correlation length extracted from GISAXS data that equals $D_{\mathrm{corr}} = 628 \pm 4$ nm.

The much smaller islands of dbSeQ in this case can be explained by the presence of DIP in the mixture.

Furthermore, the results of the SEM measurements are presented in Fig. 6.15. We observe the appearance of rectangular-shaped structures formed on the dbSeQ needles, which are not characteristic of dbSeQ or DIP.

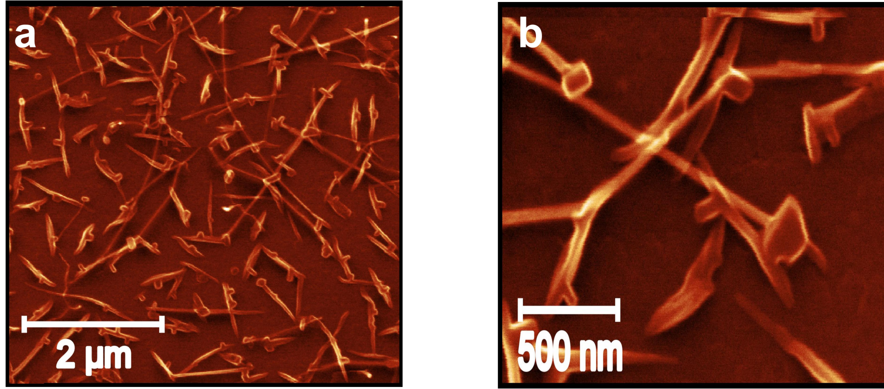


***Figure 6.15:*** *Real space SEM data for co-deposited dbSeQ:DIP 1:1 grown at RT: × 15000 magnification (a) and × 65000 magnification (b).*

The morphology data showed that DIP has a limited impact on the morphology of dbSeQ thin films. For the bilayer film, we observed needle-like islands of dbSeQ likewise for the neat dbSeQ film. Interestingly that the templating layer of DIP does not increase the surface coverage for dbSeQ. We observed that for the co-deposited film, both compounds tend to phase separate, which is evident from the DIP islands located between the dbSeQ islands. The average island size is smaller for the mixture than for the neat dbSeQ grown at RT, which can be attributed to the impact of DIP. The inter-island distance extracted from the AFM image is in good agreement with *in situ* GISAXS data.

## 6.3.2 Ex situ morphology studies of the heterostructures incorporating dbSeQ and PEN

The AFM image of the bilayer dbSeQ/PEN film ($d_{\mathrm{dbSeQ}} = 14$ nm, $d_{\mathrm{PEN}} = 16$ nm) grown at RT is presented in Fig. 6.16 (a). We see that similar to neat dbSeQ, the islands of dbSeQ have elongated needle-like form, but unlike bilayer dbSeQ/DIP film, the inter-island distances are larger. The surface coverage for dbSeQ islands is about 31%. The inter-island distance extracted from AFM is $D_{\mathrm{ii}} = 706 \pm 270$ nm, while the correlation length from the GISAXS data is $D_{\mathrm{corr}} = 731 \pm 11$ nm. In the gaps between the dbSeQ islands, the islands of PEN are observable. The distinguishing characteristic of this thin film is the substantial length of the dbSeQ islands, which can reach up to 2 $\mu$m. The average length of the islands is $1020 \pm 480$ nm, and the average width is $219 \pm 35$ nm. The average roundness of the islands equals $0.30 \pm 0.21$, indicating that the dbSeQ islands in the bilayer film

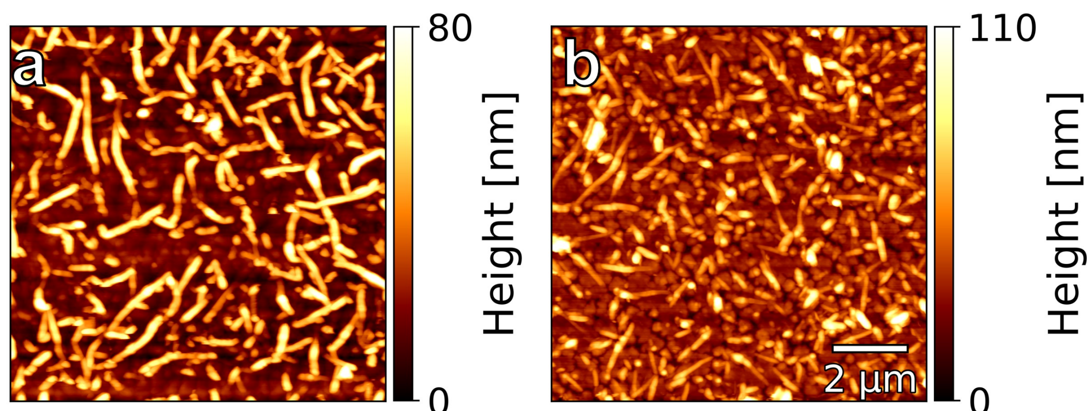


***Figure 6.16:*** *Real space AFM data: bilayer dbSeQ/PEN film grown at RT (a) and co-deposited dbSeQ:PEN 1:1 grown at RT (b).*

are slightly less elongated than the islands in neat dbSeQ and bilayer dbSeQ/DIP films.

The morphology for a RT-grown co-deposited dbSeQ:PEN 1:1 ($d_{\text{nom}}$(total) = 30 nm) film is presented in Fig. 6.16 (b). We observe that dbSeQ forms needle-like islands in a similar manner to the growth of pristine dbSeQ grown on Si/SiO$_x$ and PEN forms wedding-cake-shaped islands between dbSeQ islands. The average island length equals $661 \pm 314$ nm and the average width equals $180 \pm 37$ nm, with average roundness equal to $0.33 \pm 0.17$, while the surface coverage is about 32%. The average inter-island distance of dbSeQ $D_{\text{ii}} = 476 \pm 190$ nm is in a good agreement with the correlation length extracted from GISAXS data that equals $D_{\text{corr}} = 456 \pm 5$ nm. An additional topology image is presented in Fig. 6.17

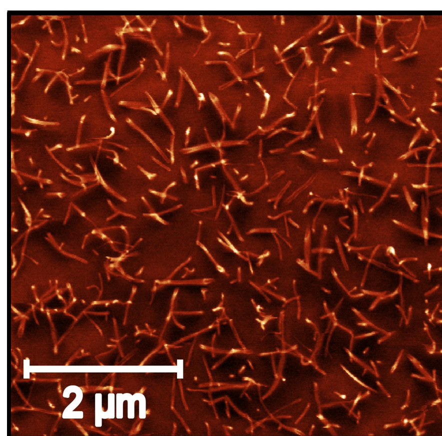


***Figure 6.17:*** *Real space SEM data for co-deposited dbSeQ:PEN 1:1 grown at RT.*

confirms the smaller needle-shaped islands of dbSeQ oriented randomly on the substrate. We found that likewise for the co-deposited dbSeQ:DIP 1:1 film, islands of dbSeQ are smaller than for the neat dbSeQ film. We attribute this finding to

the presence of PEN in the mixture.

The *ex situ* XRR scans for the aforementioned films are presented in Fig. 6.18. For the bilayer dbSeQ/PEN film only PEN-related features are visible, including two Bragg peaks that emerge at $q_z = 0.4$ Å$^{-1}$ and $q_z = 0.8$ Å$^{-1}$. Similar to bilayer films with DIP, no Bragg peaks corresponding to the novel structures are present.

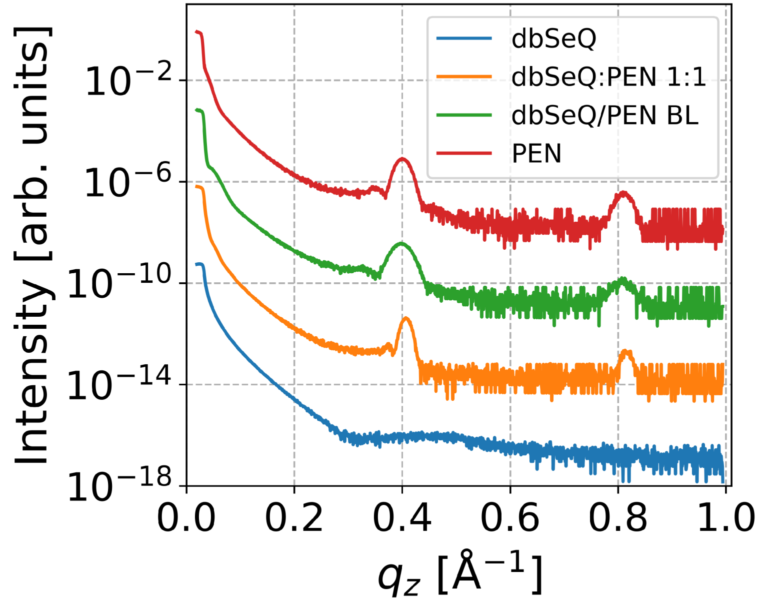


***Figure 6.18:*** *Ex situ XRR scans of neat dbSeQ, neat PEN, bilayer dbSeQ/PEN and co-deposited dbSeQ:PEN 1:1 films grown at RT. All curves are vertically offset for clarity.*

XRR scans for the co-deposited dbSeQ:PEN 1:1 film reveal two PEN-related Bragg peaks at $q_z = 0.4$ Å$^{-1}$ and $q_z = 0.8$ Å$^{-1}$. Similarly to the bilayer film, we observe no new features related to mixed phase.

In conclusion, we found that how PEN influences dbSeQ in the RT-grown heterostructures that incorporate both compounds. For the bilayer film, we observed large islands of dbSeQ, in the $\mu$m range which characterizes by the large inter-island distances which are in a good agreement with GISAXS data. The roundness of the dbSeQ islands is slightly higher than for the neat dbSeQ film. The XRR data for the dbSeQ/PEN bilayer film showed no new peaks characteristic for the new phase of dbSeQ on the PEN. For the co-deposited dbSeQ:PEN 1:1 film, it is evident that both compounds exhibit a phase separation scenario. The real-space morphology showed the needle-like dbSeQ islands along the islands of PEN. A good correlation between GISAXS and AFM data was found for the co-deposited film.

## 6.4 Crystalline structure of the films

In order to achieve a more complete understanding of the in-plane and out-of-plane structures of mixed and bilayer films, a series of GIWAXS experiments were conducted. In this section, we present *ex situ* GIWAXS data for films grown at RT. Initially, the discussion will cover bilayer and co-deposited dbSeQ thin films containing DIP, and then heterostructures incorporating dbSeQ and PEN. The GIWAXS data for neat DIP and PEN thin films is well known in the literature [199, 267], and the GIWAXS results of dbSeQ were described in detail in a previous chapter (Sec. 5.5).

### 6.4.1 Crystalline structure of the heterostructures incorporating dbSeQ and DIP

GIWAXS data for the bilayer dbSeQ/DIP film grown at RT are presented in Fig. 6.19 (a). As it was stated in Sec. 5.5, dbSeQ at RT grows with randomly oriented domains, so thin films of dbSeQ grown at RT show the Debye-Scherrer rings at $q = 0.50,\ 0.79,\ 0.85,\ 1.00,\ 1.34$ Å$^{-1}$ with the maximum of intensity aligned along $q_z$ and rings at $q = 1.69$ $2.03,\ 2.26$ Å$^{-1}$ with the maximum of intensity aligned along $q_{xy}$. The measured pattern for the bilayer film reveal the presence of pronounced intensity peaks, which are predominantly attributed to DIP (truncation rods at $q_{xy} = 1.17$ and $1.48$ Å$^{-1}$ and a bright peak at $q_{xy} = 0,\ q_z = 0.37$ Å$^{-1}$). All these peaks belong to the $\sigma$-phase of the DIP [199], while the weak Debye-Scherrer rings ($q = 0.50,\ 0.85$ and $1.05$ Å$^{-1}$) are related to dbSeQ. The absence of new features in GIWAXS data indicates the weak influence of DIP on dbSeQ.

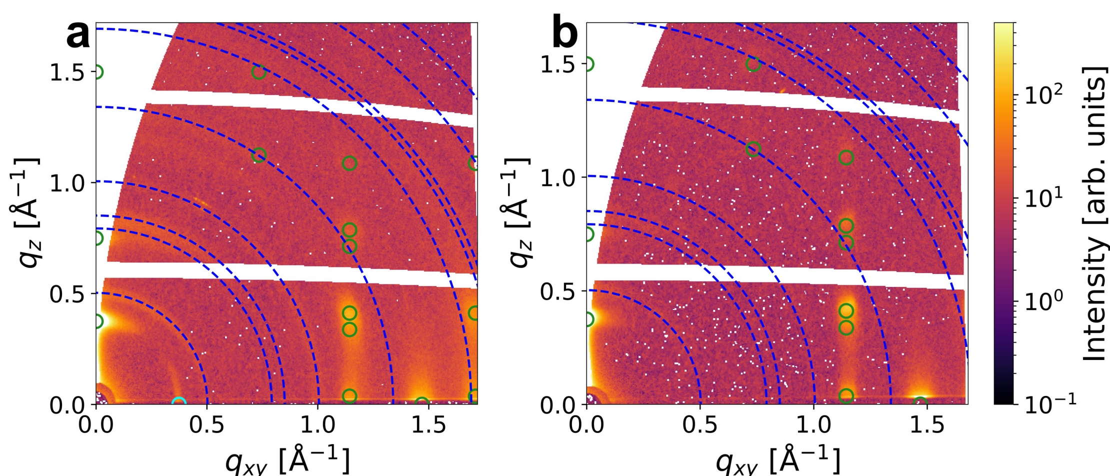


***Figure 6.19:*** *GIWAXS data for: Bilayer film of dbSeQ/DIP grown at RT (a). Co-deposited film of dbSeQ:DIP 1:1 (b). Blue dashed circles indicate peaks from dbSeQ, green ($\sigma$-phase with preferred [001] orientation) and cyan ($\lambda$-phase with preferred [100] orientation) circles indicate peaks from DIP.*

The results obtained for the co-deposited dbSeQ:DIP 1:1 film confirm previous suggestions about the phase separation during the co-deposition. In Fig. 6.19 (b) we observe intense peaks of DIP (truncation rods at $q_{xy} = 1.17,\ 1.48,\ 1.71$ Å$^{-1}$ and two peaks at $q_{xy} = 0,\ q_z = 0.37$ Å$^{-1}$ and $q_{xy} = 0,\ q_z = 0.72$ Å$^{-1}$) and weak Debye-Scherrer rings related to dbSeQ ($q = 0.50, 0.85$ and 1.05 Å$^{-1}$). We observe the absence of new features indicative of a new mixed crystalline structure or enhanced long-range order in the co-deposited film; however, there is a peak at $q_{xy} = 0.37$ Å$^{-1}$, $q_z = 0$ which corresponds to $\lambda$-phase of DIP, indicating the partial reorientation of DIP molecules due to the presence of dbSeQ. This confirms our previous suggestion that the co-deposited dbSeQ:DIP films undergo phase separation of both components.

In summary, the GIWAXS data for bilayer dbSeQ/DIP film confirmed our previous suggestions about the limited impact of the templating layer on the overlayer of dbSeQ. GIWAXS data for the co-deposited dbSeQ:DIP 1:1 film, confirmed our previous hypothesis regarding the phase separation in such complexes. Interestingly, we observed the signal attributed to the $\lambda$-phase of DIP in thin films, indicating the influence of dbSeQ on the orientation of the DIP molecules in the co-deposited film at RT.

### 6.4.2 Crystalline structures of the heterostructures incorporating dbSeQ and PEN

GIWAXS data for the bilayer dbSeQ/PEN film grown at RT are presented in Fig. 6.20 (a). Similarly to bilayer films of dbSeQ with DIP, we do not observe new features characteristic for a new orientation of dbSeQ. We see that the two pronounced and elongated Bragg peaks related to PEN at $q_{xy} = 1.35$ and 1.65 Å$^{-1}$ and two high-intensity peaks in the region above $q_z = 0.30$ Å$^{-1}$ belong to the $\sigma$-orientation of the PEN [199]. The weak Debye-Scherrer rings around $q_{xy} = 0.50,\ 0.85$ and 1.00 Å$^{-1}$ are similar to those of RT-grown dbSeQ on the Si/SiO$_x$ substrate. The absence of new features in GIWAXS data indicates the weak influence of the PEN layer on dbSeQ.

Before discussing GIWAXS patterns of mixed films dbSeQ:PEN, it is important to note that PEN growth at RT on a Si/SiO$_x$ substrate is characterized by multiple phases dependent on the thickness of the thin film [80]. The elongated peaks at $q_{xy} = 1.35$ and 1.65 Å$^{-1}$ and the peaks at $q_z = 0.40$ and 0.80 Å$^{-1}$ are in complete correspondence with the previously performed data for the $\sigma$-orientation of PEN molecules in thin films grown at RT [199]. The weak Debye-Scherrer rings around $q_{xy} = 0.50,\ 0.85$ and 1.00 Å$^{-1}$ are similar to those of RT-grown dbSeQ on the Si/SiO$_x$ substrate. For the co-deposited dbSeQ:PEN 1:1 film there are no new diffraction peaks indicative of a new mixed crystalline structures. However, we observe an intense peak at $q_{xy} = 0.16,\ q_z = 0.42$ Å$^{-1}$ that corresponds to the tilted by 21° Holmes bulk phase of PEN [268]. We attribute the appearance of this phase of PEN to the influence of dbSeQ in the mixture.

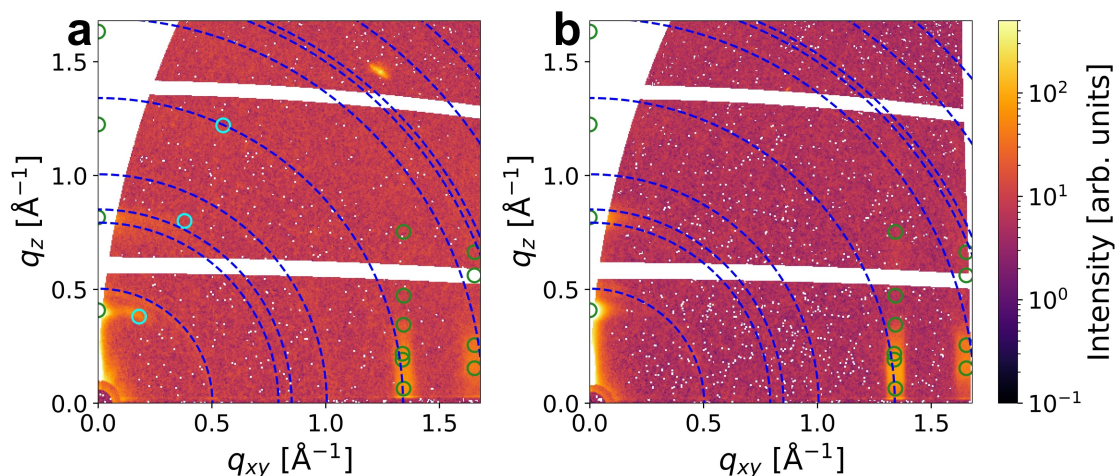


***Figure 6.20:*** *GIWAXS data for: Bilayer film of dbSeQ/PEN grown at RT (a). Co-deposited film of dbSeQ:PEN 1:1 (b). Blue dashed circles indicate peaks from dbSeQ, green ($\sigma$-phase with preferred [001] orientation) and cyan ($\lambda$-phase with preferred [001] orientation) circles indicate peaks from PEN.*

In summary, the GIWAXS data for the heterostructures with dbSeQ and PEN showed results quite similar to those of the heterostructures that incorporate dbSeQ and DIP. For the bilayer dbSeQ/DIP film, we confirmed our previous suggestions about the limited impact of the templating layer on the overlayer of dbSeQ. GIWAXS data for the co-deposited dbSeQ:PEN 1:1 film confirmed our previous hypothesis regarding the phase separation in such complexes. However, we observed the signal attributed to the bulk-phase of PEN in thin films, indicating the influence of dbSeQ on the orientation of the PEN molecules in the co-deposited film at RT. These findings are consistent with the results obtained previously from the AFM and XRR analysis.

## 6.5 Optical Properties

For the optical characterization of the thin films, we employed transmission absorption spectroscopy in the UV-Vis range. This technique is non-invasive and allows us to obtain relatively quick information on absorption spectra of the thin film. The optical characterization of neat DIP and PEN thin films is well known in the literature [86, 128, 266, 269], and the optical data of dbSeQ were described in detail in Sec. 5.6. Initially, the discussion will cover bilayer and co-deposited dbSeQ thin films containing DIP, and then bilayer and mixed dbSeQ films incorporating PEN. The optical characterization of all films was performed *ex situ*.

### 6.5.1 Optical characterization of the heterostructures incorporating dbSeQ and DIP

The absorption spectrum of the bilayer dbSeQ/DIP film in Fig. 6.21 demonstrates minor (0.02-0.05 eV) discrepancies in peak position compared to the absorption of the neat DIP film. As expected, we see no changes in spectra for the bilayer film compared to the neat compounds, all of the features arising from the superposition of the dbSeQ and DIP absorption curves. The dbSeQ-related peaks (2.50, 2.85, 3.17, 3.90 and 4.89 eV) in the bilayer film are practically invisible because of the much greater absorption of DIP in the UV-Vis range and there are no new peaks emerge.

As previously outlined, the dbSeQ spectrum exhibits three prominent peaks in the region preceding 3.25 eV. These peaks include a high-intensity peak at 2.85 eV

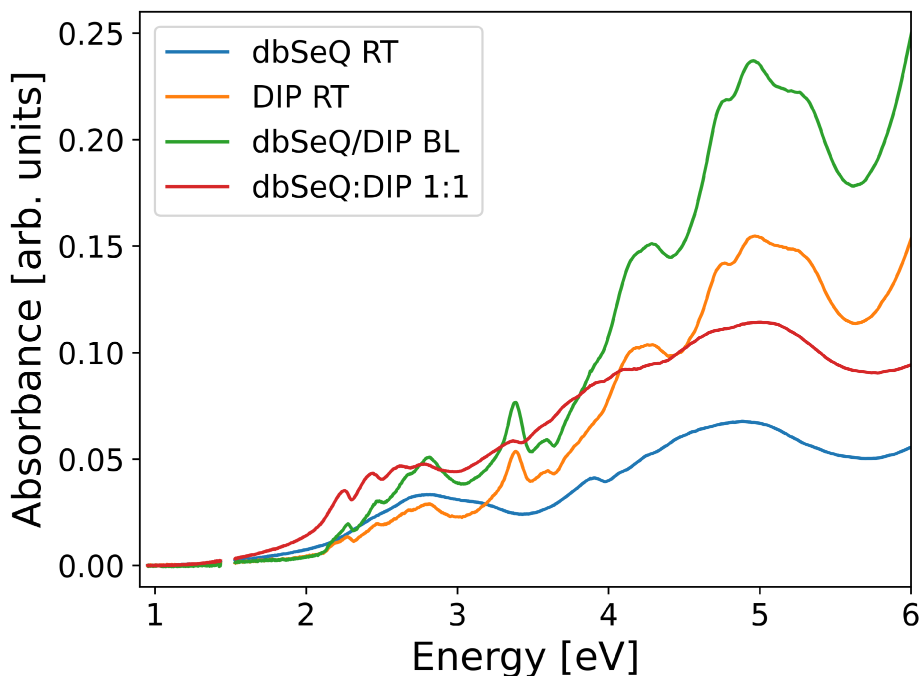


***Figure 6.21:*** *Optical absorption spectra in UV-Vis region for the various thin films incorporating dbSeQ and DIP, normalized to the film thickness. Gaps at about 1.5 eV originate from the switch of the detector.*

and two low-intensity peaks at 2.50 eV and 3.17 eV, respectively. In the same range, DIP exhibits weak peaks at 2.21, 2.38, and 2.58 eV. According to Nichols et al. [269], these peaks correspond to a vibronic progression. There is also a peak at 2.81 eV. This is in full agreement with previous works, such as Duva et al. [270]. The absorption spectrum of the co-deposited dbSeQ:DIP 1:1 film shows an indication of the $\lambda$-phase of DIP in co-deposited film. This is evident from the different relative intensity of the low-energy peaks (2.27, 2.47, 2.67 and 2.80 eV)

compared to the RT-grown DIP film [199]. It confirms that the dbSeQ in the mixture influences the orientation of DIP unit cells, as was shown by GIWAXS before. Furthermore, presence of dbSeQ in the mixture causes a decline in the intensity of the peaks above 3 eV, compared to neat DIP, which can also be attributed to the influence of dbSeQ.

In summary, the UV-Vis data for bilayer dbSeQ/DIP film confirmed our previous suggestions about the limited impact of the templating layer on the overlayer of dbSeQ. UV-Vis data for the co-deposited dbSeQ:DIP 1:1 film showed that the majority of the absorption peaks arise from the superposition of neat compounds, which confirms our previous hypothesis regarding the phase separation in such complexes. We found another confirmation of the presence of the $\lambda$-phase of DIP in thin films, indicating the influence of dbSeQ on the orientation of the DIP molecules in the co-deposited film at RT.

### 6.5.2 Optical characterization of the heterostructures incorporating dbSeQ and PEN

The absorption spectrum of the bilayer dbSeQ/PEN film in Fig. 6.22 demonstrates minor discrepancies in the peak position compared to the absorption of neat PEN film. We observe the presence of high-intensity PEN-related peaks between 1.6 and 2.5 eV, namely at 1.83, 1.94, 2.09, and 2.25 eV. In PEN molecules, the TDM is oriented along the short molecular axis, resulting in amplified absorption in the transmission geometry for RT-grown films containing PEN. Similarly to the bilayer dbSeQ/DIP film, we observe no changes in spectra for the bilayer film compared to the neat compounds, all of the features arising from the superposition of the dbSeQ and PEN absorption curves. In the region between 2.3 and 3.2 eV, where PEN does not have significant absorption features, we observe pronounced dbSeQ-related absorption peaks. In the high-energy range the broad peaks of PEN at 4.3 and 5.1 eV are observed. It is evident that no new peak emerges, indicating a negligible influence of the PEN layer on the absorption spectrum of the bilayer film.

The absorption spectrum of the co-deposited dbSeQ:PEN 1:1 film shows an indication of the different polymorphs of PEN in co-deposited film, which is evident from a change in relative peak intensities for peaks in the energy range of 1.5 – 2.6 eV [271]. We attribute this observation to the influence of dbSeQ on PEN in the co-deposited film, as was shown by GIWAXS data before.

In summary, we observe that the RT-grown films incorporating dbSeQ and PEN do not show the new absorption features compared to pure compounds. This serves as additional evidence that the film structure did not change as a result of the change in the deposition surface. There is no evidence of charge transfer or intermixing in absorption spectra for co-deposited films with PEN as well as for bilayer films with PEN. In the analogous manner to co-deposited dbSeQ:DIP 1:1 film we observe the presence of different phase of PEN in the co-deposited

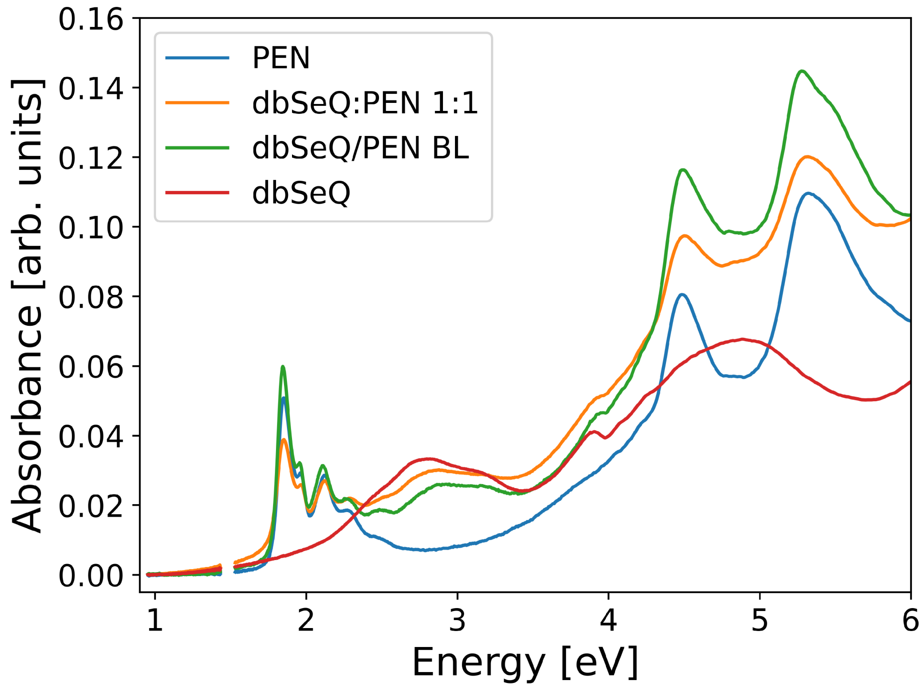


***Figure 6.22:*** *Optical absorption spectra in UV-Vis region for the various thin films incorporating dbSeQ and PEN, normalized to the film thickness. Gaps at about 1.5 eV originate from the switch of the detector.*

dbSeQ:PEN 1:1 film which we attribute to the influence of dbSeQ on PEN.

## 6.6 Summary and conclusion

In this section, we offer a comprehensive summary of the results obtained in this chapter, thereby facilitating the drawing of the most profound conclusions about co-deposited and bilayer dbSeQ films with DIP and PEN grown at different substrate temperatures. Initially, the discussion will cover co-deposited and bilayer dbSeQ thin films containing DIP, and then co-deposited and bilayer dbSeQ films incorporating PEN.

### 6.6.1 Summary and conclusion on films with DIP

The growth of dbSeQ on top of a DIP film at RT results in large, rough, needle-like islands of dbSeQ with a correlation length exceeding the experimental resolution. Compared to a neat dbSeQ film, the crystallites of dbSeQ grown on DIP are more elongated. From the AFM data, we found that the correlation length is so large because of the overlap of the islands of dbSeQ. From the AFM data we found out the correlation length is so high because of the overlap of the islands of dbSeQ. Additional characterization by XRR, GIWAXS, and absorbance spectroscopy did

not show signs of a different crystalline and electronic structures. The results indicated that the morphology of the bilayer films was influenced by the underlying layer; however, no significant changes in the crystallinity or the new phase of the dbSeQ layer were observed for the RT-grown bilayer films with DIP as a bottom layer. Optical characterization confirmed the absence of distinctive features due to the bilayer architecture, supporting the conclusion of negligible structural changes induced by the planar heterojunction. Annealing to 333 K showed that the bilayer films remained stable; the growth and annealing schema of RT-grown bilayer dbSeQ/DIP film is presented in Fig. 6.23.

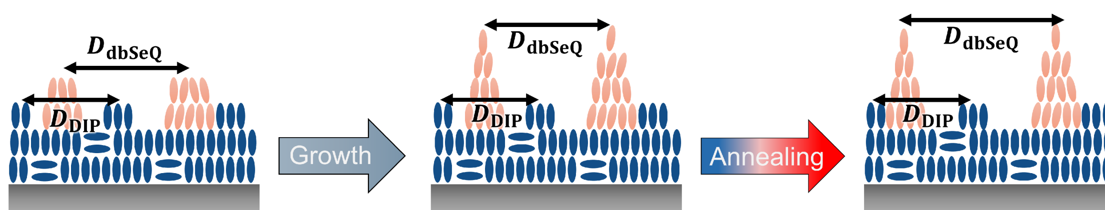


***Figure 6.23:*** *Schematic representation of growth and annealing behavior of RT-grown bilayer dbSeQ/DIP film.* $D_{dbSeQ}$, $D_{DIP}$ *stand for correlation lengths of dbSeQ and DIP, respectively.*

The growth of dbSeQ on top of the DIP film at LT is characterized by the inheritance of the correlation length of the DIP by dbSeQ at the beginning of the deposition and a subsequent, fast increase of the correlation length beyond the resolution limit of the experiment. Similarly to the growth of neat dbSeQ at LT, we observe continuous layer growth for the bilayer film. The analysis of post-growth and annealing data reveals that the layer of dbSeQ on DIP has a low roughness that remains stable until annealing to 273 K. After this temperature, we observed only DIP-related scattering features as a result of the strong dewetting of the dbSeQ film. We assume that the dbSeQ layer desorbs from the film, leaving only the DIP layer. Notably, the dbSeQ layer does not prevent DIP from the bottom layer from reorientation to its $\sigma$-phase during annealing of the film to RT. The growth and annealing schema of RT-grown bilayer dbSeQ/DIP film is presented in Fig. 6.24.

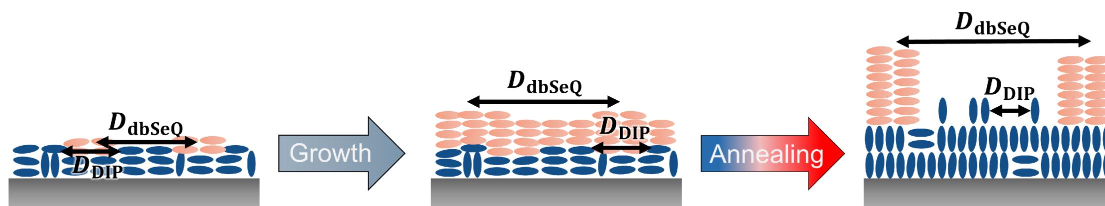


***Figure 6.24:*** *Schematic representation of growth and annealing behavior of LT-grown bilayer dbSeQ/DIP film.* $D_{dbSeQ}$, $D_{DIP}$ *stand for correlation lengths of dbSeQ and DIP, respectively.*

Analysis of the growth of co-evaporated dbSeQ:DIP 1:1 film at RT reveals a clear phase separation of the two compounds after the completion of the first monolayer. The GISAXS measurements showed two distinct in-plane correlation lengths, which belong to each of the deposited materials. We speculate that dbSeQ and DIP are mixing in the beginning of the deposition when the monolayer of DIP is formed. In the co-deposited film, the morphology has not shown significant changes compared to that of the neat compounds. However, the dbSeQ islands in the co-deposited film are shorter and exhibit a more circular shape in comparison to those observed in the neat dbSeQ film at RT. We found that the inter-island distances for dbSeQ in co-deposited film are smaller compared to the growth of neat dbSeQ at RT. Interestingly, the presence of dbSeQ in the co-deposited allows DIP to form only one closed monolayer, instead of 3-5 monolayers, as was previously found for neat DIP film. The subsequent annealing showed the increase in the correlation length for the dbSeQ islands, indicating low impact of DIP on the thermal stability of co-deposited film. Additionally, we observe the presence of the $\lambda$-phase of DIP molecules in the co-deposited film, which can also be attributed to the influence of dbSeQ. In the absorption spectrum, we observed peaks that can be described by superposition of the individual components, confirming our suggestion about the phase separation. The growth and annealing schema of RT-grown bilayer dbSeQ/DIP film is presented in Fig. 6.25.

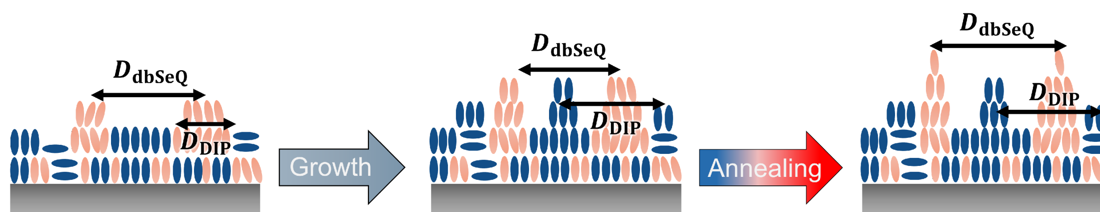


***Figure 6.25:*** *Schematic representation of growth and annealing behavior of RT-grown co-deposited dbSeQ:DIP 1:1 film. $D_{dbSeQ}$, $D_{DIP}$ stand for correlation lengths of dbSeQ and DIP, respectively.*

## 6.6.2 Summary and conclusion on films with PEN

For the growth of dbSeQ on PEN film at RT, we observe the same growth behavior as for the bilayer dbSeQ/DIP film, where the correlation length of dbSeQ is large and rapidly exceeds the experimental resolution. From the AFM data, we observe the large overlapping islands of dbSeQ. We do not observe the influence of the PEN layer on the optical or structural properties of dbSeQ. Optical characterization confirmed the absence of the templating effect that is evident from the absence of new signals in the UV-Vis spectrum. We have not observed the distinct in-plane correlation length scales in GISAXS experiments due to the rough nature of both components and length scales beyond the resolution of the experimental setup, as presented in Fig. 6.26.

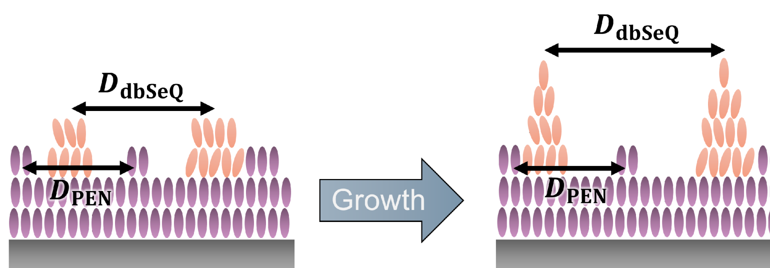


***Figure 6.26:*** *Schematic representation of growth and annealing behavior of bilayer dbSeQ/PEN film at RT.* $D_{dbSeQ}$, $D_{PEN}$ *stand for correlation lengths of dbSeQ and PEN, respectively.*

The growth of the co-deposited dbSeQ:PEN 1:1 film at RT is characterized by large inter-island distances beyond the experimental resolution for both compounds. We observe a growth pattern that resembles the one for co-deposited dbSeQ:DIP 1:1 film. We assume that, likewise the co-deposited film with DIP, the co-deposited film with PEN exhibits phase-separation from the beginning of the deposition but cannot prove it due to the fact that we have not observed the distinct in-plane correlation length scales in GISAXS experiments. From absorption spectroscopy,

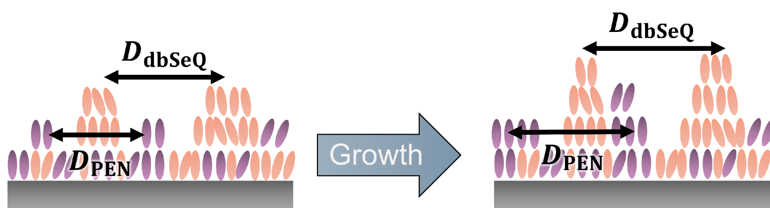


***Figure 6.27:*** *Schematic representation of growth and annealing behavior of co-deposited RT-grown dbSeQ:DIP 1:1 film.* $D_{dbSeQ}$, $D_{PEN}$ *stand for correlation lengths of dbSeQ and PEN, respectively.*

we found that for the co-deposited film a different PEN phase appeared. In addition, optical measurements proved our initial suggestions about the clear phase separation for RT grown films, which was proved by the absence of the new peaks in the UV-Vis spectrum. Morphology studies did not show significant changes in morphology compared to neat compounds. The growth and annealing schema of the film is presented in Fig. 6.27.

We demonstrate the growth behavior of the dbSeQ in various heterostructures and how it can be influenced by the substrate temperature. Our results provide crucial insight into the understanding of growth mechanisms in donor-acceptor blends, which could be used for the development of device architectures.

# Part IV

# Conclusions and outlook

**Chapter 7**

# Conclusions

This thesis provides insights into the growth and annealing behavior of thin films of $\pi$-conjugated molecules of selenadiazole. We prepared and analyzed a variety of thin films under different growth conditions, both *ex situ* and *in situ* to characterize growth and reveal post-growth effects. We also have grown various heterojunctions of dbSeQ with donor semiconductor molecules diindenoperylene and pentacene in BHJ and PHJ. The real-time experiments helped us to observe the morphology evolution during film deposition and allowed us to make some suggestions about growth behavior. Optical characterization served as an additional instrument for obtaining information on the electronic structure of neat and co-deposited compounds.

It was found that dbSeQ on Si/$SiO_x$ at RT grows in the form of rough, randomly oriented, needle-shaped, long crystallites. The correlation distances obtained by GISAXS and AFM are in the sub-$\mu$m range. dbSeQ crystallizes predominantly in the $\sigma$-phase, where the molecules are standing with a tilted edge-on configuration. The absorption spectrum in the UV-Vis range exhibits five distinct peaks and resembles the one measured in solution.

Conversely, the growth of dbSeQ at LT is characterized by significantly smaller correlation lengths and lower roughness, compared to the RT-grown film, which we attribute to the change in the molecular orientation of dbSeQ. It was observed that the low thermal stability of the LT-grown dbSeQ films resulted in strong dewetting during their annealing to RT. This, in turn, resulted in high roughness of the resulting film. The resulting islands are generally smaller and more circular than that observed for the RT-grown film. From the GIWAXS results, it is evident that the crystallites are oriented in the $\lambda$-phase in contrast to the $\sigma$-phase formed during growth at RT. This change in the molecular orientation leads to alterations in the absorption spectrum, resulting in a variation in the relative intensity of the peaks, as was previously found for different organic films grown at RT and LT.[199]

The growth of dbSeQ on top of a DIP film at RT results in large, rough, needle-like islands of dbSeQ with a correlation length exceeding the experimental resolution. Compared to a neat dbSeQ film, the crystallites of dbSeQ grown on DIP are more elongated. From the AFM data, we found that the correlation length is so large because of the overlap of the islands of dbSeQ. Additional characterization by XRR, GIWAXS, and absorbance spectroscopy did not show signs of a different crystalline nor electronic structure.

The growth of dbSeQ on top of the DIP film at LT has several differences

compared to the growth of neat dbSeQ. At the beginning, the correlation length of dbSeQ is equal to that of DIP, which means that dbSeQ grows in the gaps between DIP islands. After the initial stage, a subsequent fast increase in the correlation length beyond the resolution limit of the experiment is observed. Notably, the decay of the correlation length of dbSeQ in the bilayer is almost five times slower than that for the neat compound. From the XRR it is evident that the layer of dbSeQ on DIP has a low roughness that remains stable until annealing to 273 K. Above this temperature, we observed only DIP-related scattering features as a result of the strong dewetting of the dbSeQ film. Interestingly, the dbSeQ layer does not prevent DIP from the bottom layer from reorientation to its $\sigma$-phase during annealing of the film to RT.

The growth of co-evaporated dbSeQ:DIP 1:1 film at RT is characterized by mixing of both compounds in the first monolayer. After the first layer is closed, a phase separation growth scenario occurs. In the co-deposited film, the dbSeQ islands are smaller and exhibit more circular shape in comparison to those observed in the neat dbSeQ film at RT. We found that the inter-island distances for dbSeQ in the co-deposited film are smaller compared to the growth of neat dbSeQ at RT. Interestingly, the presence of dbSeQ in the co-deposited film allows DIP to form only one closed monolayer, instead of 3-5 monolayers, as was previously found for neat DIP. Sterical competition of the islands of both compounds results in smaller dbSeQ islands compared to those of neat dbSeQ. Additionally, we observe the presence of the $\lambda$-phase of DIP in the co-deposited film which can be also attributed to the influence of dbSeQ.

For the growth of dbSeQ on PEN at RT, we observe the same growth behavior as for the dbSeQ growth on DIP. The correlation length of dbSeQ is large and rapidly exceeds the experimental resolution. From the AFM data, we observe large overlapping islands of dbSeQ. The PEN layer has virtually no impact on the optical or structural properties of dbSeQ.

Co-deposited dbSeQ:PEN 1:1 films at RT exhibit is characterized by large inter-island distances in the sub-$\mu$m range for both compounds. We observe a growth pattern that resembles that of the co-deposited dbSeQ:DIP 1:1 film. We speculated that, likewise to the co-deposited film with DIP, the co-deposited film with PEN exhibits a phase-separation growth scenario. From absorption spectroscopy and GIWAXS, we found that for the co-deposited film a tilted Holmes bulk phase of PEN appeared.

We studied the growth behavior of dbSeQ in various heterostructures and how it can be influenced by the substrate temperature. The general trend for the growth of neat and bilayer films at RT is the formation of rod-shaped islands of dbSeQ, with inter-island distances in the sub-$\mu$m range. Neat and bilayer films deposited at LT exhibit low roughness and a correlation length of $\sim 60$ nm, which is of the order of magnitude smaller than for RT-growth. The annealing of these films to RT leads to strong dewetting. Simultaneous deposition of dbSeQ and DIP at RT leads to a clear phase separation, but for the co-deposited film with DIP mixing occurs in the first monolayer. The islands of dbSeQ are generally smaller in the

co-deposited films than those of neat dbSeQ, because of the sterical competition of the islands of both compounds. Additionally, it was found that the presence of dbSeQ in co-deposited films leads to the appearance of a different phase of the second compound. Our results provide crucial insight into the understanding of growth mechanisms in donor-acceptor blends. We expect that the growth scenarios for dbSeQ in combination with DIP and PEN can be transferred to other rod-shaped OSCs. The search for other binary mixtures that can enhance the thermal stability and structural order of films with dbSeQ is underway.

## Chapter 8

# Outlook

This thesis provides valuable information on the structure and growth behavior of dbSeQ and its blends with DIP and PEN, while raising several questions for future research and leaving room for improvement.

- We found that at LT, dbSeQ forms a smooth film. However, the question about the crystallinity of the film is still open. Additional *in situ* real-time XRR and GIWAXS studies for the LT-grown film could track the roughness evolution and answer the question of whether the film is crystalline or amorphous? If it is crystalline, how does annealing change its crystalline structure?

- Our growth studies would be helpful in tailoring the length scales according to the needs. The important direction for future research would be the development of encapsulation techniques to prevent LT-grown dbSeQ from annealing effects.

- Another idea is to create a PHJ with DIP or PEN at LT, but to use dbSeQ as a templating layer. We assume that it could increase the thermal stability of the dbSeQ film and weaken the dewetting.

- The growth of the thin film on strongly-interacting substrates such as metals or on the oriented mica could improve the crystallinity of dbSeQ and might change the orientation of the unit cell of dbSeQ.

- We have shown that both co-deposited films with dbSeQ exhibited phase separation, meaning that dbSeQ has the potential to be implemented as a spacer material to tailor the length scales of other materials in the co-deposited films.

- More detailed XRR studies during annealing of the LT-grown neat dbSeQ film would allow us to define the exact temperature at which desorption occurs. In contrast, the growth of neat dbSeQ at other substrate temperatures between 173 and 273 K would answer the question at which temperature dbSeQ change orientation on the substrate.

# Part V

# Appendices

Chapter 9

# Appendix

This chapter presents supplementary data for the results discussed in Chap. 5, focusing on the characterization of dbSeQ films. The additional data includes AFM/SEM images and fitting procedures for the AFM and GISAXS data.

## 9.1 Additional morphology investigations

In order to compare the morphologies of the dbSeQ thin films with known materials, we deposited thin films of DIP and PEN, where both films have a nominal thickness of 3 nm. The resulting images are presented in Fig. 9.1. We observe that the islands of PEN and DIP are more uniform than those for dbSeQ. The surface coverage for both films (∼83 % and ∼57 % for DIP and PEN, respectively) is significantly larger compared to the films of dbSeQ with comparable or higher thicknesses.

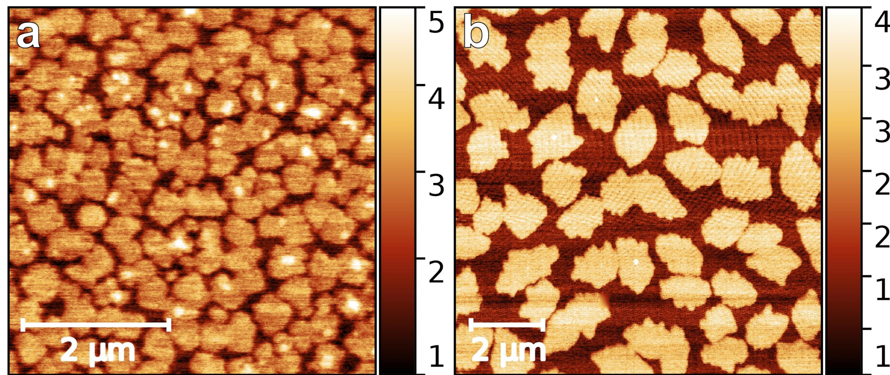


***Figure 9.1:*** *AFM images of thin films with a nominal thickness of 3 nm grown at RT: DIP (a), PEN (b). The height scale is given in nm.*

In Fig. 9.2 we present an example of analysis of HHCF from the raw AFM image (Fig. 9.2 (a)). As a first step, we employed grain detection procedures using the watershed algorithm (red mask in Fig. 9.2 (b)). It allows us to extract the height-height correlation function (HHCF) with in-built functions in the Gwyddion software. After extraction, we are able to fit it with a Gaussian function: $f(x) = 2\sigma^2[1 - \exp(-(x/\xi)^2)]$, where $\sigma$ and $\xi$ are the roughness and correlation length, respectively. The fit result is depicted in Fig. 9.2 (c).

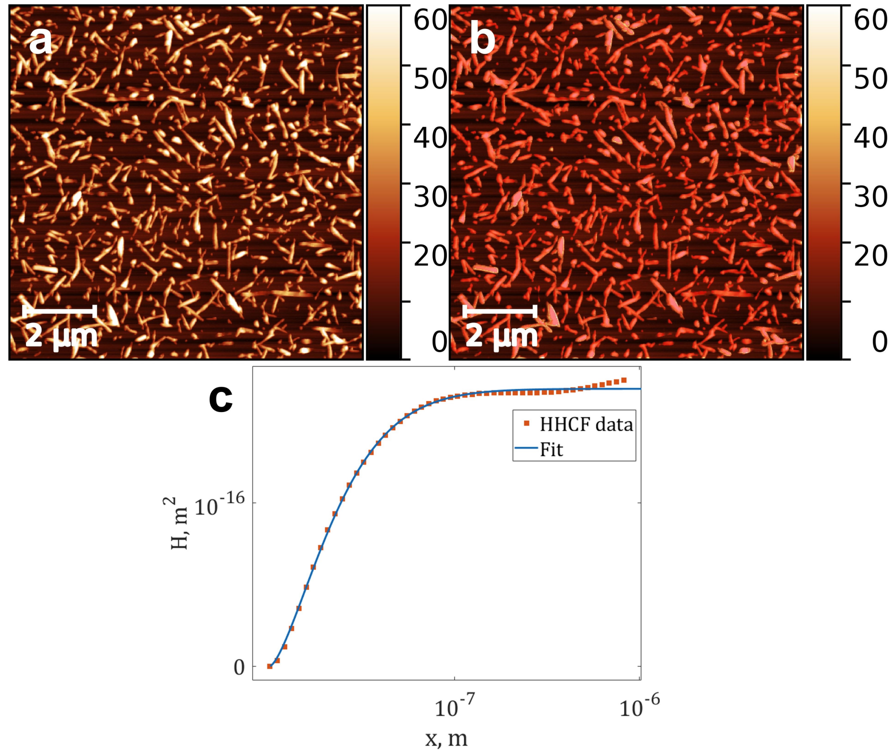


***Figure 9.2:*** *AFM scan of dbSeQ thin film with a nominal thickness of 12 nm grown on Si/SiO$_x$ (a). Example of marking grains by watershed algorithm, where the grains are marked by red color (b). HHCF and its fit by Gaussian function (c). The height scale for AFM images is given in nm.*

Because AFM measurements do not always produce clear and defect-free images, as an additional real space characterization method, we picked a SEM. The resulting images for different thin films are presented in Fig. 9.3. We observed a good convergence between AFM and SEM data, confirming the quality of AFM images. This fact is important for the AFM analysis presented earlier in Sec. 5.4.

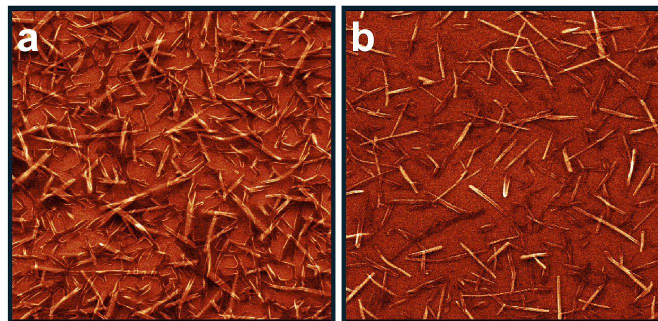


***Figure 9.3:*** *SEM images of dbSeQ thin films grown at RT: $d = 36$ nm (a), $d = 12$ nm (b).*

## 9.2 Additional XRR data

We performed series of *ex situ* and *in situ* XRR experiments, where the results are presented in Fig. 9.4. From the Fig. 9.4 (a) and (b) it is evident that the tendency of dbSeQ to grow as a rough film remains unchanged with a film thickness. We observe no scattering features for those scans, which we attribute to the high roughness that does not not change with thickness. For the LT-grown film depicted in Fig. 9.4 (c) we observe the absence of scattering features due to high roughness. This finding correlates with the AFM data and we suggest that the high roughness is a result of dewetting that occurs during the annealing of the film to RT. The AFM image of the RT-grown film with a high deposition rate (Fig. 5.16 (d)) reveals that the roughness of the film is relatively low compared to other RT-grown films. The XRR of this film is presented in Fig. 9.4 (d) and does not show the prominent features, even within the higher $q_z$-range.

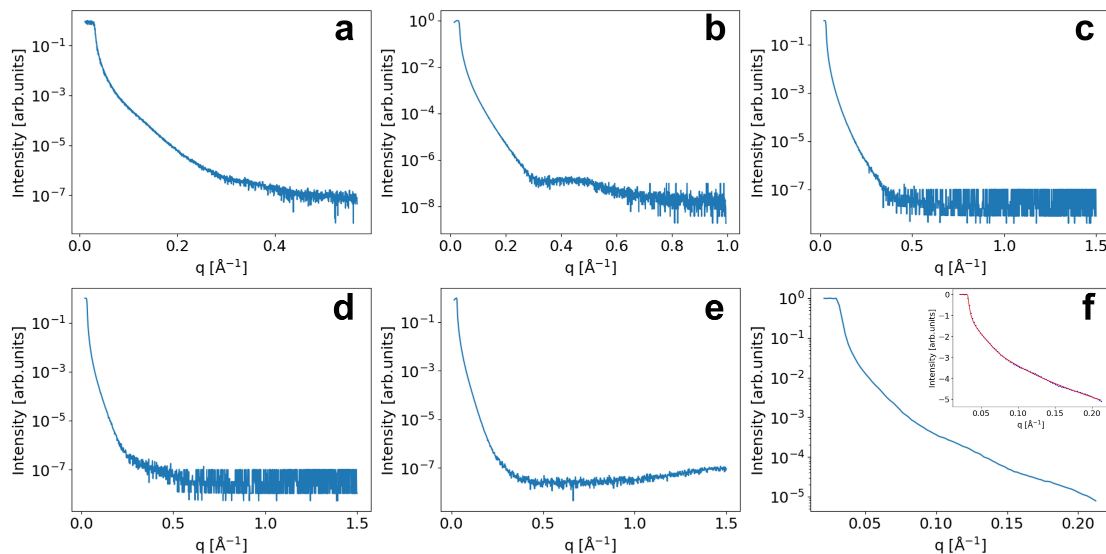


***Figure 9.4:*** *Ex situ XRR scans of dbSeQ thin films grown on Si/SiO$_x$ substrate, with deposition rate 0.3 nm/min: RT-grown film, $d_{nom}$ = 20 nm (a). RT-grown film, $d_{nom}$ = 10 nm (b) LT-grown film, $d_{nom}$ = 30 nm (c). RT-grown film with high deposition rate 1 nm/min, $d_{nom}$ = 50 nm (d). RT-grown film with nominal thickness $d_{nom}$ = 30 nm on the glass substrate. XRR scan was taken with higher exposure time (e). In situ XRR scan for the RT-grown film taken with high-intensity X-ray source. Nominal thickness $d_{nom}$ = 30 nm (f). The inset shows the fit result of the Kiessig fringes. All the y-axes are in logarithmic scale. Note that each image has different q-range.*

It is evident that the presence of significant noise becomes discernible in all the aforementioned scans, particularly at higher $q_z$ values, beyond which the scattered signal from the surface exhibits a decrease in intensity relative to regions of material near-critical angles [272]. In an effort to enhance the signal and mitigate noise,

the exposure time for a specific point was increased from 30 to 90 seconds. The resulting curve, presented in Fig. 9.4 (e), does not exhibit prominent reflectivity features, even upon closer examination.

A further attempt to detect features for RT-grown films was made *in situ*, directly after depositing a film with a nominal thickness of 20 nm with a source of the high brilliance at the ESRF synchrotron facility. The results are depicted in Fig. 9.4 (f). At first glance, the curve exhibits local minima, indicating its suitability as a candidate for fitting. To analyze the reflectivity data, we employed a custom-developed program based on the "refnx" data analysis package [206]. The inset in Fig. 9.4 (f) displays the fit result for the experimental data. The fitting yielded the following parameters: $d = 11 \pm 0.2$ nm and $\sigma_{RMS} = 3 \pm 1$ nm. These results are not correlate with a real data, which makes the analysis not reliable.

## 9.3 Additional GISAXS data

The section 5.2 contains the part about the evaluation of GISAXS data from raw patterns. In this section, several details about curve fitting that were not disclosed previously are added. In the current example, three peaks are being fitted, corresponding to the central and two side peaks in the GISAXS patterns. The side peaks in the current example are fitted with asymmetric Lorentzian functions (denoted "aLorentzian" in Fig. 9.5) and the central peaks is fitted as a combination of two Lorentzian functions (denoted as Lorentzian in Fig. 9.5).

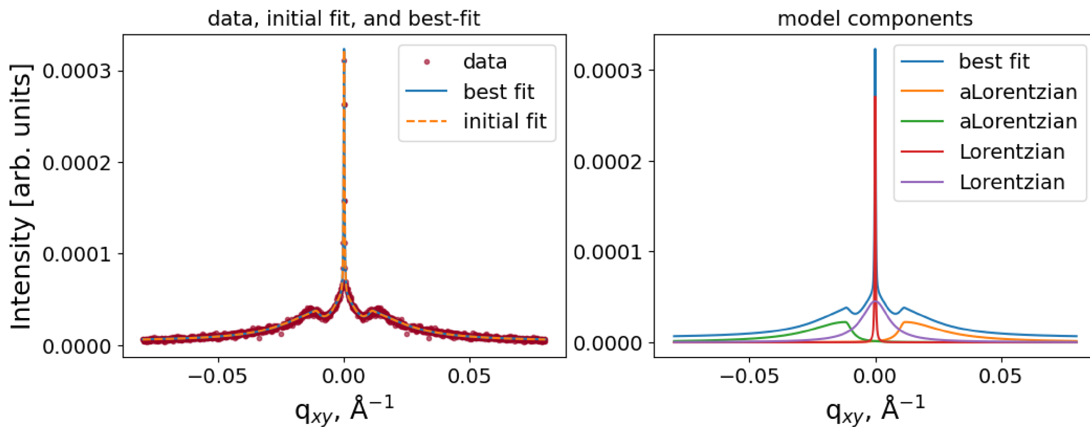


***Figure 9.5:*** *Example of the peak fitting procedure for one of GISAXS patterns taken during the growth of neat dbSeQ film at LT. The right part of the image contains separate functions are used in combination to create the best fit. The central part of the data is fitted with two Lorentzian functions.*

The present procedure is designed to estimate the peak parameters, including the peak position, width, and height (intensity). These parameters were used for

the physical interpretation of the results.

# List of Abbreviations

**AFM** Atomic Force Microscopy

**BA** BornAgain

**BHJ** Bulk Heterojunction

**BL** Bilayer

**CCD** Charge-Coupled Device

**CT** Charge Transfer

**CVD** Chemical Vapor Deposition

**dbSeQ** Dibenzoselenadiazoloquinoxaline

**DESY** Deutsches Elektronen-Synchrotron

**DIP** Diindenoperylene

**DWBA** Distorted Wave Born Approximation

**EA** Electron Affinity

**ES** Ehrlich-Schwoebel barrier

**ESRF** European Synchrotron Radiation Facility

**FWHM** Full Width at Half Maximum

**GISAXS** Grazing Incidence Small Angle X-Ray Scattering

**GIWAXS** Grazing Incidence Wide Angle X-Ray Scattering

**HOMO** Highest Occupied Molecular Orbital

**HHFC** Height-Height Correlation Function

**IE** Ionization Energy

**IGP** Ion Getter Pump

**LCAO** Linear Combination of Atomic Orbitals

**LT** Low Temperature

**LUMO** Lowest Unoccupied Molecular Orbital

**OMBD** Organic Molecular Beam Deposition

**OLED** Organic Light Emitting Diode

**OFET** Organic Field-Effect Transistor

**OPV** Organic Photovoltaics

**OSC** Organic Semiconductor

**OTFT** Organic Thin-Film Transistors

**PEN** Pentacene

**PHJ** Planar Heterojunction

**PL** Photoluminescence

**PVD** Physical Vapor Deposition

**QCM** Quartz Crystal Microbalance

**RMS** Root Mean Square

**RT** Room Temperature

**SAXS** Small Angle X-Ray Scattering

**SEM** Scanning Electron Microscopy

**TDM** Transition Dipole Moment

**TMP** Turbomolecular Pump

**TSP** Titanium Sublimation Pump

**UHV** Ultrahigh Vacuum

**UV-Vis** Ultraviolet-Visible

**VL** Vacuum Level

**XRR** X-Ray Reflectivity

# Bibliography


[1] R. Keyes, *Fundamental limits of silicon technology*, Proc. IEEE **89** (2001), 227–239.

[2] F. Oberbauer, T. J. Winkel, T. Böhnert, M. S. Claro, L. Benetti, I. undefinedaha, L. Francis, F. Moradi, R. Ferreira, M. Münzenberg, and T. S. Parvini, *Hybrid Opto-Electrical Excitation of Spin-Transfer Torque Nano-Oscillators for Advanced Computing*, 2025.

[3] R. Bryant, K.-T. Cheng, A. Kahng, K. Keutzer, W. Maly, R. Newton, L. Pileggi, J. Rabaey, and A. Sangiovanni-Vincentelli, *Limitations and challenges of computer-aided design technology for CMOS VLSI*, Proc. IEEE **89** (2001), 341–365.

[4] J. M. Shaw and P. F. Seidler, *Organic electronics: introduction*, IBM J. Res. Dev. **45** (2001), 3–9.

[5] A. Pochettino, *Sul comportamento foto-elettrico dell'antracene*, Atti Acad. Lincei Rend. **XV** (1906), 355–363.

[6] A. Pochettino, *Sull'effetto fotoelettrico nell'antracene*, Atti Acad. Lincei Rend. **XV** (1906), 171–179.

[7] C. Wang, *Weak intermolecular interactions for strengthening organic batteries*, Energy Environ. Mater. **3** (2020), 441–452.

[8] D. Chopra, *Understanding intermolecular interactions in the solid state: approaches and techniques*, Royal Society of Chemistry, 2018.

[9] S. E. Root, S. Savagatrup, A. D. Printz, D. Rodriquez, and D. Lipomi, *Mechanical Properties of Organic Semiconductors for Stretchable, Highly Flexible, and Mechanically Robust Electronics.*, Chem. Rev. **117 9** (2017), 6467–6499.

[10] N. R. Armstrong, W. Wang, D. M. Alloway, D. Placencia, E. Ratcliff, and M. Brumbach, *Organic/Organic Heterojunctions: Organic Light Emitting Diodes and Organic Photovoltaic Devices*, Macromol. Rapid Commun. **30** (2009), 717–731.

[11] T. W. Kelley, P. F. Baude, C. Gerlach, D. E. Ender, D. Muyres, M. A. Haase, D. E. Vogel, and S. D. Theiss, *Recent Progress in Organic Electronics: Materials, Devices, and Processes*, Chem. Mater. **16** (2004), 4413–4422.

[12] C. Wang, H. Dong, L. Jiang, and W. Hu, *Organic semiconductor crystals.*, Chem. Soc. Rev. **47** (2018), 422–500.

[13] Q. Liu, S. Bottle, and P. Sonar, *Developments of Diketopyrrolopyrrole-Dye-Based Organic Semiconductors for a Wide Range of Applications in Electronics*, Adv. Mater. **32** (2019), 1903882.

[14] D. Yang and D. Ma, *Development of Organic Semiconductor Photodetectors: From Mechanism to Applications*, Adv. Opt. Mater. **7** (2018), 1800522.

[15] J. Myers and J. Xue, *Organic semiconductors and their applications in photovoltaic devices*, Polym. Rev. **52** (2012), 1 – 37.

[16] T. Okamoto, C. P. Yu, C. Mitsui, M. Yamagishi, H. Ishii, and J. Takeya, *Bent-Shaped p-Type Small Molecule Organic Semiconductors: A Molecular Design Strategy for Next-Generation Practical Applications*, J. Am. Chem. Soc. (2020), 9083–9096.

[17] H. Bronstein, C. Nielsen, B. Schroeder, and I. McCulloch, *The role of chemical design in the performance of organic semiconductors*, Nat. Rev. Chem. **4** (2020), 66–77.

[18] G. Leising, S. Tasch, C. Brandstatter, F. Meghdadi, G. Froyer, and L. Athouel, *Red–green–blue light emission from a thin film electroluminescence device based on parahexaphenyl*, Adv. Mater. **9** (1997), 33.

[19] H. T. Yi, M. Payne, J. Anthony, and V. Podzorov, *Ultra-flexible solution-processed organic field-effect transistors*, Nat. Commun. **3** (2012), 1259.

[20] Z. Li, H. C. Wong, Z. Huang, H. Zhong, C.-H. Tan, W. Tsoi, J. Kim, J. Durrant, and J. Cabral, *Performance enhancement of fullerene-based solar cells by light processing*, Nat. Commun. **4** (2013), 2227.

[21] A. A. Virkar, S. Mannsfeld, Z. Bao, and N. Stingelin, *Organic Semiconductor Growth and Morphology Considerations for Organic Thin-Film Transistors*, Adv. Mater. **22** (2010), 3857–3875.

[22] F. Todescato, R. Capelli, F. Dinelli, M. Murgia, N. Camaioni, M. Yang, and M. Muccini, *Influence of the dielectric and of the active layer doping on the FET mobility in PPV-based devices*, Organic Light Emitting Materials and Devices XI, vol. 6655, SPIE, 2007, pp. 277–288.

[23] Y. D. Park, J. A. Lim, H. S. Lee, and K. Cho, *Interface engineering in organic transistors*, Mater. Today **10** (2007), 46–54.

[24] A. Virkar, S. Mannsfeld, J. H. Oh, M. F. Toney, Y. H. Tan, G.-y. Liu, J. C. Scott, R. Miller, and Z. Bao, *The role of OTS density on pentacene and $C_{60}$ nucleation, thin film growth, and transistor performance*, Adv. Funct. Mater. **19** (2009), 1962–1970.

[25] B. K. Crone, P. S. Davids, I. H. Campbell, and D. L. Smith, *Device model investigation of bilayer organic light emitting diodes*, J. Appl. Phys. **87** (2000), 1974–1982.

[26] G. Duva, P. Beyer, R. Scholz, V. Belova, A. Opitz, A. Hinderhofer, A. Gerlach, and F. Schreiber, *Ground-state charge-transfer interactions in donor:acceptor pairs of organic semiconductors – a spectroscopic study of two representative systems*, Phys. Chem. Chem. Phys. **21** (2019), 17190–17199.

[27] L. Qiu, J. A. Lim, X. Wang, W. H. Lee, M. Hwang, and K. Cho, *Versatile use of vertical-phase-separation-induced bilayer structures in organic thin-film transistors*, Adv. Mater. **20** (2008), 1141–1145.

[28] D. Zhang, W. Zhong, L. Ying, B. Fan, M. Li, Z. Gan, Z. Zeng, D. Chen, N. Li, F. Huang, and Y. Cao, *Overcoming incompatibility of donors and acceptors by constructing planar heterojunction organic solar cells*, Nano Energy **85** (2021), 105957.

[29] Y. Li and Y. Lin, *Planar heterojunctions for reduced non-radiative open-circuit voltage loss and enhanced stability of organic solar cells*, J. Mater. Chem. C. **9** (2021), 11715–11721.

[30] R. Banerjee, J. Novák, C. Frank, C. Lorch, A. Hinderhofer, A. Gerlach, and F. Schreiber, *Evidence for kinetically limited thickness dependent phase separation in organic thin film blends*, Phys. Rev. Lett. **110** (2013), 185506.

[31] A. Hinderhofer, A. Gerlach, S. Kowarik, F. Zontone, J. Krug, and F. Schreiber, *Smoothing and coherent structure formation in organic-organic heterostructure growth*, Europhys. Lett. **91** (2010), 56002.

[32] W. Brütting, *Introduction to the Physics of Organic Semiconductors*, John Wiley & Sons, Ltd, 2005.

[33] R. W. Schwartz, *Chemical solution deposition of perovskite thin films*, Chem. Mater. **9** (1997), 2325–2340.

[34] K. Lambert, R. K. Čapek, M. I. Bodnarchuk, M. V. Kovalenko, D. Van Thourhout, W. Heiss, and Z. Hens, *Langmuir-Schaefer Deposition of Quantum Dot Multilayers*, Langmuir **26** (2010), 7732–7736.

[35] N. A. Kotov, F. C. Meldrum, and J. H. Fendler, *Monoparticulate Layers of Titanium Dioxide Nanocrystallites with Controllable Interparticle Distances*, J. Phys. Chem. **98** (1994), 8827–8830.

[36] V. Santhanam and R. P. Andres, *Microcontact Printing of Uniform Nanoparticle Arrays*, Nano Lett. **4** (2003), 41–44.

[37] S. M. Rossnagel, *Thin film deposition with physical vapor deposition and related technologies*, J. Vac. Sci. Technol. A: Vac. Surf. Films **21** (2003), S74–S87.

[38] S. R. Forrest, *Ultrathin Organic Films Grown by Organic Molecular Beam Deposition and Related Techniques*, Chem. Rev. **97** (1997), 1793.

[39] A. Pancaldi, L. Raimondo, A. Minotto, and A. Sassella, *Post-growth dynamics and growth modeling of organic semiconductor thin films*, Langmuir **39** (2023), 3266–3272.

[40] S. M. Kowarik, *Real-time studies of thin film growth of organic semiconductors*, Ph.D. thesis, Wadham College, Oxford, 2006.

[41] S. Kowarik, A. Gerlach, and F. Schreiber, *Organic molecular beam deposition: fundamentals, growth dynamics, and in situ studies*, JJ. Phys. Condens. Matter **20** (2008), 184005.

[42] A. Gerlach, S. Sellner, S. Kowarik, and F. Schreiber, *In-situ X-ray scattering studies of OFET interfaces*, Phys. Status Solidi (A) **205** (2008), 461–474.

[43] M. Schwartzkopf, A. Buffet, V. Körstgens, E. Metwalli, K. Schlage, G. Benecke, J. Perlich, M. Rawolle, A. Rothkirch, B. Heidmann, G. Herzog, P. Müller-Buschbaum, R. Röhlsberger, R. Gehrke, and S. V. Roth, *From atoms to layers: in situ gold cluster growth kinetics during sputter deposition*, Nanoscale **5** (2013), 5053.

[44] R. Lazzari, F. Leroy, and G. Renaud, *Grazing-incidence small-angle x-ray scattering from dense packing of islands on surfaces: Development of distorted wave born approximation and correlation between particle sizes and spacing*, Phys. Rev. B **76** (2007), 125411.

[45] M. Schwartzkopf, A. Hinz, O. Polonskyi, T. Strunskus, F. C. Löhrer, V. Körstgens, P. Müller-Buschbaum, F. Faupel, and S. V. Roth, *Role of sputter deposition rate in tailoring nanogranular gold structures on polymer surfaces*, ACS Appl. Mater. Interfaces **9** (2017), 5629–5637, PMID: 28106380.

[46] A. Köhler and H. Bässler, *Electronic Processes in Organic Semiconductors: An Introduction*, Wiley, March 2015.

[47] M. Schwoerer and H. C. Wolf, *Organic Molecular Solids*, Wiley, December 2006.

[48] S. R. Forrest, *The path to ubiquitous and low-cost organic electronic appliances on plastic*, Nature **428** (2004), 911–918.

[49] Y. Sun, Y. Liu, and D. Zhu, *Advances in organic field-effect transistors*, J. Mater. Chem. **15** (2005), 53.

[50] M. Pope and C. Swenberg, *Electronic Processes in Organic Crystals and Polymers*, Monographs on the physics and chemistry of materials, Oxford University Press, 1999.

[51] N. Rußegger, *Organic Semiconductors: Mixing Behavior and Charge Transfer for Diindenoperylene/Dinaphthothienothiophene:Perylene Diimide-Based Binary Systems*, Ph.D. thesis, Eberhard Karls Universität, Tübingen, 2022.

[52] E. A. Meyer, R. K. Castellano, and F. Diederich, *Interactions with Aromatic Rings in Chemical and Biological Recognition*, Angew. Chem. Int. Ed. **42** (2003), 1210–1250.

[53] J. H. Williams, *The molecular electric quadrupole moment and solid-state architecture*, Acc. Chem. Res. **26** (1993), 593–598.

[54] C. R. Martinez and B. L. Iverson, *Rethinking the term "pi-stacking"*, Chem. Sci. **3** (2012), 2191.

[55] S. Grimme, *Do Special Noncovalent $\pi - \pi$ Stacking Interactions Really Exist?*, Angew. Chem. Int. Ed. **47** (2008), 3430–3434.

[56] F. Schreiber, *Organic molecular beam deposition: Growth studies beyond the first monolayer*, Phys. Status Solidi (A) **201** (2004), 1037.

[57] A. Hinderhofer and F. Schreiber, *Organic–Organic Heterostructures: Concepts and Applications*, ChemPhysChem **13** (2012), 628–643.

[58] J. T. Cheung and H. Sankur, *Growth of thin films by laser-induced evaporation*, Crit. Rev. Solid State Mater. Sci. **15** (1988), 63–109.

[59] R. G. Humphreys, J. S. Satchell, N. G. Chew, J. A. Edwards, S. W. Goodyear, S. E. Blenkinsop, O. D. Dosser, and A. G. Cullis, *Physical vapour deposition techniques for the growth of YBa2Cu3O7 thin films*, Supercond. Sci. Technol. **3** (1990), 38–52.

[60] T. Besmann, D. Stinton, and R. Lowden, *Chemical Vapor Deposition Techniques*, MRS Bull. **13** (1988), 45–51.

[61] S. P. Speakman, G. G. Rozenberg, K. J. Clay, W. I. Milne, A. Ille, I. A. Gardner, E. Bresler, and J. H. Steinke, *High performance organic semiconducting thin films: Ink jet printed polythiophene [rr-P3HT]*, Org. Electron **2** (2001), 65–73.

[62] L. Zhang, B. Lin, B. Hu, X. Xu, and W. Ma, *Blade-Cast Nonfullerene Organic Solar Cells in Air with Excellent Morphology, Efficiency, and Stability*, Adv. Mater. **30** (2018), 1800343.

[63] M. Abdelsamie, K. Zhao, M. R. Niazi, K. W. Chou, and A. Amassian, *In situ UV-visible absorption during spin-coating of organic semiconductors: a new probe for organic electronics and photovoltaics*, J. Mater. Chem. C. **2** (2014), 3373.

[64] K.-N. Tu, *Surface energies*, Cambridge University Press, 2010.

[65] D. Smith, *Thin-Film Deposition: Principles and Practice*, McGraw-Hill Education, 1995.

[66] M. Ohring, *The Materials Science of Thin Films*, Science Direct e-books, Academic Press, 1992.

[67] T. Michely and J. Krug, *Islands, Mounds and Atoms*, Springer Berlin Heidelberg, 2004.

[68] D. Mattox, *Handbook of Physical Vapor Deposition (PVD) Processing*, Online access with subscription: Proquest Ebook Central, Elsevier Science, 2014.

[69] G. Ehrlich and F. G. Hudda, *Atomic View of Surface Self-Diffusion: Tungsten on Tungsten*, J. Chem. Phys. **44** (1966), 1039–1049.

[70] R. L. Schwoebel and E. J. Shipsey, *Step Motion on Crystal Surfaces*, J. Appl. Phys. **37** (1966), 3682–3686.

[71] S. Krishna, *Handbook of Thin Film Deposition*, Elsevier, 2012.

[72] F. Brochard-Wyart, J. M. Di Meglio, D. Quere, and P. G. De Gennes, *Spreading of nonvolatile liquids in a continuum picture*, Langmuir **7** (1991), 335–338.

[73] P. G. de Gennes, *Wetting: statics and dynamics*, Rev. Mod. Phys. **57** (1985), 827–863.

[74] E. Schulz, *Nucleation and growth of thin films*, Acta Polym. **31** (1980), 216–216.

[75] H. Brune, M. Giovannini, K. Bromann, and K. Kern, *Self-organized growth of nanostructure arrays on strain-relief patterns*, Nature **394** (1998), 451–453.

[76] J. A. Venables, G. D. T. Spiller, and M. Hanbucken, *Nucleation and growth of thin films*, Rep. Prog. Phys. **47** (1984), 399.

[77] J. Pflaum, J. Niemax, and A. Tripathi, *Chemical and structural effects on the electronic transport in organic single crystals*, Chem. Phys. **325** (2006), 152–159.

[78] U. Heinemeyer, A. Hinderhofer, M. I. Alonso, J. O. Ossó, M. Garriga, M. Kytka, A. Gerlach, and F. Schreiber, *Uniaxial anisotropy of organic thin films determined by ellipsometry*, Phys. Status Solidi (A) **205** (2008), 927–930.

[79] A. C. Dürr, F. Schreiber, K. A. Ritley, V. Kruppa, J. Krug, H. Dosch, and B. Struth, *Rapid roughening in thin film growth of an organic semiconductor (diindenoperylene)*, Phys. Rev. Lett. **90** (2003), 016104.

[80] C. C. Mattheus, A. B. Dros, J. Baas, G. T. Oostergetel, A. Meetsma, J. L. de Boer, and T. T. Palstra, *Identification of polymorphs of pentacene*, Synth. Met. **138** (2003), 475–481.

[81] G. Witte and C. Wöll, *Growth of aromatic molecules on solid substrates for applications in organic electronics*, J. Mater. Res. **19** (2004), 1889.

[82] N. Karl, *Charge-carrier mobility in organic crystals*, Organic electronic materials: conjugated polymers and low molecular weight organic solids, Springer, 2001, pp. 283–326.

[83] R. B. Campbell, J. M. Robertson, and J. Trotter, *The crystal structure of hexacene, and a revision of the crystallographic data for tetracene*, Acta Crystallogr. **15** (1962), 289–290.

[84] U. Mazur and K. W. Hipps, *Kinetic and thermodynamic processes of organic species at the solution-solid interface: the view through an STM.*, Chem. Commun. **51 23** (2015), 4737–49.

[85] M. Sawatzki-Park, S. Wang, H. Kleemann, and K. Leo, *Highly Ordered Small Molecule Organic Semiconductor Thin-Films Enabling Complex, High-Performance Multi-Junction Devices*, Chem. Rev. **123** (2023), 8232 – 8250.

[86] K. Broch, A. Aufderheide, L. Raimondo, A. Sassella, A. Gerlach, and F. Schreiber, *Optical Properties of Blends: Influence of Mixing-Induced Disorder in Pentacene:Diindenoperylene versus Perfluoropentacene:Diindenoperylene*, J. Phys. Chem. C **117** (2013), 13952–13960.

[87] S. Hou, J. Yu, X. Zhuang, D. Li, Y. Liu, Z. Gao, T. Sun, F. Wang, and X. Yu, *Phase separation of P3HT/PMMA blend film formed semiconducting and dielectric layers in organic thin-film transistors for high sensitivity $NO_2$ detection*, ACS Appl. Mater. Interfaces (2019), 44521–44527.

[88] K. Broch, A. Gerlach, C. Lorch, J. Dieterle, J. Novák, A. Hinderhofer, and F. Schreiber, *Structure formation in perfluoropentacene: diindenoperylene blends and its impact on transient effects in the optical properties studied in real-time during growth*, J. Chem. Phys. **139** (2013), 174709.

[89] K. Broch, C. Bürker, J. Dieterle, S. Krause, A. Gerlach, and F. Schreiber, *Impact of molecular tilt angle on the absorption spectra of pentacene:perfluoropentacene blends*, Phys. Status Solidi (RRL) **7** (2013), 1084–1088.

[90] K. Nakano and K. Tajima, *Organic Planar Heterojunctions: From Models for Interfaces in Bulk Heterojunctions to High-Performance Solar Cells*, Adv. Mater. **29** (2017), 1603269.

[91] S. H. Kim, M. A. Saeed, S. Lee, and J. Shim, *Investigating the Indoor Performance of Planar Heterojunction Based Organic Photovoltaics*, IEEE J. Photovolt. **11** (2021), 997–1003.

[92] I. Markov, *Crystal Growth for Beginners: Fundamentals of Nucleation, Crystal Growth and Epitaxy*, G - Reference,Information and Interdisciplinary Subjects Series, World Scientific, 2003.

[93] J. Yang and D. Yan, *Weak epitaxy growth of organic semiconductor thin films*, Chem. Soc. Rev. **38** (2009), 2634.

[94] G. Koller, S. Berkebile, J. R. Krenn, F. P. Netzer, M. Oehzelt, T. Haber, R. Resel, and M. G. Ramsey, *Heteroepitaxy of Organic-Organic Nanostructures*, Nano Lett. **6** (2006), 1207–1212.

[95] J. O. Ossó, F. Schreiber, V. Kruppa, H. Dosch, M. Garriga, M. I. Alonso, and F. Cerdeira, *Controlled molecular alignment in phthalocyanine thin films on stepped sapphire surfaces*, Adv. Funct. Mater. **12** (2002), 455–460.

[96] S. Heutz, R. Cloots, and T. S. Jones, *Structural templating effects in molecular heterostructures grown by organic molecular-beam deposition*, Appl. Phys. Lett. **77** (2000), 3938–3940.

[97] S. Duhm, G. Heimel, I. Salzmann, H. Glowatzki, R. L. Johnson, A. Vollmer, J. P. Rabe, and N. Koch, *Orientation-dependent ionization energies and interface dipoles in ordered molecular assemblies*, Nat. Mater. **7** (2008), 326–332.

[98] D. de Oteyza, E. Barrena, S. Sellner, J. Ossó, and H. Dosch, *Molecular structure and growth morphologies of pentacene/fluorinated copper-phthalocyanine heterostructures*, Thin Solid Films **516** (2008), 7525–7529.

[99] D. G. de Oteyza, T. N. Krauss, E. Barrena, S. Sellner, H. Dosch, and J. O. Ossó, *Towards controlled bottom-up architectures in organic heterostructures*, Appl. Phys. Lett. **90** (2007), 076102.

[100] E. Barrena, D. G. de Oteyza, S. Sellner, H. Dosch, J. O. Ossó, and B. Struth, *In situ study of the growth of nanodots in organic heteroepitaxy*, Phys. Rev. Lett. **97** (2006), 076102.

[101] D. G. de Oteyza, E. Barrena, H. Dosch, and Y. Wakayama, *Nanoconfinement effects in the self-assembly of diindenoperylene (DIP) on Cu(111) surfaces*, Phys. Chem. Chem. Phys. **11** (2009), 8741.

[102] J. Als-Nielsen and D. McMorrow, *Elements of Modern X-ray Physics*, Wiley, 2011.

[103] I. Zaluzhnyy and F. Schreiber, *Lecture notes: X-ray and Neutron scattering*, 2024, http://www.soft-matter.uni-tuebingen.de/teaching/scattering_lecture/LectureNotes.pdf.

[104] W. C. Röntgen, *On a New Kind of Rays*, Science **3** (1896), 227–231.

[105] W. H. Bragg and W. L. Bragg, *The Reflection of X-rays by Crystals*, Proc. R. Soc. Lond. A **88** (1913), 428–438.

[106] L. S. Konstantinova, I. E. Bobkova, Y. V. Nelyubina, E. A. Chulanova, I. G. Irtegova, N. V. Vasilieva, P. S. Camacho, S. E. Ashbrook, G. Hua, A. M. Z. Slawin, J. D. Woollins, A. V. Zibarev, and O. A. Rakitin, *[1, 2, 5]Selenadiazolo[3, 4-b]pyrazines: Synthesis from 3, 4-Diamino-1, 2, 5-selenadiazole and Generation of Persistent Radical Anions*, Eur. J. Org. Chem. **2015** (2015), 5585–5593.

[107] L. S. Konstantinova and O. A. Rakitin, *Chalcogen exchange in chalcogen–nitrogen $\pi$-heterocycles*, Mendeleev Commun. **31** (2021), 433–441.

[108] J. A. Pereira, A. M. Pessoa, M. N. D. Cordeiro, R. Fernandes, C. Prudêncio, J. P. Noronha, and M. Vieira, *Quinoxaline, its derivatives and applications: A State of the Art review*, Eur. J. Med. Chem. **97** (2015), 664–672.

[109] H. Ouahine, A. Hasnaoui, I. Hdoufane, R. Idouhli, A. Abouelfida, M. A. Ali, and L. El Firdoussi, *Benzo [c][1, 2, 5] selenadiazole organoselenium derivatives: synthesis, X-ray, DFT, Fukui analysis and electrochemical behavior*, J. Mol. Struct. **1199** (2020), 126914.

[110] P. A. Lewis, *Colored organic pigments*, 493–526, Elsevier, 2000, p. 493–526.

[111] M. A. Heinrich, J. Pflaum, A. K. Tripathi, W. Frey, M. L. Steigerwald, and T. Siegrist, *Enantiotropic Polymorphism in Di-indenoperylene*, J. Phys. Chem. C **111** (2007), 18878–18881.

[112] A. C. Dürr, F. Schreiber, M. Münch, N. Karl, B. Krause, V. Kruppa, and H. Dosch, *High structural order in thin films of the organic semiconductor diindenoperylene*, Appl. Phys. Lett. **81** (2002), 2276–2278.

[113] S. Kowarik, A. Gerlach, S. Sellner, L. Cavalcanti, O. Konovalov, and F. Schreiber, *Real-time X-ray diffraction measurements of structural dynamics and polymorphism in diindenoperylene growth*, Appl. Phys. A **95** (2009), 233–239.

[114] A. C. Dürr, N. Koch, M. Kelsch, A. Rühm, J. Ghijsen, R. L. Johnson, J.-J. Pireaux, J. Schwartz, F. Schreiber, H. Dosch, and A. Kahn, *Interplay between morphology, structure, and electronic properties at diindenoperylene-gold interfaces*, Phys. Rev. B **68** (2003), 115428.

[115] A. Dürr, B. Nickel, V. Sharma, U. Täffner, and H. Dosch, *Observation of competing modes in the growth of diindenoperylene on $SiO_2$*, Thin Solid Films **503** (2006), 127–132.

[116] C. Frank, R. Banerjee, M. Oettel, A. Gerlach, J. Novák, G. Santoro, and F. Schreiber, *Analysis of island shape evolution from diffuse x-ray scattering of organic thin films and implications for growth*, Phys. Rev. B **90** (2014), 205401.

[117] M. Heilig, M. Domhan, and H. Port, *Optical properties and morphology of thin diindenoperylene films*, J. Lumin. **110** (2004), 290, 325th Wilhelm and Else Heraeus Workshop. Organic Molecular Solids : Excited Electronic States and Optical Properties.

[118] X. Zhang, E. Barrena, D. de Oteyza, and H. Dosch, *Transition from layer-by-layer to rapid roughening in the growth of DIP on SiO2*, Surf. Sci. **601** (2007), 2420.

[119] C. Frank, J. Novák, R. Banerjee, A. Gerlach, F. Schreiber, A. Vorobiev, and S. Kowarik, *Island size evolution and molecular diffusion during growth of organic thin films followed by time-resolved specular and off-specular scattering*, Phys. Rev. B **90** (2014), 045410.

[120] S. Schiefer, M. Huth, A. Dobrinevski, and B. Nickel, *Determination of the Crystal Structure of Substrate-Induced Pentacene Polymorphs in Fiber Structured Thin Films*, J. Am. Chem. Soc. **129** (2007), 10316–10317.

[121] D. Käfer and G. Witte, *Growth of crystalline rubrene films with enhanced stability*, Phys. Chem. Chem. Phys. **7** (2005), 2850.

[122] M. Hodas, P. Siffalovic, P. Nádaždy, N. Mrkyvková, M. Bodík, Y. Halahovets, G. Duva, B. Reisz, O. Konovalov, W. Ohm, M. Jergel, E. Majková, A. Gerlach, A. Hinderhofer, and F. Schreiber, *Real-Time Monitoring of Growth and Orientational Alignment of Pentacene on Epitaxial Graphene for Organic Electronics*, ACS Appl. Nano Mater. **1** (2018), 2819.

[123] C. P. Theurer, F. Laible, J. Tang, K. Broch, M. Fleischer, and F. Schreiber, *Strong light-matter coupling in pentacene thin films on plasmonic arrays*, Nanoscale **15** (2023), 11707.

[124] Q. Wang, M.-T. Chen, A. Franco-Cañellas, B. Shen, T. Geiger, H. F. Bettinger, F. Schreiber, I. Salzmann, A. Gerlach, and S. Duhm, *Impact of*

*fluorination on interface energetics and growth of pentacene on Ag(111)*, Beilstein J. Nanotechnol. **11** (2020), 1361.

[125] K. Broch, J. Dieterle, F. Branchi, N. J. Hestand, Y. Olivier, H. Tamura, C. Cruz, V. M. Nichols, A. Hinderhofer, D. Beljonne, F. C. Spano, G. Cerullo, C. J. Bardeen, and F. Schreiber, *Robust singlet fission in pentacene thin films with tuned charge transfer interactions*, Nat. Commun. **9** (2018), 954.

[126] S. Kowarik, A. Hinderhofer, C. Wang, C. Weber, A. Gerlach, A. Hexemer, S. R. Leone, and F. Schreiber, *Identification of an organic semiconductor superlattice structure of pentacene and perfluoro-pentacene through resonant and non-resonant X-ray scattering*, AIP Adv. **5** (2015), 117241.

[127] S. Duhm, C. Bürker, J. Niederhausen, I. Salzmann, T. Hosokai, J. Duvernay, S. Kera, F. Schreiber, N. Koch, N. Ueno, and A. Gerlach, *Pentacene on Ag(111): Correlation of Bonding Distance with Intermolecular Interaction and Order*, ACS Appl. Mater. Interfaces **5** (2013), 9377.

[128] F. Anger, J. Ossó, U. Heinemeyer, K. Broch, R. Scholz, A. Gerlach, and F. Schreiber, *Photoluminescence spectroscopy of pure pentacene, perfluoropentacene, and mixed thin films*, J. Chem. Phys. **136** (2012), 054701.

[129] G. Yoshikawa, T. Miyadera, R. Onoki, K. Ueno, I. Nakai, S. Entani, S. Ikeda, D. Guo, M. Kiguchi, H. Kondoh, T. Ohta, and K. Saiki, *In-situ measurement of molecular orientation of the pentacene ultrathin films grown on $SiO_2$ substrates*, Surf. Sci. **600** (2006), 2518–2522.

[130] C. C. Mattheus, A. B. Dros, J. Baas, A. Meetsma, J. L. d. Boer, and T. T. M. Palstra, *Polymorphism in pentacene*, Acta Crystallogr. Sect. C: Cryst. Struct. Commun. **57** (2001), 939–941.

[131] I. Bouchoms, W. Schoonveld, J. Vrijmoeth, and T. Klapwijk, *Morphology identification of the thin film phases of vacuum evaporated pentacene on $SiO_2$ substrates*, Synth. Met. **104** (1999), 175 – 178 (Dutch).

[132] A. C. Mayer, A. Kazimirov, and G. G. Malliaras, *Dynamics of Bimodal Growth in Pentacene Thin Films*, Phys. Rev. Lett. **97** (2006), 105503.

[133] A. C. Mayer, R. Ruiz, R. L. Headrick, A. Kazimirov, and G. G. Malliaras, *Early stages of pentacene film growth on silicon oxide*, Org. Electron **5** (2004), 257–263.

[134] H. Zhu, Q. L. Li, X. J. She, and S. D. Wang, *Surface roughening evolution in pentacene thin film growth*, Appl. Phys. Lett. **98** (2011), 243304.

[135] D. Holmes, S. Kumaraswamy, A. J. Matzger, and K. P. C. Vollhardt, *On the Nature of Nonplanarity in the [N]Phenylenes*, Chem. Eur. J. **5** (1999), 3399–3412.

[136] K.-G. Wagner, *A brief review of Knudsen-cells for applications in experimental research*, Vacuum **34** (1984), 743–746.

[137] K. D. Carlson, P. W. Gilles, and R. J. Thorn, *Molecular and Hydrodynamical Effusion of Mercury Vapor from Knudsen Cells*, J. Chem. Phys. **38** (1963), 2725–2735.

[138] J. I. AG, *NanoWizard AFM Handbook*, 2012, https://www.bruker.com/de.html.

[139] R. Colton, *Procedures in Scanning Probe Microscopies*, no. v. 1, Wiley, 1998.

[140] G. Duva, *Structural and spectroscopic studies of molecular semiconductor donor:acceptor systems for organic optoelectronics*, Ph.D. thesis, Eberhard Karls Universität, Tübingen, 2019.

[141] G. Binnig, C. F. Quate, and C. Gerber, *Atomic Force Microscope*, Phys. Rev. Lett. **56** (1986), 930–933.

[142] D. Nečas and P. Klapetek, *Gwyddion: an open-source software for SPM data analysis*, Cent. Eur. J. Phys. **10** (2012), 181.

[143] M. Knoll, *Aufladepotentiel und sekundäremission elektronenbestrahlter körper*, Z. techn. Phys. **16** (1935), 467.

[144] J. I. Goldstein, D. E. Newbury, P. Echlin, D. C. Joy, C. E. Lyman, E. Lifshin, L. Sawyer, and J. R. Michael, *Scanning Electron Microscopy and X-ray Microanalysis: Third Edition*, Springer US, 2003.

[145] L. Reimer, *Scanning Electron Microscopy: Physics of Image Formation and Microanalysis*, Springer Berlin Heidelberg, 1998.

[146] D. C. Joy, *Principles of Analytical Electron Microscopy*, Springer US, 1986.

[147] J. B. Pawley, *Handbook Of Biological Confocal Microscopy*, Springer US, 2006.

[148] T. E. Everhart and R. F. M. Thornley, *Wide-band detector for micro-microampere low-energy electron currents*, J. Sci. Instrum. **37** (1960), 246–248.

[149] B. Reisz, *Structure Formation during Organic Molecular Beam Deposition*, Ph.D. thesis, Eberhard Karls Universität, Tübingen, 2021.

[150] V. Holý and T. Baumbach, *Nonspecular X-ray reflection from rough multilayers*, Phys. Rev. B **49** (1994), 10668.

[151] L. G. Parratt, *Surface Studies of Solids by Total Reflection of X-Rays*, Phys. Rev. **95** (1954), 359.

[152] P. Willmott, *An Introduction to Synchrotron Radiation: Techniques and Applications*, Wiley, 2019.

[153] H. Kiessig, *Interferenz von Röntgenstrahlen an dünnen Schichten*, Ann. Phys. **402** (1931), 769–788.

[154] L. Nevot, B. Pardo, and J. Corno, *Characterization of X-UV multilayers by grazing incidence X-ray reflectometry*, Rev. phys. appl. **23** (1988), 1675–1686.

[155] P. Müller-Buschbaum, *The Active Layer Morphology of Organic Solar Cells Probed with Grazing Incidence Scattering Techniques*, Adv. Mater. **26** (2014), 7692–7709.

[156] J. A. Steele, E. Solano, D. Hardy, D. Dayton, D. Ladd, K. White, P. Chen, J. Hou, H. Huang, R. A. Saha, L. Wang, F. Gao, J. Hofkens, M. B. J. Roeffaers, D. Chernyshov, and M. F. Toney, *How to GIWAXS: Grazing Incidence Wide Angle X-Ray Scattering Applied to Metal Halide Perovskite Thin Films*, Adv. Energy Mater **13** (2023), 2300760.

[157] G. Renaud, R. Lazzari, C. Revenant, A. Barbier, M. Noblet, O. Ulrich, F. Leroy, J. Jupille, Y. Borensztein, C. R. Henry, J.-P. Deville, F. Scheurer, J. Mane-Mane, and O. Fruchart, *Real-time monitoring of growing nanoparticles*, Science **300** (2003), 1416.

[158] P. Müller-Buschbaum, *Grazing incidence small-angle X-ray scattering: an advanced scattering technique for the investigation of nanostructured polymer films*, Anal. Bioanal. Chem. **376** (2003), 3–10.

[159] J. R. Levine, J. B. Cohen, Y. W. Chung, and P. Georgopoulos, *Grazing-incidence small-angle X-ray scattering: new tool for studying thin film growth*, J. Appl. Crystallogr. **22** (1989), 528–532.

[160] G. Renaud, R. Lazzari, and F. Leroy, *Probing surface and interface morphology with Grazing Incidence Small Angle X-Ray Scattering*, Surf. Sci. Rep. **64** (2009), 255.

[161] Y. Yoneda, *Anomalous Surface Reflection of X Rays*, Phys. Rev. **131** (1963), 2010–2013.

[162] S. K. Sinha, E. B. Sirota, S. Garoff, and H. B. Stanley, *X-ray and neutron scattering from rough surfaces*, Phys. Rev. B **38** (1988), 2297.

[163] V. Holy, *High-Resolution X-Ray Scattering from Thin Films and Multilayers*, Springer Berlin Heidelberg, 1999.

[164] D. Babonneau, *FitGISAXS: software package for modelling and analysis of GISAXS data using IGOR Pro*, J. Appl. Crystallogr. **43** (2010), 929–936.

[165] G. Pospelov, W. Van Herck, J. Burle, J. M. Carmona Loaiza, C. Durniak, J. M. Fisher, M. Ganeva, D. Yurov, and J. Wuttke, *BornAgain: software for simulating and fitting grazing-incidence small-angle scattering*, J. Appl. Crystallogr. **53** (2020), 262.

[166] A. Nejati, M. Svechnikov, and J. Wuttke, *BornAgain, software for GISAS and reflectometry: Releases 1.17 to 20*, EPJ Web Conf. **286** (2023), 06004.

[167] N. J. Hestand and F. C. Spano, *Expanded Theory of H- and J-Molecular Aggregates: The Effects of Vibronic Coupling and Intermolecular Charge Transfer*, Chem. Rev. **118** (2018), 7069–7163.

[168] J. Gierschner, J. Shi, B. Milián-Medina, D. Roca-Sanjuán, S. Varghese, and S. Park, *Luminescence in Crystalline Organic Materials: From Molecules to Molecular Solids*, Adv. Opt. Mater. **9** (2021), 2002251.

[169] M. Kasha, *Characterization of electronic transitions in complex molecules*, Faraday Discuss. **9** (1950), 14.

[170] A. Pylypenko, E. Chulanova, F. Unger, J. Keck, I. Zaluzhnyy, I. Dax, M. Schwartzkopf, A. Gerlach, A. Hinderhofer, A. J. Meixner, and F. Schreiber, *Thin Films of Conjugated Chalcogenadiazole: Growth, Structure, and Optical Properties of Substituted Selenadiazoloquinoxaline*, J. Phys. Chem. C **128** (2024), 8104–8113.

[171] A. Pylypenko, D. Lapkin, E. Chulanova, I. Zaluzhnyy, V. Munteanu, A. Gerlach, A. Hinderhofer, M. Schwartzkopf, M. Jankowski, O. Konovalov, and F. Schreiber, *Growth, structure and optical properties of neat, bilayer and codeposited thin films: Combining dibenzoselenadiazoloquinoxaline with diindenoperylene and pentacene*, J. Phys. Chem. C **129** (2025), 21223–21234.

[172] A. Mishra and P. Bäuerle, *Small Molecule Organic Semiconductors on the Move: Promises for Future Solar Energy Technology*, Angew. Chem. Int. Ed. **51** (2012), 2020–2067.

[173] C. Wang, H. Dong, W. Hu, Y. Liu, and D. Zhu, *Semiconducting pi-Conjugated Systems in Field-Effect Transistors: A Material Odyssey of Organic Electronics*, Chem. Rev. **112** (2012), 2208–2267, PMID: 22111507.

[174] A. Wadsworth, M. Moser, A. Marks, M. S. Little, N. Gasparini, C. J. Brabec, D. Baran, and I. McCulloch, *Critical review of the molecular design progress in non-fullerene electron acceptors towards commercially viable organic solar cells*, Chem. Soc. Rev. **48** (2019), 1596–1625.

[175] G. Zhang, F. R. Lin, F. Qi, T. Heumüller, A. Distler, H.-J. Egelhaaf, N. Li, P. C. Y. Chow, C. J. Brabec, A. K.-Y. Jen, and H.-L. Yip, *Renewed Prospects for Organic Photovoltaics*, Chem. Rev. **122** (2022), 14180–14274, PMID: 35929847.

[176] D. Cortizo-Lacalle, C. Gozalvez, M. Olano, X. Sun, M. Melle-Franco, L. E. Hueso, and A. Mateo-Alonso, *Bisthiadiazole-Fused Tetraazapentacenequinone: An Air-Stable Solution-Processable n-Type Organic Semiconductor*, Org. Let. **17** (2015), 5902–5905.

[177] P.-Y. Gu, J. Zhang, G. Long, Z. Wang, and Q. Zhang, *Solution-processable thiadiazoloquinoxaline-based donor–acceptor small molecules for thin-film transistors*, J. Mater. Chem. C **4** (2016), 3809–3814.

[178] J. W. Jung, J. W. Jo, E. H. Jung, and W. H. Jo, *Recent progress in high efficiency polymer solar cells by rational design and energy level tuning of low bandgap copolymers with various electron-withdrawing units*, Org. Electron **31** (2016), 149–170.

[179] H. Mori, *Development of semiconducting polymers based on a novel heteropolycyclic aromatic framework*, Polym. J. **53** (2021), 975–987.

[180] B. A. D. Neto, A. A. M. Lapis, E. N. da Silva Júnior, and J. Dupont, *2,1,3-Benzothiadiazole and Derivatives: Synthesis, Properties, Reactions, and Applications in Light Technology of Small Molecules*, Eur. J. Org. Chem. **2013** (2013), 228–255.

[181] W. Wang, B. Ji, and Y. Zhang, *Chalcogen Bond: A Sister Noncovalent Bond to Halogen Bond*, J. Phys. Chem. A **113** (2009), 8132–8135, PMID: 19537765.

[182] J. Alfuth, B. Zadykowicz, A. Sikorski, T. Połoński, K. Eichstaedt, and T. Olszewska, *Effect of Aromatic System Expansion on Crystal Structures of 1,2,5-Thia- and 1,2,5-Selenadiazoles and Their Quaternary Salts: Synthesis, Structure, and Spectroscopic Properties*, Materials **13** (2020), 4908.

[183] A. F. Cozzolino, I. Vargas-Baca, S. Mansour, and A. H. Mahmoudkhani, *The Nature of the Supramolecular Association of 1,2,5-Chalcogenadiazoles*, J. Am. Chem. Soc. **127** (2005), 3184–3190, PMID: 15740158.

[184] J. S. Murray, P. Lane, T. Clark, and P. Politzer, *$\sigma$-hole bonding: molecules containing group VI atoms*, J. Mol. Model. **13** (2007), 1033–1038.

[185] A. H. Bui, A. D. Fernando Pulle, A. S. Micallef, J. J. Lessard, and B. T. Tuten, *Dynamic Chalcogen Squares for Material and Topological Control over Macromolecules*, Angew. Chem. Int. Ed. **63** (2024), e202404474.

[186] E. A. Radiush, H. Wang, E. A. Chulanova, Y. A. Ponomareva, B. Li, Q. Y. Wei, G. E. Salnikov, S. Y. Petrakova, N. A. Semenov, and A. V. Zibarev, *Halide Complexes of 5,6-Dicyano-2,1,3-Benzoselenadiazole with 1:4 Stoichiometry: Cooperativity between Chalcogen and Hydrogen Bonding*, ChemPlusChem **88** (2023), e202300523.

[187] K. Eichstaedt, A. Wasilewska, B. Wicher, M. Gdaniec, and T. Połoński, *Supramolecular Synthesis Based on a Combination of Se···N Secondary Bonding Interactions with Hydrogen and Halogen Bonds*, Cryst. Growth Des. **16** (2016), 1282–1293.

[188] H. Li, G. Giri, J. B.-H. Tok, and Z. Bao, *Toward high-mobility organic field-effect transistors: Control of molecular packing and large-area fabrication of single-crystal-based devices*, MRS Bull. **38** (2013), 34–42.

[189] D. Kim, S. Lee, J. Park, J. Lee, H. C. Choi, K. Kim, and S. Ryu, *In-plane and out-of-plane excitonic coupling in 2D molecular crystals*, Nat. Commun. **14** (2023), 2736.

[190] J. Hagara, H. Kim, J. Hagenlocher, I. Zaluzhnyy, A. Gerlach, A. Hinderhofer, S. V. Roth, W. Brütting, and F. Schreiber, *Improved order and transport in $C_{60}$ thin films grown on $SiO_2$ via use of transient templates*, Appl. Phys. Lett. **121** (2022), 182101.

[191] Z. Chen, A. Lohr, C. R. Saha-Möller, and F. Würthner, *Self-assembled π-stacks of functional dyes in solution: structural and thermodynamic features*, Chem. Soc. Rev. **38** (2009), 564–584.

[192] T. Dallos, D. Beckmann, G. Brunklaus, and M. Baumgarten, *Thiadiazoloquinoxaline–Acetylene Containing Polymers as Semiconductors in Ambipolar Field Effect Transistors*, J. Am. Chem. Soc. **133** (2011), 13898–13901.

[193] T. T. Steckler, P. Henriksson, S. Mollinger, A. Lundin, A. Salleo, and M. R. Andersson, *Very Low Band Gap Thiadiazoloquinoxaline Donor–Acceptor Polymers as Multi-tool Conjugated Polymers*, J. Am. Chem. Soc. **136** (2014), 1190–1193.

[194] C. An, S. Zhou, and M. Baumgarten, *Condensed Derivatives of Thiadiazoloquinoxaline as Strong Acceptors*, Cryst. Growth Des. **15** (2015), 1934–1938.

[195] S.-i. Kato, K. Watanabe, M. Tamura, M. Ueno, M. Nitani, Y. Ie, Y. Aso, T. Yamanobe, H. Uehara, and Y. Nakamura, *Tetraalkoxyphenanthrene-Fused Thiadiazoloquinoxalines: Synthesis, Electronic, Optical, and Electrochemical Properties, and Self-Assembly*, J. Org. Chem. **82** (2017), 3132–3143.

[196] M. Müller, S. Koser, O. Tverskoy, F. Rominger, J. Freudenberg, and U. H. F. Bunz, *Thiadiazolo-Azaacenes*, Chem. Eur. J. **25** (2019), 6082–6086.

[197] H. Sirringhaus, P. J. Brown, R. H. Friend, M. M. Nielsen, K. Bechgaard, B. M. W. Langeveld-Voss, A. J. H. Spiering, R. A. J. Janssen, E. W. Meijer, P. Herwig, and D. M. de Leeuw, *Two-dimensional charge transport in self-organized, high-mobility conjugated polymers*, Nature **401** (1999), 685–688.

[198] S. H. Amsterdam, T. LaMountain, T. K. Stanev, V. K. Sangwan, R. López-Arteaga, S. Padgaonkar, K. Watanabe, T. Taniguchi, E. A. Weiss, T. J. Marks, M. C. Hersam, and N. P. Stern, *Tailoring the Optical Response of Pentacene Thin Films via Templated Growth on Hexagonal Boron Nitride*, J. Phys. Chem. Letters **12** (2020), 26–31.

[199] G. Duva, A. Mann, L. Pithan, P. Beyer, J. Hagenlocher, A. Gerlach, A. Hinderhofer, and F. Schreiber, *Template-free orientation selection of rod-like molecular semiconductors in polycrystalline films*, J. Phys. Chem. Letters **10** (2019), 1031–1036.

[200] A. Hofmann, M. Schmid, and W. Brütting, *The Many Facets of Molecular Orientation in Organic Optoelectronics*, Adv. Opt. Mater. **9** (2021), 2101004.

[201] U. Heinemeyer, K. Broch, A. Hinderhofer, M. Kytka, R. Scholz, A. Gerlach, and F. Schreiber, *Real-Time Changes in the Optical Spectrum of Organic Semiconducting Films and Their Thickness Regimes during Growth*, Phys. Rev. Lett. **104** (2010), 257401.

[202] K. A. Ritley, B. Krause, F. Schreiber, and H. Dosch, *A portable ultrahigh vacuum organic molecular beam deposition system for in situ x-ray diffraction measurements*, Rev. Sci. Instrum. **72** (2001), 1453.

[203] P. Klapetek, I. Ohlídal, A. Montaigne-Ramil, A. Bonanni, D. Stifter, and H. Sitter, *Atomic Force Microscopy Characterization of ZnTe Epitaxial Thin Films*, Jpn. J. Appl. Phys. **42** (2003), 4706.

[204] A. Pimpinelli and J. Villain, *Physics of crystal growth*, Cambridge University Press, 1998.

[205] A.-L. Barabási and H. E. Stanley, *Fractal concepts in surface growth*, Cambridge University Press, 1995.

[206] A. R. J. Nelson and S. W. Prescott, *refnx: neutron and X-ray reflectometry analysis in Python*, J. Appl. Crystallogr. **52** (2019), 193–200.

[207] A. Greco, V. Starostin, E. Edel, V. Munteanu, N. Rußegger, I. Dax, C. Shen, F. Bertram, A. Hinderhofer, A. Gerlach, and F. Schreiber, *Neural network analysis of neutron and x-ray reflectivity data: automated analysis using mlreflect, experimental errors and feature engineering*, J. Appl. Crystallogr. **55** (2022), 362.

[208] A. Hinderhofer, A. Greco, V. Starostin, V. Munteanu, L. Pithan, A. Gerlach, and F. Schreiber, *Machine learning for scattering data: strategies, perspectives and applications to surface scattering*, J. Appl. Crystallogr. **56** (2023), 3–11.

[209] V. Munteanu, V. Starostin, A. Greco, L. Pithan, A. Gerlach, A. Hinderhofer, S. Kowarik, and F. Schreiber, *Neural network analysis of neutron and X-ray reflectivity data incorporating prior knowledge*, J. Appl. Crystallogr. **57** (2024), 456–469.

[210] A. Abukaev, C. Völter, M. Romodin, S. Schwartzkopff, F. Bertram, O. Konovalov, A. Hinderhofer, D. Lapkin, and F. Schreiber, *A Python Package for Fast Data Reduction in Grazing-Incidence Diffraction (GID)*, J. Appl. Crystallogr. (2025), submitted.

[211] M. Bohra, A. S. Bandaru, P. Grammatikopoulos, and V. Singh, *Versatile gold-polymer nanointerfaces probed by GISAXS*, Mater. Today Chem. **17** (2020), 100297.

[212] M. Schwartzkopf and S. Roth, *Investigating Polymer–Metal Interfaces by Grazing Incidence Small-Angle X-Ray Scattering from Gradients to Real-Time Studies*, Nanomaterials **6** (2016), 239.

[213] G. Herzog, G. Benecke, A. Buffet, B. Heidmann, J. Perlich, J. F. H. Risch, G. Santoro, M. Schwartzkopf, S. Yu, W. Wurth, and S. V. Roth, *In Situ Grazing Incidence Small-Angle X-ray Scattering Investigation of Polystyrene Nanoparticle Spray Deposition onto Silicon*, Langmuir **29** (2013), 11260–11266.

[214] P. Müller-Buschbaum, *Grazing incidence small-angle neutron scattering: challenges and possibilities*, Polym. J. **45** (2012), 34–42.

[215] T. Salditt, T. H. Metzger, J. Peisl, and G. Goerigk, *Non-specular x-ray scattering from thin films and multilayers with small-angle scattering equipment*, J. Phys. D: Appl. Phys. **28** (1995), A236.

[216] P. Müller-Buschbaum, P. Vanhoorne, V. Scheumann, and M. Stamm, *Observation of nano-dewetting structures*, EPL **40** (1997), 655.

[217] K. Sankhala, D. F. Wieland, J. Koll, M. Radjabian, C. Abetz, and V. Abetz, *Self-assembly of block copolymers during hollow fiber spinning: an in situ small-angle x-ray scattering study*, Nanoscale **11** (2019), 7634–7647.

[218] G. Santoro, S. Yu, M. Schwartzkopf, P. Zhang, S. Koyiloth Vayalil, J. F. H. Risch, M. A. Rübhausen, M. Hernández, C. Domingo, and S. V. Roth, *Silver substrates for surface enhanced raman scattering: Correlation between nanostructure and raman scattering enhancement*, Appl. Phys. Lett. **104** (2014), 243107.

[219] L. Yang, G. Li, M. Zhao, J. Zheng, X. Guan, and L. Li, *Preparation and morphology-sensitive luminescence properties of Eu3+-doped YVO4: a defect chemistry viewpoint of study*, CrystEngComm **14** (2012), 3227–3235.

[220] S. Wang, T. Andersson, and M. J. Ekenstedt, *Interface morphology in molecular beam epitaxy grown In0.5Ga0.5As/GaAs strained heterostructures*, Appl. Phys. Lett. **59** (1991), 2156–2158.

[221] J. Christen, *Characterization of semiconductor interfaces with atomic scale resolution by luminescence*, 239–265, Springer Berlin Heidelberg, 1990, p. 239–265.

[222] I. I. Khaliava, A. L. Khamets, I. Safronov, A. Filonov, T. Suemasu, and D. Migas, *Effect of morphology on the phonon thermal conductivity in si/ge superlattice nanowires*, Jpn. J. Appl. Phys. **62** (2022), SD1013.

[223] C. Polanco, R. Rastgarkafshgarkolaei, J. Zhang, N. Le, P. Norris, P. Hopkins, and A. W. Ghosh, *Role of crystal structure and junction morphology on interface thermal conductance*, Phys. Rev. B **92** (2015), 144302.

[224] S. Barwich, J. M. de Araújo, A. Rafferty, C. G. da Rocha, M. Ferreira, and J. Coleman, *On the relationship between morphology and conductivity in nanosheet networks*, Carbon (2021), 306–319.

[225] K. Koshmak, A. Banshchikov, R. Ciancio, P. Orgiani, F. Borgatti, G. Panaccione, A. Giglia, D. Céolin, J. Rueff, N. Sokolov, and L. Pasquali, *Buried Interfaces Effects in Ionic Conductive LaF3–SrF2 Multilayers*, Adv. Mater. Interfaces **4** (2017), 1600875.

[226] G. Zuo, X. Liu, M. Fahlman, and M. Kemerink, *Morphology Determines Conductivity and Seebeck Coefficient in Conjugated Polymer Blends.*, ACS Appl. Mater. Interfaces **10 11** (2018), 9638–9644.

[227] J. Zimmerman, B. E. Lassiter, X. Xiao, K. Sun, A. Dolocan, R. Gearba, D. V. V. Bout, K. Stevenson, P. Wickramasinghe, M. Thompson, and S. Forrest, *Control of interface order by inverse quasi-epitaxial growth of squaraine/fullerene thin film photovoltaics.*, ACS nano **7 10** (2013), 9268–75.

[228] S. Kowarik, A. Gerlach, W. Leitenberger, J. Hu, G. Witte, C. Wöll, U. Pietsch, and F. Schreiber, *Energy-dispersive x-ray reflectivity and gid for real-time growth studies of pentacene thin films*, Thin Solid Films **515** (2007), 5606, The Ninth International Conference on Surface X-Ray and Neutron Scattering.

[229] E. Empting, M. Klopotek, A. Hinderhofer, F. Schreiber, and M. Oettel, *Lattice gas study of thin-film growth scenarios and transitions between them: Role of substrate*, Phys. Rev. E **103** (2021), 023302.

[230] C. Zhuang, K. Chen, J. Redwing, Q. Li, and X. Xi, *Surface morphology and thickness dependence of the properties of MgB2 thin films by hybrid physical–chemical vapor deposition*, Supercond. Sci. Technol. **23** (2010), 055004.

[231] P. Fenter, F. Schreiber, L. Zhou, P. Eisenberger, and S. Forrest, *In situ studies of morphology, strain, and growth modes of a molecular organic thin film*, Phys. Rev. B **56** (1997), 3046–3053.

[232] A. Perrotta, P. Christian, A. O. F. Jones, F. Muralter, and A. Coclite, *Growth regimes of poly(perfluorodecyl acrylate) thin films by initiated chemical vapor deposition*, Macromolecules **51** (2018), 5694 – 5703.

[233] J. Krug, *Origins of scale invariance in growth processes*, Adv. Phys. **46** (1997), 139.

[234] E. Empting, M. Klopotek, A. Hinderhofer, F. Schreiber, and M. Oettel, *Lattice gas study of thin-film growth scenarios and transitions between them: Role of substrate*, Phys. Rev. E **103** (2021), 023302.

[235] N. Shioya, R. Murdey, K. Nakao, H. Yoshida, T. Koganezawa, K. Eda, T. Shimoaka, and T. Hasegawa, *Alternative face-on thin film structure of pentacene*, Sci. Rep. **9** (2019), 579.

[236] G. Hu, G. Orkoulas, and P. D. Christofides, *Regulation of film thickness, surface roughness and porosity in thin film growth using deposition rate*, Chem. Eng. Sci. **64** (2009), 3903–3913.

[237] T. Storzer, A. Hinderhofer, C. Zeiser, J. Novák, Z. Fišer, V. Belova, B. Reisz, S. Maiti, G. Duva, R. K. Hallani, A. Gerlach, J. E. Anthony, and F. Schreiber, *Growth, structure, and anisotropic optical properties of difluoro-anthradithiophene thin films*, J. Phys. Chem. C **121** (2017), 21011–21017.

[238] Y. Zeng, B. Tao, and Z. Yin, *Molecular orientation transformation of pentacene on amorphous $SiO_2$: A computational study on the initial growth stage of physical vapor deposition*, J. Cryst. Growth. **405** (2014), 73–80.

[239] Y. Zeng, B. Tao, J. Chen, and Z. Yin, *Temperature-dependent orientation study of the initial growth of pentacene on amorphous $SiO_2$ by molecular dynamics simulations*, J. Cryst. Growth. **429** (2015), 35–42.

[240] N. Alagna, J. Han, N. Wollscheid, J. L. Perez Lustres, J. Herz, S. Hahn, S. Koser, F. Paulus, U. H. F. Bunz, A. Dreuw, T. Buckup, and M. Motzkus, *Tailoring Ultrafast Singlet Fission by the Chemical Modification of Phenazinothiadiazoles*, J. Am. Chem. Soc. **141** (2019), 8834–8845.

[241] B. D. Lindner, B. A. Coombs, M. Schaffroth, J. U. Engelhart, O. Tverskoy, F. Rominger, M. Hamburger, and U. H. F. Bunz, *From Thia- to Selenadiazoles: Changing Interaction Priority*, Org. Let. **15** (2013), 666–669.

[242] B. A. Coombs, B. D. Lindner, R. M. Edkins, F. Rominger, A. Beeby, and U. H. F. Bunz, *Photophysical property trends for a homologous series of bis-ethynyl-substituted benzochalcogendiazoles*, New J. Chem. **36** (2012), 550–553.

[243] A. Opitz, G. Duva, M. Gebhardt, H. Kim, E. Meister, T. Meisel, P. Beyer, V. Belova, C. Kasper, J. Pflaum, L. Pithan, A. Hinderhofer, F. Schreiber, and W. Brütting, *Thin films of electron donor–acceptor complexes: characterisation of mixed-crystalline phases and implications for electrical doping*, Mater. Adv. **3** (2022), 1017–1034.

[244] P. Peumans, S. Uchida, and S. R. Forrest, *Efficient bulk heterojunction photovoltaic cells using small-molecular-weight organic thin films*, Nature **425** (2003), 158–162.

[245] S. A. Burke, J. M. Topple, and P. Grütter, *Molecular dewetting on insulators*, J. Phys. Condens. Matter. **21** (2009), 423101.

[246] T. Breuer, A. Karthäuser, H. Klemm, F. Genuzio, G. Peschel, A. Fuhrich, T. Schmidt, and G. Witte, *Exceptional Dewetting of Organic Semiconductor Films: The Case of Dinaphthothienothiophene (DNTT) at Dielectric Interfaces*, ACS Appl. Mater. Interfaces **9** (2017), 8384–8392, PMID: 28218510.

[247] R. Acharya, D. Günder, T. Breuer, G. Schmitz, H. Klauk, and G. Witte, *Stability of organic thin-film transistors based on ultrathin films of dinaphtho[2,3-b:2',3'-f]thieno[3,2-b]thiophene (DNTT)*, J. Mater. Chem. C **9** (2021), 270–280.

[248] C. Albonetti, M. Barbalinardo, S. Milita, M. Cavallini, F. Liscio, J.-F. Moulin, and F. Biscarini, *Selective Growth of α-Sexithiophene by Using Silicon Oxides Patterns*, Int. J. Mol. Sci. **12** (2011), 5719–5735.

[249] S. Kowarik, A. Gerlach, S. Sellner, L. Cavalcanti, and F. Schreiber, *Dewetting of an Organic Semiconductor Thin Film Observed in Real-time*, Adv. Eng. Mater. **11** (2009), 291–294.

[250] A. C. Dürr, N. Koch, M. Kelsch, A. Rühm, J. Ghijsen, R. L. Johnson, J.-J. Pireaux, J. Schwartz, F. Schreiber, H. Dosch, and A. Kahn, *Interplay between morphology, structure, and electronic properties at diindenoperylene-gold interfaces*, Phys. Rev. B **68** (2003), 115428.

[251] J. Wagner, M. Gruber, A. Hinderhofer, A. Wilke, B. Bröker, J. Frisch, P. Amsalem, A. Vollmer, A. Opitz, N. Koch, F. Schreiber, and W. Brütting, *High fill factor and open circuit voltage in organic photovoltaic cells with diindenoperylene as donor material*, Adv. Funct. Mater. **20** (2010), 4295–4303.

[252] M. W. Wilson, A. Rao, B. Ehrler, and R. H. Friend, *Singlet exciton fission in polycrystalline pentacene: from photophysics toward devices*, Acc. Chem. Res. **46** (2013), 1330–1338.

[253] M. Kitamura and Y. Arakawa, *Pentacene-based organic field-effect transistors*, J. Phys. Condens. Matter. **20** (2008), 184011.

[254] I. Dax, I. A. Zaluzhnyy, A. Pylypenko, N. Russegger, V. Starostin, R. Rysov, F. Westermeier, M. Sprung, A. Hinderhofer, L. Pithan, and F. Schreiber, *Insight into heterogeneous dynamics of growing islands using coherent X-ray scattering*, New J. Phys. **25** (2023), 103033.

[255] D. Lapkin, R. Nasro, J. Hagara, B. Hofferberth, A. Hinderhofer, A. Gerlach, and F. Schreiber, *Vacuum chamber for deposition of gradient thin films: Toward high-throughput structure–property correlative studies*, Rev. Sci. Instrum. **96** (2025), 053905.

[256] I. Hirosawa, T. Watanabe, T. Koganezawa, M. Kikuchi, and N. Yoshimoto, *Surface morphology of vacuum-evaporated pentacene film on Si substrate studied by in situ grazing-incidence small-angle X-ray scattering: I. The initial stage of formation of pentacene film*, Jpn. J. Appl. Phys. **57** (2018), 03EG12.

[257] C. Lorch, J. Novák, R. Banerjee, S. Weimer, J. Dieterle, C. Frank, A. Hinderhofer, A. Gerlach, F. Carla, and F. Schreiber, *Influence of C60 co-deposition on the growth kinetics of diindenoperylene–From rapid roughening to layer-by-layer growth in blended organic films*, J. Chem. Phys. **146** (2017), 052807.

[258] E. Chason and T. M. Mayer, *Thin film and surface characterization by specular X-ray reflectivity*, Crit. Rev. Solid State Mater. Sci. **22** (1997), 1–67.

[259] A. Gerlach, S. Sellner, S. Kowarik, and F. Schreiber, *In Situ X-Ray Scattering Studies of OFET Interfaces*, 161–187, Wiley-VCH Verlag GmbH & Co. KGaA, 2009, p. 161–187.

[260] A. Hinderhofer, T. Hosokai, K. Yonezawa, A. Gerlach, K. Kato, K. Broch, C. Frank, J. Novák, S. Kera, N. Ueno, and F. Schreiber, *Post-growth surface smoothing of thin films of diindenoperylene*, Appl. Phys. Lett. **101** (2012), 033307.

[261] S. Kowarik, A. Gerlach, S. Sellner, F. Schreiber, L. Cavalcanti, and O. Konovalov, *Real-time observation of structural and orientational transitions during growth of organic thin films*, Phys. Rev. Lett. **96** (2006), 125504.

[262] P. Elsässer and T. Schilling, *Structural transition in the single layer growth of diindenoperylene on silica*, J. Chem. Phys. **161** (2024), 094903.

[263] D. Babonneau, S. Camelio, D. Lantiat, L. Simonot, and A. Michel, *Waveguiding and correlated roughness effects in layered nanocomposite thin films studied by grazing-incidence small-angle x-ray scattering*, Phys. Rev. B **80** (2009), 155446.

[264] M. Schwartzkopf, S.-J. Wöhnert, V. Waclawek, N. Carstens, A. Rothkirch, J. Rubeck, M. Gensch, J. Drewes, O. Polonskyi, T. Strunskus, A. M. Hinz, S. J. Schaper, V. Körstgens, P. Müller-Buschbaum, F. Faupel, and S. V. Roth, *Real-time insight into nanostructure evolution during the rapid formation of ultra-thin gold layers on polymers*, Nanoscale Horiz. **6** (2021), 132–138.

[265] M. Gruber, M. Rawolle, J. Wagner, D. Magerl, U. Hörmann, J. Perlich, S. V. Roth, A. Opitz, F. Schreiber, P. Müller-Buschbaum, and W. Brütting, *Correlating Structure and Morphology to Device Performance of Molecular Organic Donor–Acceptor Photovoltaic Cells Based on Diindenoperylene (DIP) and $C_{60}$*, Adv. Energy Mater **3** (2013), 1075–1083.

[266] A. Hinderhofer, U. Heinemeyer, A. Gerlach, S. Kowarik, R. M. J. Jacobs, Y. Sakamoto, T. Suzuki, and F. Schreiber, *Optical properties of pentacene and perfluoropentacene thin films*, J. Chem. Phys. **127** (2007), 194705.

[267] H. Yang, T. J. Shin, M.-M. Ling, K. Cho, C. Y. Ryu, and Z. Bao, *Conducting AFM and 2D GIXD studies on pentacene thin films*, J. Am. Chem. Soc. **127** (2005), 11542–11543.

[268] S. Pachmajer, A. O. Jones, M. Truger, C. Röthel, I. Salzmann, O. Werzer, and R. Resel, *Self-limited growth in pentacene thin films*, ACS Appl. Mater. Interfaces **9** (2017), 11977–11984.

[269] V. M. Nichols, K. Broch, F. Schreiber, and C. J. Bardeen, *Excited-state dynamics of diindenoperylene in liquid solution and in solid films*, J. Phys. Chem. C **119** (2015), 12856–12864.

[270] G. Duva, L. Pithan, C. Zeiser, B. Reisz, J. Dieterle, B. Hofferberth, P. Beyer, L. Bogula, A. Opitz, S. Kowarik, A. Hinderhofer, A. Gerlach, and F. Schreiber, *Thin-Film Texture and Optical Properties of Donor/Acceptor Complexes. Diindenoperylene/F6TCNNQ vs Alpha-Sexithiophene/F6TCNNQ*, J. Phys. Chem. C **122** (2018), 18705–18714.

[271] D. Faltermeier, B. Gompf, M. Dressel, A. K. Tripathi, and J. Pflaum, *Optical properties of pentacene thin films and single crystals*, Phys. Rev. B **74** (2006), 125416.

[272] B. K. Tanner, *Grazing Incidence X-Ray Reflectivity and Scattering*, 1181–1214, Springer International Publishing, 2019, p. 1181–1214.

# List of own publications

1.) **A. Pylypenko**, E. Chulanova, F. Unger, J. Keck, I. Zaluzhnyy, I. Dax, M. Schwartzkopf, A. Gerlach, A. Hinderhofer, A. J. Meixner and F. Schreiber, Thin films of conjugated chalcogenadiazole: Growth, structure, and optical properties of substituted selenadiazoloquinoxaline, *J. Phys. Chem. C*, 128 (2024), 8104–8113.

2.) **A. Pylypenko**, D. Lapkin, E. Chulanova, I. Zaluzhnyy, V. Munteanu, A. Gerlach, A. Hinderhofer, M. Schwartzkopf, M. Jankowski, O. Konovalov, and F. Schreiber, Growth, Structure and Optical Properties of Neat, Bilayer and Codeposited Thin Films: Combining Dibenzoselenadiazoloquinoxaline with Diindenoperylene and Pentacene, *J. Phys. Chem. C*, 129 (2025), 21223–21234.

3.) I. Dax, I. Zaluzhnyy, **A. Pylypenko**, N. Russegger, V. Starostin, R. Rysov, F. Westermeier, M. Sprung, A. Hinderhofer, L. Pithan and F. Schreiber, Insight into heterogeneous dynamics of growing islands using coherent x-ray scattering, *New J. Phys.*, 25 (2023), 103033.

4.) E. Chulanova, D. Lapkin, **A. Pylypenko**, F. Unger, J. Keck, A. Gerlach, A. J. Meixner and F. Schreiber, Graphene assisted growth of highly ordered substituted selenadiazoloquinoxaline in thin film with tuned optical properties (in preparation).

# Acknowledgments

This thesis would not have been possible without the help, guidance, and encouragement of the many people who supported me in countless ways throughout my doctoral studies. I would like to take this opportunity to express my sincere gratitude to all of them.

First and foremost, I would like to express my deepest appreciation to Prof. Frank Schreiber for giving me the opportunity to conduct my PhD research in his wonderful group. I am truly grateful for the trust, freedom, and continuous support I have received over the years. I believe that only a great person can create such a productive and welcoming scientific environment and bring together so many inspiring people. I am also thankful for the patience and encouragement that he showed during the more challenging phases of the project, which helped me grow as an independent researcher.

I would also like to thank two wonderful professors whom I had the honor to meet: Prof. Martin Oettel, for reviewing my thesis and serving on the examination board, and Prof. Dieter Kölle, for kindly participating in my thesis defense. I truly appreciate the time and effort you have dedicated to this work.

A very special place in these acknowledgments goes to Dr. Dmitry Lapkin for his valuable contributions, many helpful discussions, and inspiring ideas. I deeply appreciate his willingness to discuss results, share his expertise, and provide practical advice whenever experiments or data analysis became complex. Looking back, I can say that Dr. Lapkin guided me exceptionally well and taught me more than I could ever have expected. You are a great scientist - one of the brightest I have met.

Another special place belongs to my officemate and an outstanding scientist, Dr. Ivan Zaluzhnyy, whose impact on my scientific path is impossible to overstate. He was always there to help - whether it was a diffractometer problem or a theoretical question I was struggling with. Our exchanges of ideas greatly broadened my scientific horizons. I deeply value his knowledge, expertise, and constant willingness to help.

My sincere thanks also go to Dr. Alexander Gerlach and Dr. Alexander Hinderhofer, highly valued professionals who introduced me to the laboratory in 2021, taught me how to operate the equipment, and shared many insightful comments on my papers and on this thesis. Their support has been extremely important throughout this journey.

I am grateful to my former officemates and colleagues Dr. Ekaterina Kneschaurek, Dr. Elena Chulanova, and Dr. Ingrid Dax, with whom I took my first steps in independent scientific work and traveled to numerous beamtimes. I would also

like to thank Dr. Giuliano Duva and Dr. Nadine Rußegger, who shared their experience and guided me during my first thin-film depositions.

Proper scientific work would not have been possible without the outstanding engineering support of Bernd Hofferberth, who built, repaired, and improved so many pieces of equipment and generously shared his expertise. Another essential part of our work rests on the shoulders of our secretaries, Susanne Kern and Aleksandra Rötschke, whose tireless organizational efforts keep everything running smoothly. I am sincerely grateful for all they do.

I would also like to thank Dr. Fajun Zhang and Dr. Günter Bertsche for providing me with teaching duties and the opportunity to lead practical courses. This experience was extremely important to me, and I appreciate it very much.

I am thankful for our gym sports team - Dr. Maximilian Senft, Paul Zimmermann, and later Ainur Abukaev and Gianfranco Melis. Having this way to clear my head from daily routine was, and still is, incredibly valuable.

My heartfelt thanks go to all my friends in the research group, who made the lab and office truly enjoyable places to work: Niels Scheffczyk, Mikhail Romodin, Sebastian Retzbach, Jasmin Rettenmeier, Constantin Völter, Ross Carter, Hans Mauser, and Sebastian Schwartzkopff. It has been a privilege to share this journey with such talented, motivated, and supportive people. From long experimental shifts to late-night data analysis, from group meetings to coffee breaks—every moment spent together has made these years unforgettable. I am grateful for the atmosphere of collaboration, humor, and mutual support that made even the most intense periods productive and enjoyable.

Beyond the scientific environment in Tübingen, I would like to express my deepest gratitude to my closest friends. At a special place are my friends from my bachelor's studies, Dr. Vadym Voitsekhovskyi and Orest Petriv. I thank Dr. Artem Levchuk, with whom I later began my European scientific journey in Le Mans as master students and who provided me with the best assistance possible. Together with Dr. Vladyslav Mishyn and Dr. Anna Voronova, I continued this path in Lille. Their friendship, understanding, and constant encouragement have been a source of strength. To all my friends back in Ukraine, whom I cannot meet because of the war - I miss you all more than words can say. Dmytro Paschenko, Dmytro Navrotskiy, Ivan Kogut, Nazar Sedak and all others, I send you all my love and support.

My greatest thanks go to my family, who have always supported me and loved me through everything we have faced together.

Finally, I want to express my deepest love and gratitude to my wonderful wife, Anastasiia. Your patience, optimism, and unwavering support carried me through the most challenging times. Thank you for standing by my side, for celebrating the small victories, and for lifting me up when things were difficult. This thesis would not have been possible without your love and encouragement.

To everyone who has been part of this journey, whether through talking about science, sharing laughter, or giving quiet support, I thank you for making these years such an important and memorable part of my life.